Shock Driven Discrete Vortex Growth on Oblique Interfaces

by

Alexander Martin Rasmus

A dissertation submitted in partial fulfillment
of the requirements for the degree of
Doctor of Philosophy
(Applied Physics)
in The University of Michigan
2019

Doctoral Committee:

      Associate Research Professor Carolyn Kuranz, Chair
      Doctor Carlos Di Stefano, Los Alamos National Laboratory
      Professor R. Paul Drake
      Associate Professor Eric Johnsen
      Professor Y.Y. Lau
      Assistant Professor Louise Willingale

In Memoriam Roch Kendrick

Acknowledgments

This work would not have been possible without the assistance of many people. First, I have been extremely fortunate to have Carolyn Kuranz, Carlos Di Stefano, and Kirk Flippo as advisors. They have all contributed to my growth as a physicist and a person, and it is hard to imagine this dissertation would have been completed without the contributions of each of them. Mario Manuel provided important guidance during my years in Michigan, and greatly increased my proficiency as an experimental physicist over the course of two experimental campaigns on Trident and Titan. Andy Hazi provided a great deal of mentorship during the tedious process of authoring my first publication.

My fellow graduate students and coworkers in the Paul Drake group, in particular Pat Belancourt, Josh Davis, Jeff Fein, and Sallee Klein, were an important source of friendship, support, and scientific discussion during my time in Michigan.

I thank my girlfriend Georgia for her patience and support while I finished my degree. I also thank my family for their support in this and all my other endeavors.

Finally, I thank Cary Forest for introducing me to experimental plasma physics.

Table of Contents

List of Tables

List of Figures

List of Appendices

Appendix

Abstract

A shock incident on a contact surface between two materials will deposit vorticity baroclinically given mis-alignments between pressure and density gradients. This vorticity will typically cause any perturbations on the pre-shock interface to grow. The process responsible for that growth will depend on the average tilt between interface and incoming shock, the details of the perturbation on the pre-shock interface, the material properties, and the strength of the incoming shock. If the shock front is parallel to the pre-shock interface the Richtmyer-Meshkov (RM) process will dominate perturbation growth. If the shock front is orthogonal to the pre-shock interface, the shear-driven Kelvin-Helmholtz (KH) instability will typically dominate perturbation growth. Previous theoretical work describing the shock-driven KH instability has assumed that the baroclinic vorticity deposition by the shock along the interface is independent of the post-shock shear flow across that same interface. However, this contradicts Stokes' theorem, which establishes a direct correspondence between the integral vorticity within some region and the shear flow across it through the definition of vorticity ($\vec{\omega} = \vec{\nabla} \times \vec{u}$). Here, I generalize a method for estimating integral baroclinic vorticity generation in the KH geometry, first presented in Hurricane, 2008 [32], to both include an arbitrary tilt between the shock and interface, and to furthermore calculate the vorticity distribution along the interface. This vorticity deposition model was previously used in conjunction with a discrete vortex model (DVM), where the vorticity was assumed to be localized to a single point per wavelength. Here, I instead use it in conjunction with a vortex sheet model, which takes into account the full vorticity distribution along the interface. The vortex sheet model can capture both the early and late time behaviors for RM, KH, and oblique geometries so long as secondary processes remain unimportant. Interestingly, for an oblique interface with an appropriate perturbation, vortex sheet models predict that perturbation growth can be dominated by RM at early times while still asymptoting to a KH-like state at late times. I present OMEGA-EP experiments and simulations which confirm this result. I then use the vorticity deposition and vortex sheet models to predict what shock-interface interaction will evolve according to the DVM post-shock. I present simulations and preliminary experimental results which support this prediction.

Chapter 1

Introduction: Fluid instabilities on interfaces

Instability, roughly speaking, refers to a system in which a small displacement results in forcing, which increases the rate of displacement in that direction, so that any displacement from equilibrium results in a growing rate of displacement away from that equilibrium. The typical example of an unstable system is a ball on top of a hill, if it is displaced in any direction it will be accelerated by gravity. A ball in a valley, however, is stable as displacing it from the bottom of the valley results in a force towards the center of the valley. Somewhere in the middle is a ball on perfectly flat plane with no dissipative forces: if you push the ball, it will keep rolling indefinitely. Even though it is moving, the ball can be thought of as in a different type of stable state, in which its velocity rather than position is stable.

Kelvin-Helmholtz (KH) and Rayleigh-Taylor (RT) are instabilities in the sense of the ball on top of the hill. The time history of their perturbation heights (the relevant "displacement") is an exponential so that the velocity of the perturbation height grows along with their physical size. Richtmyer-Meshkov (RM) is more akin to the ball on a flat plane with a constant rate of growth of the perturbation height in time. These fluid instabilities, ubiquitous in systems with shocks, lead to mixing across interfaces. For example, this mixing critically impacts the performance of inertial confinement fusion (ICF) implosions, degrading yield via the injection of cold, high-Z material into the central hot spot [47, 5]. These instabilities are thought to strongly impact the evolution of supernovae; a specific example is the early appearance of high-Z emission lines from SN1987A [4, 3]. In this dissertation, I will discuss hydrodynamic instabilities in High-Energy-Density (HED) systems, I define the HED regime more precisely in Section 1.2. Pressure has units of energy density, so that HED more or less refers to systems with very high pressures (> 1 Mbar). The HED systems I study are created via shocks. A shock is a traveling discontinuity in the pressure, density, temperature and velocity of a fluid, created when a pressure source too strong to be communicated via sound waves is incident on a medium.
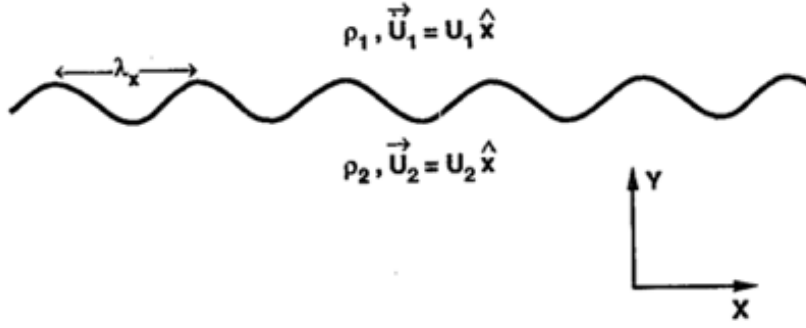
Figure 1.1   This is Fig. 1 from Mikaelian, Phys. Fluids, 1994 [58]. A schematic of an initially sinusoidal interface susceptible to KH, RT, and RM is shown. Whether the interface is unstable to Rayleigh-Taylor depends on which direction gravity points in relation to which material is denser. Assuming $\rho_2 > \rho_1$ ($\rho_1 > \rho_2$), the interface will be unstable to RT if gravity points in the $+\hat{y}$ ($-\hat{y}$) direction.

1.1   Fluid instabilities on interfaces

A shock interacting with a perturbed interface will cause the initial structure on the interface to grow due to the deposition of vorticity from mis-aligned pressure and density gradients, see Fig. 1.2. When the shock is traveling normal to the mean interface, the subsequent interface evolution is known as the Richtmyer-Meshkov process [63, 55, 56]. When the shock travels parallel to the mean interface, a shear flow is driven across the interface which results in the Kelvin-Helmholtz instability [88, 28] (there will also typically be some elements of RM present even in the KH geometry). When a sustained pressure gradient is present across the interface (e.g. from gravity) which opposes the density gradient the Rayleigh-Taylor instability results. The vorticity which drives these processes is deposited by the baroclinic term in the vorticity equation:

$$\frac{D\vec{\omega}}{Dt} + \vec{\omega}\nabla \cdot \vec{u} - \vec{\omega} \cdot \nabla \vec{u} = \left[\frac{\nabla\rho \times \nabla p}{\rho^2}\right]_{\text{baroclinic}} \tag{1.1}$$

where $\frac{D}{Dt}$ is the convective derivative, $\vec{u}$ is the velocity, $\vec{\omega} = \nabla \times \vec{u}$ is the vorticity, p is the pressure, and ρ is the density. When the shock is oblique, i.e. incident at some intermediate angle, elements of both KH and RM will be driven by the shock [58]. I will now describe each of KH, RM, and RT in more detail, and then discuss how they couple in the oblique case.

1.1.1   The Kelvin-Helmholtz instability

KH is an instability of shear layers. There is shear across some contact surface when the flow parallel to the contact surface varies across it. In more detail, suppose two fluids with the same

pressure but differing densities are superposed, i.e. fluid one exists everywhere $y > 0$ and fluid two exists everywhere $y < 0$. Fluid one has density ρ_1 and fluid two has density ρ_2. Furthermore, assume that fluid one has velocity u_1 parallel to the interface, and that fluid two has velocity u_2 parallel to the interface, see Fig. 1.1. The difference between the tangential velocities across the interface is denoted by $\Delta u = u_2 - u_1$. I furthermore assume the interface has a perturbation given by $\eta(x,t) \propto \exp i(kx - \gamma t)$, where k is the wavenumber $k = 2\pi/\lambda$ and γ is the exponential growth rate. The following dispersion relation can be found for the evolution of perturbations on the interface [43]:

$$\gamma = \frac{k(\rho_1 u_1 + \rho_2 u_2)}{\rho_1 + \rho_2} \pm \sqrt{-\frac{k^2 \rho_1 \rho_2 (\Delta u)^2}{(\rho_1 + \rho_2)^2}}. \tag{1.2}$$

The first term on the right hand side gives the motion of the interface perturbation relative to the frame chosen, while the term inside the square root gives the instability growth rate. In general, KH growth will be stronger for shorter wavelengths, densities which are nearer to equivalent, and larger shear flows. As this formulation does not include damping mechanisms (e.g. viscosity), it is unstable to KH for all wavelengths unless the shear across the interface is zero. As this instability evolves, non-linear processes lead to the formation of co-rotating vortices typically referred to as KH rollups. See Figs. 1.7, 1.11, and 1.13 for examples of experimental KH instability evolution.

1.1.2 The Rayleigh-Taylor instability

RT occurs when there are sustained, anti-parallel, density and pressure gradients across an interface. Suppose two fluids with the same pressure but differing densities are superposed, i.e. fluid one exists everywhere $y > 0$ and fluid two exists everywhere $y < 0$. Fluid one has density ρ_1 and fluid two has density ρ_2. I assume that gravity points in the $-\hat{y}$ direction with associated acceleration g. Gravity imposes a gradient in the pressure so that $\partial p/\partial y = -\rho g$ (g is taken to be positive when gravity points in the $-\hat{y}$ direction). Assuming that the interface has a perturbation given by $\eta(x,t) \propto \exp i(kx - \gamma t)$, the following dispersion relation can be found for perturbations on the interface [43]:

$$\gamma = \pm \sqrt{\frac{kg(\rho_2 - \rho_1)}{\rho_2 + \rho_1}} \tag{1.3}$$

The term inside the square root is negative when $\rho_1 > \rho_2$, so that a heavy fluid on top of a light fluid is unstable. When $\rho_1 < \rho_2$ the interface perturbation instead undergoes oscillations in perturbation height. The dispersion relation is typically given in terms of the Atwood number, defined to be $A = (\rho_2 - \rho_1)/(\rho_2 + \rho_1)$. While the derivation assumes a finite gravity, the RT instability can also be driven by accelerations from other sources, e.g. rarefactions. In terms of the vorticity equation, Eq. 1.1, the steady vorticity deposition which drives the RT instability will occur whenever there is

3

a bulk density gradient which opposes the bulk pressure gradient across the interface. RT is one limit of the general convective instability, which occurs when the entropy gradient is aligned with the density gradient [19].

1.1.3 The Richtmyer-Meshkov process

In contrast to RT and KH, RM arises due to the impulsive acceleration of an interface [63, 55, 56]. The acceleration is typically provided by a shock incident with the shock front parallel to the mean interface. A heuristic model of RM assumes the RT dispersion relation with an impulsive g, i.e.

$$g(t) = u_{\text{int}}\delta(t) \tag{1.4}$$

where u_{int} is the post-shock speed of the interface and $\delta(t)$ is the Dirac delta function. For a sinusoidal perturbation with wavelength λ and post-shock amplitude η^* this yields an initial instability velocity of

$$v_{\text{RM}} = Aku_{\text{int}}\eta^*. \tag{1.5}$$

This approximation only holds for sufficiently small perturbations and weak shocks in the light-to-heavy regime. The nomenclature "light-to-heavy" refers to the direction of shock propagation, light-to-heavy implies the primary shock is incident on the interface from the light material, whereas heavy-to-light implies the shock is incident from the heavy material. In the heavy-to-light case, the Meyer-Blewett ansatz may instead be used [57]:

$$v_{\text{RM}} = Aku_{\text{int}}\frac{\eta^* + \eta}{2}. \tag{1.6}$$

where η is the pre-shock amplitude. This ansatz is a reasonable approximation to simulation results rather than the result of analytic theory. More detailed analytic calculations of RM growth must take higher-order effects into account, which include variations induced in the transmitted and reflected waves by the perturbation along the interface [95, 94, 96]. See Figs. 1.3, 1.9, and 1.10 for experimental examples of RM evolution.

RM lacks the feedback and exponential growth of RT and KH in the linear regime. For this reason, RM is sometimes described as a "process" rather than an "instability". Where it is not overly onerous, I refer to RM as a process. However, when describing RT, KH, and RM collectively I will describe them as instabilities on interfaces. The natural growth rates to describe the evolution of KH and RT differs from that of RM: for RM the first time derivative of the perturbation height dominates, whereas in KH and RT the second time derivate of the perturbation height dominates. Where possible, I will use the term "perturbation velocity" or "instability velocity" to refer to the

first derivative of the perturbation height and reserve the term "growth rate" for the characteristic time for exponential growth for RT and KH.

1.1.4 The combined Rayleigh-Taylor, Richtmyer-Meshkov, and Kelvin-Helmholtz instabilities

For oblique shocks, all three of RT, RM, and KH may occur simultaneously. Supposing that a shock is incident on an interface with some finite tilt between the shock front and mean interface, RM will be driven by the impulsive acceleration of the interface, KH may result from shear flow across the post-shock interface due to the tilt of the shock, and RT may result from deceleration if the pressure source which created the shock is unsustained. The derivations of the RT and KH linear growth rates may be performed simultaneously, with the result that the growth rates add in quadrature [43, 58].

The combined situation can be described as follows. Suppose two fluids with the same pressure but differing densities are superposed, i.e. fluid one exists everywhere $y > 0$ and fluid two exists everywhere $y < 0$. Furthermore, assume that fluid one has velocity u_1 parallel to the interface, and that fluid two has velocity u_2 parallel to the interface. Furthermore, imagine that gravity points in the $-\hat{y}$ direction with acceleration g. Assuming that the structure on the interface has structure given by $\eta(x,t) \propto \exp i(kx - \gamma t)$, the following dispersion relation can be found for perturbations on the interface [43]:

$$\gamma = \frac{k(\rho_1 u_1 + \rho_2 u_2)}{\rho_1 + \rho_2} \pm \sqrt{\frac{kg(\rho_2 - \rho_1)}{\rho_2 + \rho_1} - \frac{k^2 \rho_1 \rho_2 (\Delta u)^2}{(\rho_1 + \rho_2)^2}}. \tag{1.7}$$

The heuristic interpretation of RM as an impulsive acceleration at $t = 0$ is implicitly contained in this dispersion relation. More generally, one should use an appropriate formula to calculate the RM instability velocity and let this be the instability velocity at $t = 0$ (i.e. $d\eta/dt(t = 0) = v_{\text{RM}}$). RT and KH will then feed back on the initial condition through higher order derivatives.

The dispersion relation given in Eq. 1.7 also suggests one way of thinking about combined instability growth on oblique interfaces, in which the instabilities are linearly independent, and the growth rates from RM, KH, and RT can be added together in a quantitative sense. This picture of coupled instability growth is described in detail in Mikaelian, 1994 [58]. Given that the dispersion relation in Eq. 1.7 only holds in the linear regime, the description of coupled instability growth it gives also only holds in the linear regime. To understand coupled instability growth at later times a different approach is needed.
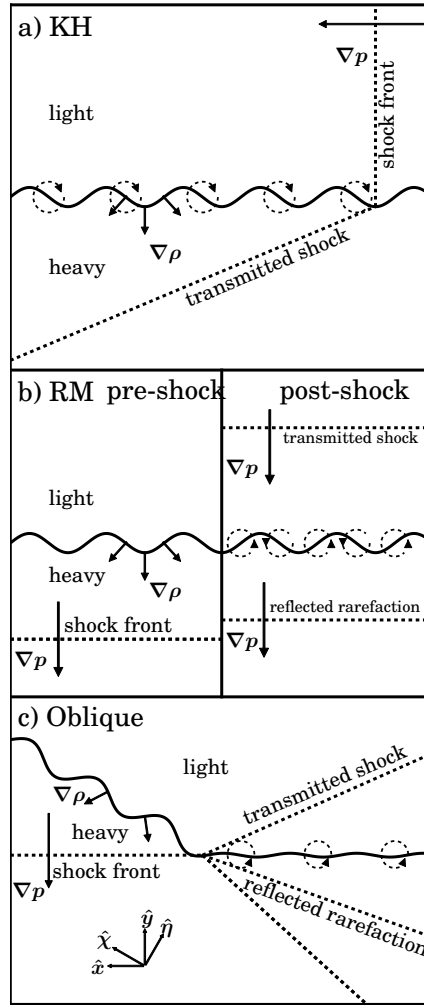
Figure 1.2 This figure shows the shock orientations associated with typical experiments to study hydrodynamic instabilities (a & b). The oblique configuration, which I investigate in this dissertation, is shown in (c). In the KH case (top) a shock which is nearly orthogonal to the interface travels right, depositing vorticity of consistent sign but varying amplitude, this frame is adapted from Fig. 2 in hurricane, 2008 [32]. In the RM case (middle) a shock, with a front nearly parallel to the interface, is incident from below and deposits vorticity of alternating sign on the interface. The incoming shock is shown on the left, and the transmitted shock and reflected rarefaction are shown on the right. In the oblique case, a shock is incident from the bottom on a tilted interface. Shocks travel opposite to the direction of their pressure gradient.
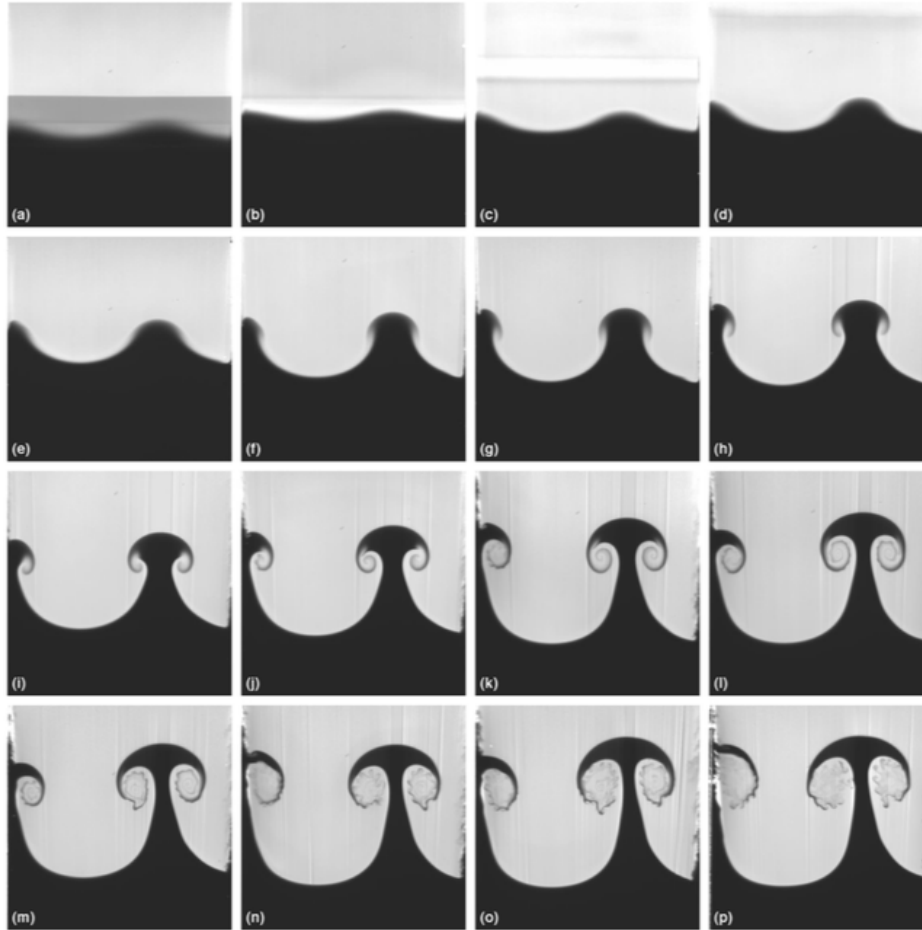
Figure 1.3 This is Figure 5 from Jacobs & Krivets, 2005 [35]. Planar Laser Induced Fluorescence (PLIF) images of RM evolution are shown. The shock can be seen crossing the interface in the top row. In the second row, non-linear processes become important, the interface structure becomes non-sinusoidal, and mushroom caps are beginning to form. In row three the mushroom caps are fully formed and counter-rotating vortices are seen on either side of each spike. In the final row, secondary instabilities appear to be taking place on the vortices themselves.

1.1.5   Late time mixing and the vortex paradigm

Late in time, RM, RT, and KH are dominated by vortex structures. The vorticity localizes due to some combination of initial modulations, secondary baroclinic vorticity generation, and non-linear processes in instability evolution. In Kelvin-Helmholtz, this results in roll-ups, and in RT and RM this causes mushroom caps (the mushrooms caps themselves are due to secondary KH). This regime of growth is well described by considering the strength, size, and distribution of these vortex structures, i.e. the so called "vortex paradigm" [98].

Quoting at length from "Vortex Paradigm for Accelerated Inhomogeneous Flows: Visiometrics for the Rayleigh-Taylor and Richtmyer-Meshkov Environments", Zabusky, 1999 [98], RM may be divided into 4 epochs of growth:

"1. Very Early Time (VET). The interval when the incident shock wave completely traverses the interface, a distance of $2a_0$, for the first time. For a very small amplitude perturbation or a very small interface angle, the linear theory applies.

"2. Early Time (ET). The interval when secondary reflected and transmitted pressure or shock waves pass over the interface (e.g. less than four transit times of a linear wave across LT , the width of the shock tube). Nonlinear effects arise early in this interval due to the growing amplitude of the interfacial perturbation, and the magnitude of the growth rate has achieved its maximum. During part of this interval, the interfacial evolution may be modeled by nonlinear theories, as discussed below, or with an evolving vortex sheet on a nearly incompressible, density-stratified interface.

"3. Intermediate Time (IT). The interval following ET when the vortex sheet or layer on the interface localizes or collapses into one or more CVSs [coherent vortex structures]. For sinusoidal perturbations, one may conveniently begin this interval when the contact discontinuity becomes a multivalued function of the transverse distance y, as discussed below.

"4. Late Time (LT). The very large interval beginning when the flow is driven by an array of compact vortices on the density-stratified interface and continuing to late in the phase when a turbulent-like collection of vortex domains merges, binds, splits, and mixes the interface."

For RM and RT, the integral vorticity over one perturbation wavelength is zero (I will go into more detail later), implying that both co- and counter-rotating vortices must be present, and in roughly equivalent numbers and strengths. Statistical models for late time, multi mode, mixing width growth of the RM process, in the limit of small Atwood number, based on the strength and size distribution of the vortices predict a mixing width proportional to

$$\eta(t)_{\text{RM}} \propto t^{0.4} \tag{1.8}$$

for two-dimensional perturbations, see Rikanati et al., 1998 [65].

A similar division into epochs of the Kelvin-Helmholtz instability, in the style of Zabusky, 1999 [98], can be made:

1. Very Early time (VET): Shear flow is incident on the interface. Assuming a small perturbation, the growth is fully linear and the vorticity distribution is uniform to first order. Kelvin-Helmholtz growth is occurring, but the perturbation is small enough that no significant feedback on the vorticity distribution has occurred.

2. Early time (ET). Non-linear processes in which the vorticity distribution is altered are occurring. The perturbation structure is no longer perfectly sinusoidal, and has begun to roll over.

3. Intermediate time (IT). The vorticity distribution has been localized and the roll-ups characteristic of Kelvin-Helmholtz are well formed.

4. Late time (LT). Secondary processes on the roll-ups become important. E.g., vortex merger processes occur.

In contrast to RM, the integral vorticity over one perturbation wavelength is finite for KH unstable interfaces. This is equivalent to stating that there is a bulk shear across the interface. Furthermore, all of the vortices that form at late times co-rotate as the vortex distribution evolves from a vortex sheet of uniform sign. The late-time, multimode, KH growth rate can be predicted from statistical models based on vortex merger rates for this type of vortex distribution. The mixing width grows linearly with time,

$$\eta(t)_{\text{KH}} \propto t, \tag{1.9}$$

see Rikanati et al., 2003 and Shimony et al., 2018 [64, 77].

Eq 1.7 can be used to readily calculate which instability is important in the linear regime, and Eqs. 1.8 and 1.9 can be used to calculate the late time, self-similar mixing rates associated with the asymptotic state of each "pure" instability state. However, Eq. 1.7 does not predict which of Eqs. 1.8 or 1.9 is appropriate for the calculation of late time mixing width growth. In particular, shock-interface interactions can be constructed such that instability can be dominated by RM-like growth in the linear regime, but which develop a KH-like distribution of vortices late in time. I show how to do this in Chapter 2. The division into epochs of this interfacial growth goes something like:

1. Very Early time (VET): RM like. The perturbation grows at a constant velocity, which is well predicted by multi-mode, linear, RM theory. The vorticity along the interface varies strongly, but is all of one sign.

2. Early time (ET): Transition. Non-linear processes which alter the shape and therefor vorticity distribution of the perturbation occur. As the vorticity is of only one sign, these non-linear processes result in the creation of one co-rotating vortex per wavelength.

3. Intermediate time (IT): KH like. The vorticity distribution has been localized and roll-ups similar to that of KH are well formed.

4. Late time (LT). KH like. Secondary processes on the rollers become important. E.g., vortex merger and secondary 3D instabilities occur.

The initial vorticity distribution has large variations, as in early time RM, but the vorticity is only of one sign, as in KH. This results in impulsive growth early in time, but the asymptotic state of the vorticity distribution is one, co-rotating, vortex per wavelength, with all vortices of like sign (as in KH). I will discuss the transition between RM and this type of growth as the initial conditions are varied in Section 2.3, when I have defined the needed parameters. The creation of this vorticity distribution can be achieved using a strong shock incident on an oblique interface with a perturbation. A set of experiments in the High-Energy-Density (HED) regime to study this type of mixing were performed at the Omega-EP laser are described in Chapter 3.

1.2 The High-Energy-Density regime and laser driven High-Energy-Density experiments

The High-Energy-Density (HED) regime is typically taken to refer to systems with pressures above 1 million atmospheres, or equivalently 1 Mbar. Pressure has units of energy density, so that high-energy-density corresponds to high-pressure. For comparison, the most effective known chemical explosive, Octanitrocubane, has a chemical potential energy of 8.5 MJ kg^{-1}, and a density of 2 g cm^{-3}, giving an energy density of 0.17 Mbar, so that the HED regime is "more energetic" than even the most powerful of conventional explosives. See Fig. 1.4 for an overview of the HED regime.

The HED regime occurs naturally in many astrophysical systems. Looking at Fig. 1.4, a line is drawn which demarcates the boundary across which the pressure is larger than 1 Mbar. The HED regime may be achieved in systems at high temperatures, high densities, or both. That a system can reach high pressures when it has both a high temperature and a high density is unsurprising. That high pressures can be achieved at high temperatures while at vanishingly small densities, or at high densities while at very small temperatures is a more surprising result. I give a short justification for each here.

Assuming a system is optically thick to its own thermal emission, the radiation pressure goes like T^4 and is independent of density, where T is taken to be the temperature. Therefore, above some temperature the pressure will be > 1 Mbar regardless of the density. At high densities and low temperatures, the pressure is dominated by Fermi degeneracy pressure. Electrons are fermions, meaning that they are not allowed to occupy the same quantum state. When electrons become so dense in space that they overlap in a spatial sense, they must instead occupy different energy levels to maintain exclusion. The Fermi degeneracy pressure is due to the additional energy density required to excite electrons which are forced to occupy higher energy states by exclusion. This is relevant to astrophysical systems that are both large enough to generate the required pressures gravitationally but lacking a heat source to sustain pressure by other means. Giant planets (e.g.
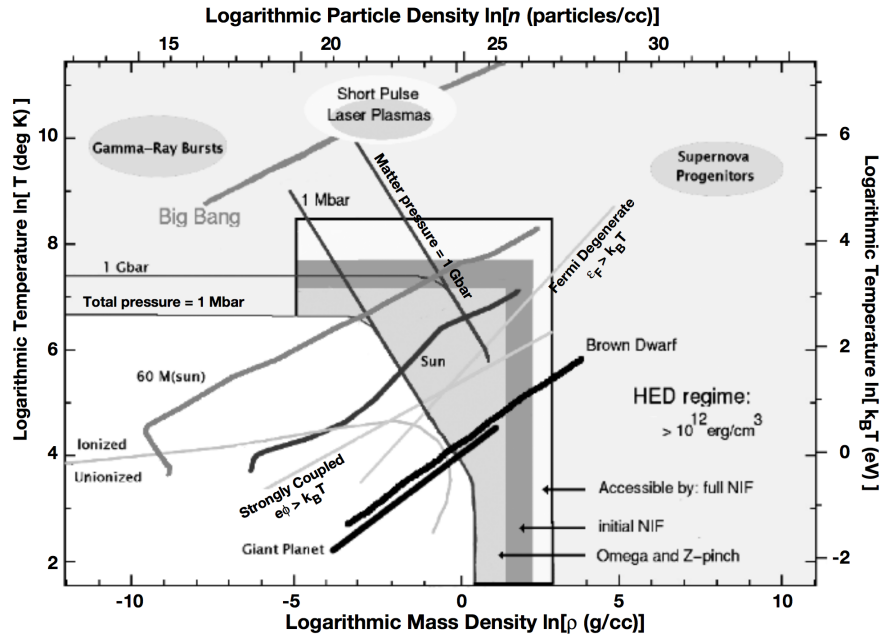
Figure 1.4 This is Figure 1.1 from Drake, 2006.

Jupiter) and brown dwarfs are typical examples. Giant planets are essentially failed stars, not quite massive enough to start fusion. Brown dwarfs are a type of stellar remnant, if a star is not large enough to become a black hole or neutron star, it will slowly burn out as it runs out of fuel for fusion reactions which sustain its temperature and luminosity. Such a star will slowly cool due to radiative processes, with the star eventually sustained by fermi degeneracy pressure alone.

1.3 The Euler equations for fluid evolution and Ryutov similarity

In addition to directly accessing thermodynamic states relevant to astrophysical processes, it is also desirable to more broadly access the fluid dynamics relevant to astrophysical processes. Terrestrial fluid dynamics experiments take place between length scales of 1 nm (as in nanofluidics experiments) with an upper limit provided by hydrodynamic test tunnels on the order of 10s of meters used to test airplane aerodynamics. Naturally occurring terrestrial fluid flows can have structure with length scales that are a sizable fraction of the Earth's circumference (e.g. Rossby waves in the atmosphere). The length scales across which astrophysical fluid dynamics take place are much larger, the sun has a radius of ≈ 7 Mm, supernovae remnants have length scales on the order of light years (1 light year $\approx 10^{16}$m), and the spatial distribution of galaxies has been observed to have length scales on the order of $\sim 10^{22}$ m [89]. Even if experiments in the HEDP regime can directly

access thermodynamic states relevant to astrophysical systems, the length scales of astrophysical processes will remain outside our reach for the foreseeable future. In order to study the dynamics of astrophysical systems, some method of scaling the dynamics to terrestrial scales is required. The typical approach is to non-dimensionalize the dynamics of the system, i.e. a characteristic scale is found for each variable in the system, and the evolution for the system is written with each variable divided by its characteristic scale. It is sometimes possible to create a system which behaves similarly to an astrophysical process in dimensionless terms, even if the physical scales of the process itself are inaccessible. A large set of scaled experiments have been performed at high-energy laser facilities studying blast-wave driven RT in supernovae relevant conditions [41, 40]. For systems described by the Euler equations, the conditions for similar evolution are described more generally by Ryutov [68, 69, 70], in this case dynamical similarity in non-dimensional terms is referred to as Ryutov similarity.

The Euler equations for a poly-tropic gas are [18]:

$$\frac{\partial \rho}{\partial t} + \nabla \cdot (\rho \mathbf{u}) = 0 \tag{1.10}$$

$$\rho \left(\frac{\partial \mathbf{u}}{\partial t} + \mathbf{u} \cdot \nabla \mathbf{u} \right) = -\nabla p \tag{1.11}$$

$$\frac{\partial p}{\partial t} + \mathbf{u} \cdot \nabla p = -\gamma p \nabla \cdot \mathbf{u} \tag{1.12}$$

Where ρ is the density, p is the pressure, u is the velocity, and γ is the polytropic index. A polytropic gas is one in which $\rho \propto p^\gamma$; a gamma law is used as a simplified equation of state, this is often approximately correct and makes analytic calculations possible (compared to EOS tables). The assumptions used to derive the Euler equations for fluids do not rely on any physical scale in isolation, but are rather dependent on ratios of scales. Quoting from Ryutov et al. [68], these equations are valid when the following are satisfied:

"1. the system needs to be 'collisional' ;

"2. energy flow by particle heat conduction needs to be negligible;

"3. energy flow by radiation flux needs to be negligible; and, finally,

"4. viscous dissipation needs to be insignificant."

Each of these conditions may be re-phrased in terms of a dimensionless parameter. Most important is (1), which is a requirement that the the characteristic length scale for collisions, λ_c, be much smaller than a characteristic length scale, L, of the the problem, i.e. $\lambda_c/L \ll 1$. When this assumption is

violated collisions will take place on scales longer than gradients in the system, so that the single fluid description of a problem will break down. For instance, if one fluid flow is incident from $x = -\infty$ with velocity $\vec{v} = v\hat{x}$ and another is incident from $x = \infty$ with velocity $\vec{v} = v\hat{x}$, there will be a region with size on the order of λ_c where the fluid velocity is multivalued provided no collisionless processes intervene.

Conditions 2 and 3 are constraints on the rate of heat transport by the flow compared to that by other processes, e.g. heat conduction or radiation. The importance of heat transport via conduction or radiation is typically described by the Péclet number,

$$
\begin{aligned}
Pe &= \frac{\text{advective heat transport}}{\text{dissipative heat transport}} \\
Pe &= \frac{UL}{D}.
\end{aligned}
\tag{1.13}
$$

where U is a characteristic velocity of the system, L is a characteristic length scale of the system, and D is the thermal diffusivity. For heat conduction, the electron thermal diffusivity should be used, whereas for the radiation flux the radiative thermal diffusivity should be used. On interfaces susceptible to fluid instabilities there is typically some density contrast between the two materials, whereas they are approximately isobaric. This implies that there is typically a temperature gradient across the interface. If the temperature difference is lessened by, e.g., heat conduction the density gradient or pressure gradient across the interface will also change, altering subsequent instability growth. An RT experiment in which heat fluxes modify instability evolution was recently published by Kuranz et al. [42].

The importance of the 4th condition is typically described via the fluid Reynolds number,

$$
\begin{aligned}
Re &= \frac{\text{advective forcing}}{\text{viscous dissipation}} \\
Re &= \frac{UL}{\nu}.
\end{aligned}
\tag{1.14}
$$

Where U is a characteristic velocity of the system, L is a characteristic length scale of the system, and ν is the kinematic viscosity of the system. When Re is large, viscous forcing will be unimportant and the flow will be susceptible to turbulence, whereas when Re is small the flow will typically be laminar. Re can be thought of as the ratio between the largest spatial scale velocity fluctuations allowed in a system (set by the spatial scale of the system) and the length scale at which viscous dissipation will damp out velocity fluctuations (determined by setting $Re = 1$ and solving for $L_\nu = \nu/U$). Typically, viscosity will reduce instability growth rates, and the instability growth is more damped for shorter wavelengths [66].

In addition to allowing comparisons between astrophysical systems and the laboratory, similarity

scalings are also crucial for understanding how laboratory experiments relate to one another. The perturbations in single mode hydrodynamic instability experiments in the HED regime typically have wavelengths on the order of 100 μm and amplitudes on the order of 10 μm. However, perturbations on the capsules used in inertial confinement fusion often have wavelengths on the order of 100 nm or less, and perturbation amplitudes on the order of 10 nm or less. Shock tube hydrodynamic instability experiments have wavelengths on the order of 1 cm. Even within terrestrial experiments, several orders of magnitude separate fundamental hydrodynamic instability experiments from the integrated context of ICF.

1.3.1 Laser-driven HED experiments

To create HED systems, either lasers or electrical currents are typically used. Nd:YLF lasers can be used to make laser pulses with a wavelength of ~ 1 μm, pulse durations of 1-10s of ns, and individual beam energies of several kilojoules, giving powers on the order of terawatts. Beams can readily be focused into spots of relative uniformity with outer diameters of ~ 1 mm using distributed phase plates, giving irradiances on the order of $\sim 10^{14}$ W cm^{-2}. This creates an ablation plume, roughly speaking an isothermal expansion wave, where the temperature is maintained by the absorption of laser energy. This ablation plume acts as a rocket, creating a pressure source for the rest of the target [37]. Non-linear crystals can be used to convert the fundamental laser harmonic into integer multiples of the original frequency. Higher order harmonics have less susceptibility to laser-plasma instabilities, which lead to reflected laser light, as well as the creation of hot electrons which cause pre-heat in experimental materials. In the experimental work in Chapter 3, lasers are used to drive a shock with a pressure of ~ 10 Mbar.

The Omega-EP laser facility

The experimental work in this dissertation was done at the Omega-EP laser facility at the Laboratory for Laser Energetics in Rochester, NY [92]. Omega-EP has four lasers, each able to deliver ≈ 4 kJ of energy over 10 ns. Two of these lasers can be converted to a short pulse mode, and deliver ≈ 1 kJ in 10 ps. Short pulse lasers are less useful for driving hydrodynamics, but are able to, e.g., create short lived line-emission x-ray sources which may be used for x-ray backlighting [61, 84] or high energy proton beams which may be used to diagnose density structure or electromagnetic fields [27, 45, 101]. Typically then, some number of beams will be used to create a physical phenomena of interest, and some number of beams will be used to diagnose the system. To diagnose a system at different times, the timing of the diagnostic beam is changed relative to the drive beams, and a time series of some experimental measurement can be compiled over severals shots. Omega-EP can

Figure 1.5 A picture of the experimental bay at Omega-EP. The optics associated with each of the four beamlines are seen in the foreground, the vacuum chamber is at the far end of the room.

perform an experiment once every 90 minutes, so that a typical experimental day consists of 7 ± 1 experiments. The long time between shots is needed to allow optics to cool as any local variations in temperature (and therefore refractive index) lead to small scale non-uniformities in the beam which in turn impact the focal quality of the beam.

1.4 Prior work

The study of the fluid instabilities discussed in this dissertation began in the late 1800s, the earliest paper cited here was published in 1868. A great breadth of research has occurred in the intervening 150 years. To drive each of RM, RT, and KH a different forcing must be present at the interface: impulsive acceleration, steady acceleration, or shear flow. In addition, the physical structures present on the interface at the onset of instability growth have a strong impact on the rate and regime of growth. Different experimental schemas determine not only which instabilities are present, but also what sort of physical structures are possible as initial conditions. Furthermore, the diagnostics available for each experiment depend on the spatial scale, time scale, and opacity of the experimental apparatus which all vary greatly between regimes. Prior work studying KH and RM has been performed in both the Low-Energy-Density (LED) and HED regimes. I will begin by discussing experiments in the LED regime, and then move on to the HED regime. See Zhou, 2017 [100, 99] for an exhaustive overview of RM and RT research up to the present day.

1.4.1 Traditional hydrodynamic instability experiments

Hydrodynamic instability experiments have been performed using shock tubes for over 100 years [7]. These facilities are typically able to measure not only interface location, but also velocity fields directly using techniques such as particle image velocimetry [1]. Traditional shock tubes offer higher repetition rates, or more dedicated shot time, as compared to HEDP facilities. In a typical shock tube experiment, a pressure source, e.g. a high pressure gas reservoir or rocket driven piston, will shock a low pressure gas section. The low pressure gas section will contain at least two fluids at initially equal pressures but differing densities. Typical shock Mach numbers achievable on these facilities are on the order of $1 < M < 5$, and the shock pressures are on the order of 10s of bar [9]. Shock tube experiments are used to study the Richtmyer-Meshkov process, and initial conditions may be provided using a variety of methods, e.g. inducing standing waves in the contact surface or varying the spatial source of flows used to produce a gas-curtain. Fig. 1.3 is from a RM shock tube experiment.

Experiments studying shocks interacting with an interface obliquely in shock tubes, with no seeded perturbation on the interface, have previously been conducted [54, 62]. See Fig. 1.6. Due to the lack of perturbation, these experiments essentially behave as the RM instability of a Chevron perturbation, given that the walls are solid to the shock and may be be treated as a reflecting boundary condition. In the future, methods of introducing perturbations could be extended to oblique configurations in the LED regime.

Splitter plates have long been used to drive the Kelvin-Helmholtz instability, i.e. two flows at differing speeds are initially separated by a physical plate. Where the splitter plate ends the Kelvin-Helmholtz instability can evolve, seeded by fluctuations in the incoming flow. See Fig. 1.7. Due to the random nature of the initial perturbations, the resulting growth is multimode, and the mixing width and perturbation spatial scale grow in kind. In addition, when the temporal duration of the experiment is long enough Rayleigh-Taylor can be driven by the Earth's gravity, see Fig. 1.8 [2]. In these experiments, the KH and RT instabilities are both present from the onset of instability growth by necessity.

In the LED regime fluid velocities can be directly measured in experiments using, e.g., particle image velocimetry (PIV). As such, the vorticity distribution in the flow can be calculated using the measured velocity field. Samtaney & Zabusky, 1994 [73] and Samtaney et al., 1998 [72] calculated the vorticity deposition by a shock onto an oblique interface the heavy-to-light and light-to-heavy case respectively. The work of Samtaney can be used to calculate the vorticity distribution along a shocked, perturbed interface by assuming that the vorticity is determined by the local tilt between the shock and interface (in addition to the shock and interface properties). Subsequent work has examined the vorticity structures which form during RM [6], see Fig. 1.9.
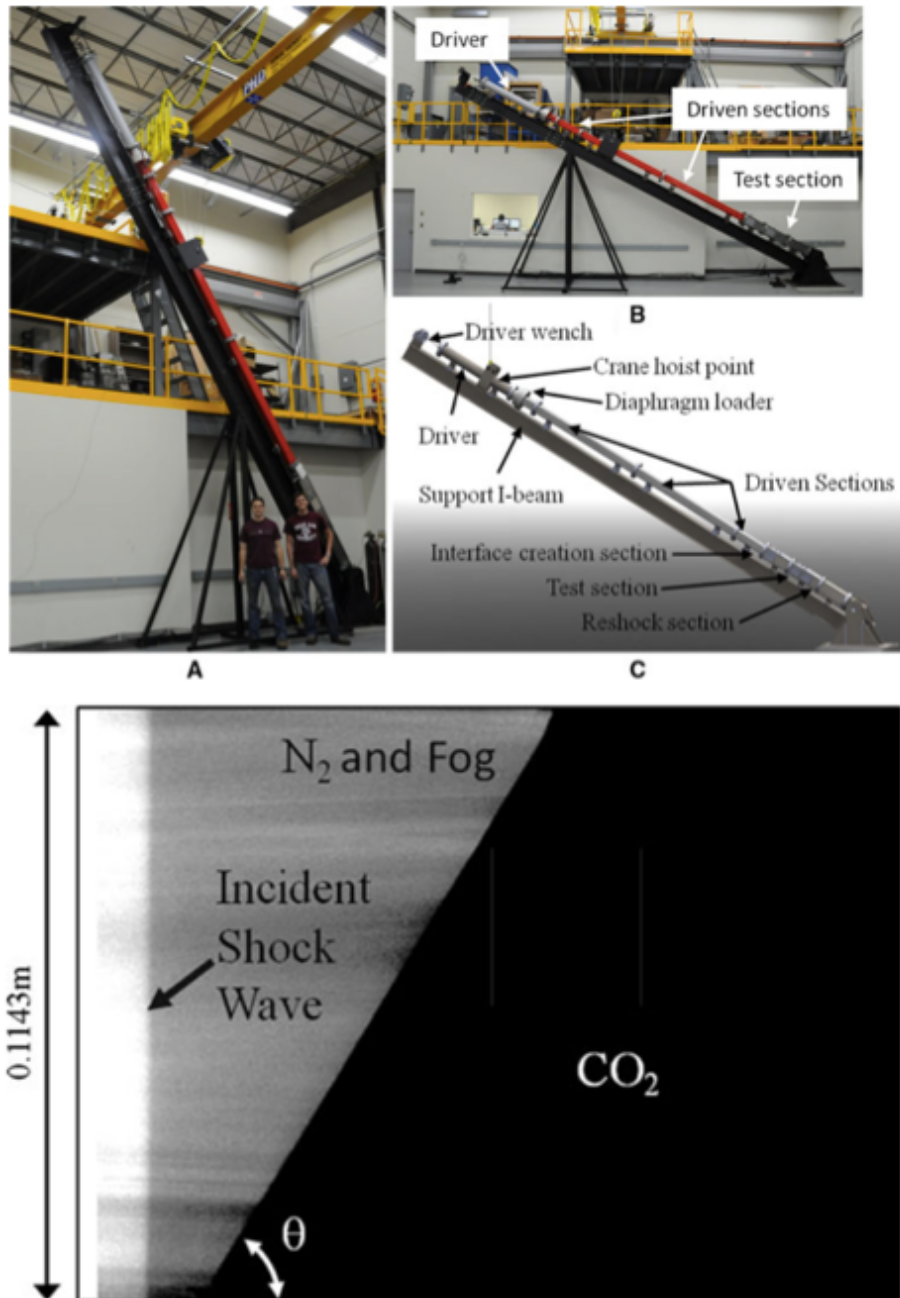
Figure 1.6 These are Figs. 1 and 3 from McFarland et al, Exp. Fluids, 2014 [54]. Top, the experimental apparatus used to drive oblique shock experiments in a shock tube are shown. The interface orientation here is determine by the direction of the Earth's gravity, whereas the shock travels axially down the tube, so that tilting the tube produces a tilt of the shock relative to the interface. Bottom, a Mie scattering image of the shock approaching the interface is pictured.
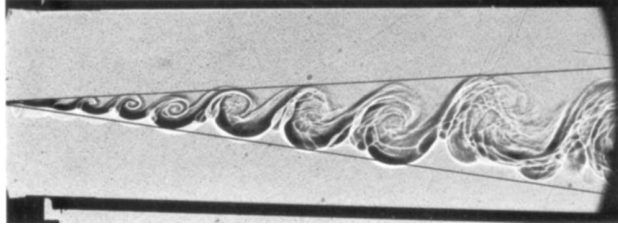
Figure 1.7 This is from Fig. 3 from Brown & Roshko, 1974 [10]. A shadowgraph of Kelvin-Helmholtz instability from a splitter plate experiment is shown. The lines approximately show the envelope of the rollers. The fluids have a bulk motion to the right, so that fluid parcels further to the right have undergone Kelvin-Helmholtz growth for a larger amount of time in a linear sense.

1.4.2 HED hydrodynamic instability experiments

In contrast to LED experiments, High-Energy-Density (HED) fluid instability experiments are driven at much higher pressures (~ 10 Mbar $= 10^7$ atm). HED experiments can therefore drive higher Mach number shocks ($M \approx 8 - 20$), and initially solid materials may be used in constructing the interface. A well characterized perturbation can therefore be machined at sub-micron accuracy and a high degree of repeatability.

The pressure sources which drive shocks in HED laser experiments are sometimes short lived compared to the experimental time scale in fluid instability experiments. When the pressure source is turned off a decompression wave, referred to as a rarefaction, is launched into the shocked material. Once this rarefaction reaches the interface, it will alter subsequent interface evolution in a manner dependent on the relative orientation of the rarefaction and interface. Previous experiments in the HED regime have studied RM [17, 16, 31, 23, 83, 14, 15, 51] and KH [26, 90, 13, 52]. In an experimental geometry designed to produce RM, the rarefaction, propagating normal to the interface, both decompresses and decelerates the interface. These processes lead to altered instability growth. In an experimental geometry designed to produce KH, sustained shocks are required to study the linear form of the instability. The rarefaction, propagating along the interface, will reduce the amount of shear flow across the mixing layer as a whole, altering the vorticity distribution of the flow, and therefore altering instability evolution as well. In the experiments discussed herein, the pressure drive of the shock is supported for 10 ns, and a rarefaction reaches the interface ~ 6 ns after the shock arrival time. It is possible to vary the duration of the laser pulse in order to alter the timing of the rarefaction relative to the initial shock.

HED experiments studying RM first appear in the literature in the mid 90s [17, 16, 31]. The first experiments were done at NOVA with a hohlraum drive, which sustained the shock pressure for ~ 4 ns, giving enough time with RM growing uncomplicated by RT that the initial impulsive growth rate of RM could be measured. These experiments were done using shocks of comparable strength to those used in instability experiments on Omega-EP currently. They found good agreement between
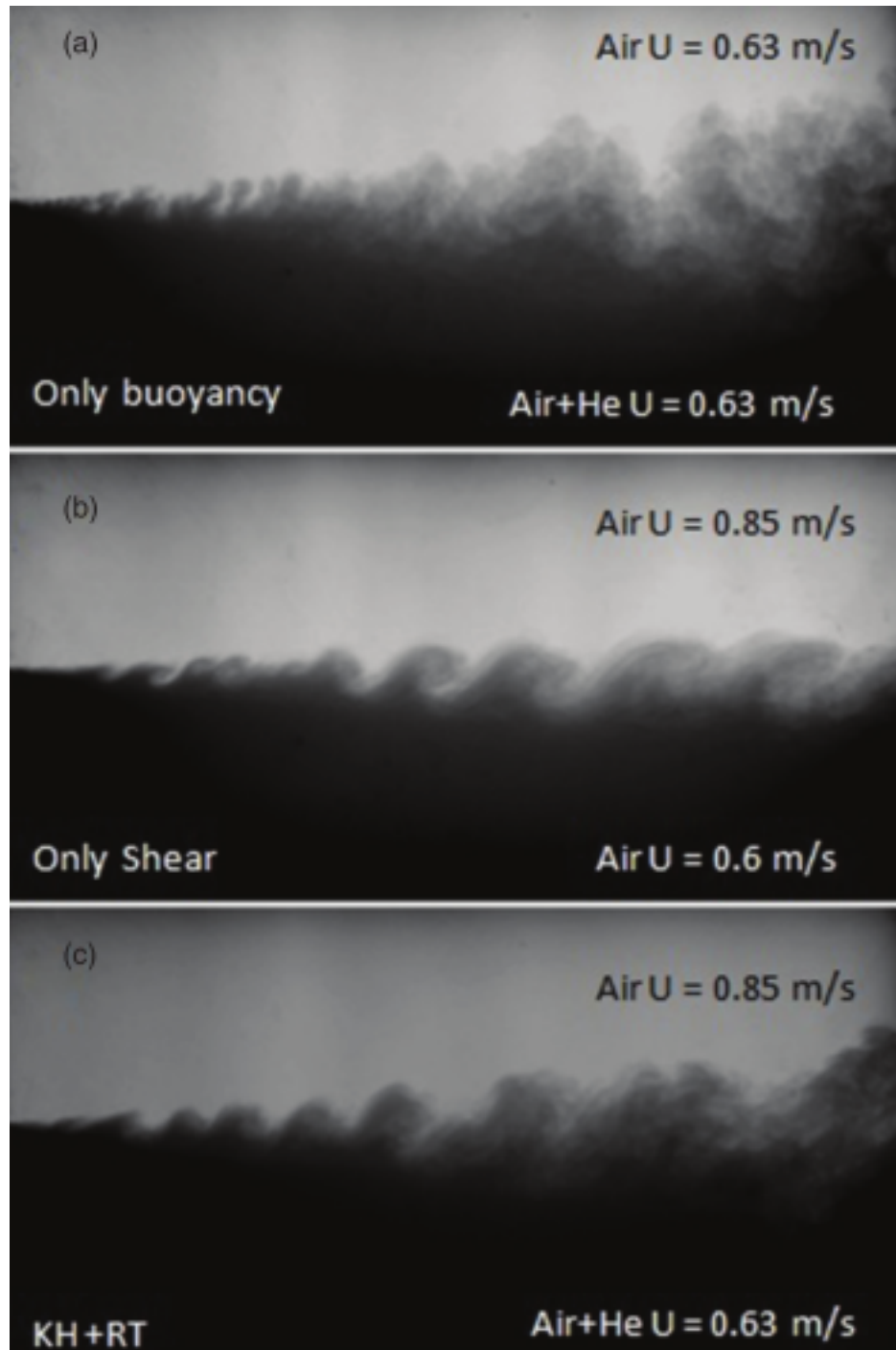
Figure 1.8 This is Fig. 3 from Akula et al., 2013. Experimental images are shown with only RT (top), only KH (middle), and combined instability growth (bottom).
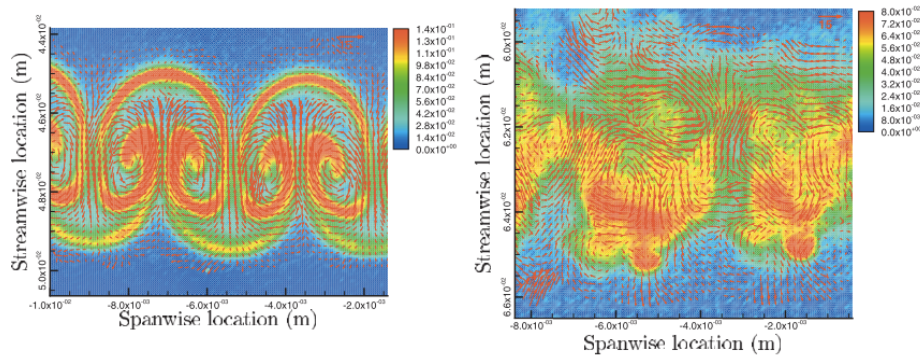
Figure 1.9 This is part of Fig. 12 from Balakumar et al., 2008 [6]. The fluid velocity (red vectors) is plotted over fluid density. The velocities and densities were measured using simultaneous PIV and PLIF images. Left, the interface after a single shock is pictured. Right, the interface is pictured after reshock.
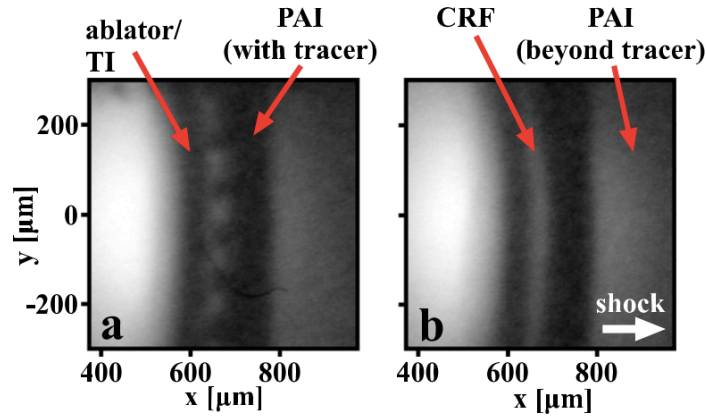
Figure 1.10 This is Fig. 2 from Di Stefano et al., 2015 [14]. Experimental radiographs of light-to-heavy RM evolution, driven by a sustained shock, are shown (a) with a machined two-mode perturbation as initial condition and (b) with a flat initial condition. Each image was taken at the same experimental time.

experiment, theory, and simulation. This initial work was focused on measuring single-mode growth rates in both the linear and non-linear regimes. These growth rates have a strong dependence on the compression of the initial structure by the shock, as well as the compressibility of the post-shock flow. Following experiments on both Omega-60 and Omega-EP studied the reduction of the impulsive growth rate due to compressibility and large-perturbation effects [23], as well as single mode growth and mode coupling under both two-mode and many-mode initial conditions under more sustained-shock conditions [51, 83, 14, 15].

The first successful KH experiments performed in the HED regime were designed by Hurricane, 2008 [32] and undertaken by Harding et al., 2009 [26]. A shock was driven through light foam which was adjacent to a heavier plastic, with the shock front orthogonal to the contact surface between these two materials, see Fig. 1.11 for an experimental radiograph. These experiments were performed on Omega-60, where only 1 ns duration laser pulses are available. The hydrodynamics is
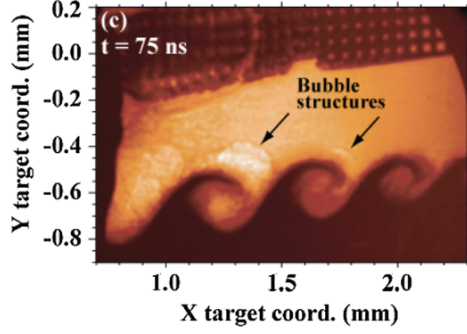
Figure 1.11 This is Fig. 2c from Harding et al., 2009 [26]. An experimental radiograph of the late-time development of blast-wave driven, single-mode KH instability is shown. The characteristic "roll-up" structures of the KH instability are evident.

therefore driven by a blast wave (a shock with an attached, trailing, rarefaction). While the shock initially deposits vorticity along the interface in a relatively uniform manner, the attached rarefaction deposits secondary baroclinic vorticity opposing the primary vorticity, complicating growth. Hurricane, 2008 approximates the baroclinic vorticity deposition by a shock traveling along a sinusoidally perturbed interface, but incorrectly associates this vorticity solely with a fluctuating component of the vorticity distribution. In Section 2.5.1 I argue that the baroclinic vorticity deposition can be associated with steady shear flow in addition to fluctuating components of the vorticity distribution.

Subsequent KH experiments in the HED regime first modified the experiment of Hurricane and Harding to have a multi-mode spectrum, which led to instability growth dominated by vortex merger [13, 76, 78, 79, 34], see Fig. 1.12. Later experiments on Omega-EP utilized the longer pulse durations (10 ns square pulse per beam) to sustain shock pressure for nearly 30 ns, so that the rarefaction from laser turn-off did not reach the shock for ~ 70 ns [52, 90, 91]. This resulted in KH growth uncomplicated by the rarefaction, providing both the first straightforward measurement of single-mode Kelvin-Helmholtz instability in the HED regime and the first measurement of KH in the supersonic regime whatsoever [52, 90], see Fig. 1.13. Further work on the same platform incorporated a two-mode perturbation to seed KH growth [91].

The oblique case has not been previously addressed from either a design or experimental standpoint in the HED regime. The experimental work presented in this dissertation (Chapter 3) uses a similar spatial perturbation as in the sustained shock RM and KH experiments performed at Omega-EP previously (100 μm wavelength sinusoid with a 10 μm amplitude) [90, 14], but inclines the interface at a 30° tilt with respect to the RM orientation. The resulting interface evolution can be modeled using a regularized Birkhoff-Rott equation, which describes the self-consistent evolution of a vortex sheet. This technique has previously been used to model KH [38, 82] as well as RM and RT [53, 80, 81]. The vorticity distribution required as an initial condition for the computation is calculated using a modified version of the baroclinic circulation deposition
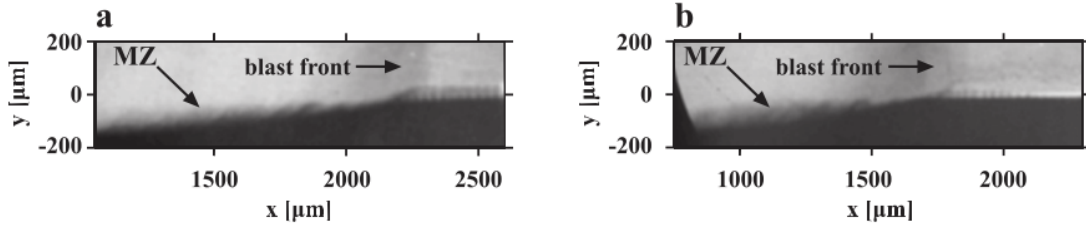
Figure 1.12 This is Fig. 2 from Di Stefano et al., 2014 [13]. Experimental radiographs showing mixing width development on an initially multi-mode interface driven by a blast-wave are pictured. A blast-wave is incident from the left, traveling to the right with the shock front orthogonal to the interface. (a) the top material has a density of 0.05 g cm^{-3} whereas (b) the density is 0.1 g cm^{-3}. The bottom, opaque material has a density of 1.4 g cm^{-3} in both radiographs.
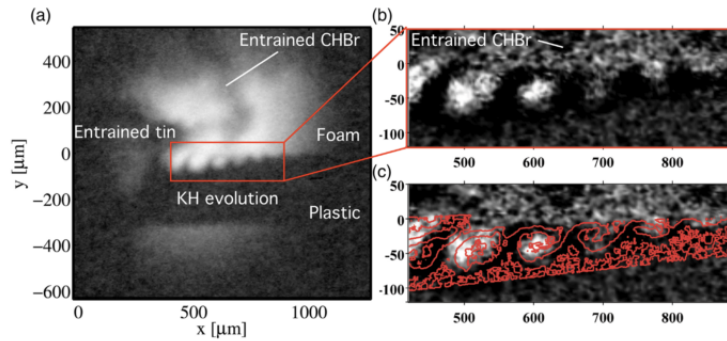
Figure 1.13 This is Fig. 4 from Wan et al. [90]. Left, a radiograph of supersonic KH evolution taken by the SCI is shown. (b) shows a zoom in of the interface with the contrast enhanced. (c) shows interface contours from DAFNA simulations (red lines) overlaid on the interface from experimental radiographs.

calculation from Hurricane, 2008 [32], which has been extended both to include the a tilt between the shock and interface, and to calculate the vorticity distribution in addition to the net vorticity over one wavelength.

1.5 Inertial Confinement Fusion

Inertial Confinement Fusion (ICF) has the potential to provide nigh limitless, clean energy. Fusion refers to the combining of two or more nuclei, leading to some higher atomic number (henceforth, Z) nucleus, and typically some number of other byproducts. If the binding energy per nucleon increases through this reaction, then some amount of energy is released, as some combination of photons and kinetic energy of the reaction byproducts.

Deuterium and tritium mixtures are the fuel used in most modern fusion experiments due to the large DT fusion cross section. Deuterium (D) is a hydrogen atom with a single neutron, and tritium (T) is hydrogen with two neutrons. Assuming that a DT mixture has been heated to maximize its

fusion cross section ($\sim$30 keV) in a uniform sphere with radius r and density ρ, and assuming that an imploded sphere will be confined for one sound speed crossing time, the burn fraction may be estimated as [18]

$$\phi = \frac{\rho r}{\rho r + 6 \text{ g cm}^{-2}},\tag{1.15}$$

where ρr is referred as the areal density (i.e., density per unit area). For a hot spot radius of 10 μm this requires a density of 6 kg cm^{-3}, quite a large number. For reference, the density of solid DT ice is 0.225 g cm^{-3}, and the initial density of the gas fill from which the hot-spot is formed is typically on the order of 0.3 mg cm^{-3}, so that compression of many orders of magnitude is required.

There are three typical strategies used to prepare DT into the required state. Indirect drive with lasers, direct drive with lasers, and pulsed power (Z-pinches). Z-pinches lie outside of my expertise, so I do not discuss them here. In indirect and direct drive, lasers are used to drive several shocks into a spherical capsule. In direct drive, lasers directly irradiate the outside of the capsule, whereas in indirect drive, the lasers irradiate the interior of a high-Z hohlraum. The hohlraum then emits x-rays, irradiating the capsule which is located at the center of the hohlraum.

The capsule consists of some ablator (typically CH, high density carbon, or beryllium), followed by a DT ice layer, and the remainder is filled by low density DT gas, see Fig. 1.14. The implosion assembles the gas fill into an extremely high density "hot-spot", which undergoes fusion, thereby heating the even denser DT ice layer and producing a burn wave. An important metric for the success of an implosion is the energy released by fusion versus the energy required to implode the capsule. If more energy is released by fusion than was required to perform the implosion, the capsule is said to have ignited. As of this writing, no laser-driven ICF experiment has achieved ignition.

Implosion performance is degraded by a number of mechanisms. Both low and high mode asymmetries in the implosion will lead to residual kinetic energy (i.e., at the time of maximum convergence parts of the hot spot will still be in motion), and therefore less compression and heating of the hot spot. High mode asymmetries lead to the injection of both cold DT fuel and higher Z ablator material into the hot-spot; this increases radiative losses therefore cools the hot-spot, increasing the difficulty of achieving ignition. The mix of ablator material into the hot spot was an important and surprising quenching mechanism for early ICF experiments on the National Ignition Facility. Prior to experiments, it was expected that ablator material mix into the hot spot would be limited to $\sim 50 - 75$ ng [25]. However, experiments showed ablator mix masses an order of magnitude larger than this, reducing neutron yields [50, 46]. Subsequent work has reduced the amount of mix and increased yields [49]. Asymmetries also lead to variation in ρr, contradicting the assumptions used in Eq. 1.15.

The growth of higher mode asymmetries is driven primarily by the fluid instability processes
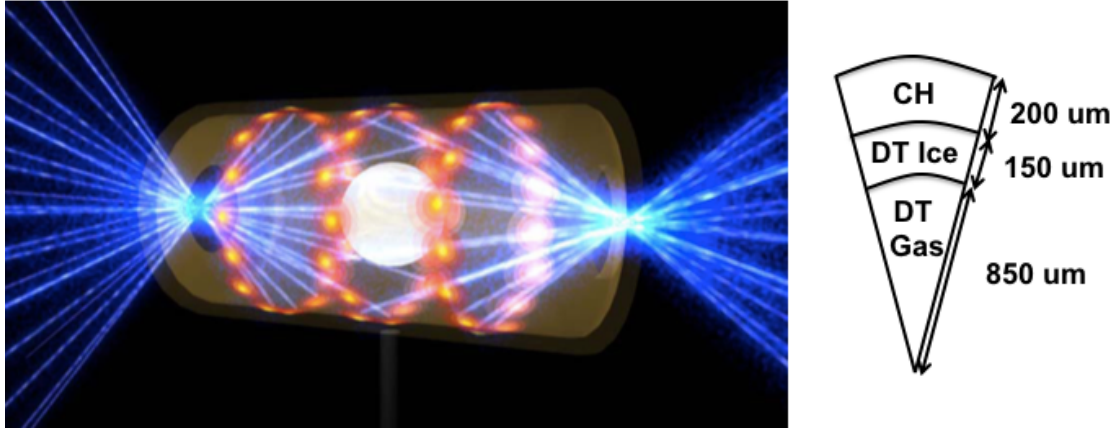
Figure 1.14 Left, an artist's rendition of an indirect drive experiment on NIF is pictured. The cylindrical object is called a hohlraum, made of a high-Z material such as gold. The incoming laser beams heat the hohlraum walls to temperatures of ~ 300 eV, which then emit a bath of thermal x-rays. These x-rays then compress the spherical capsule, which causes fusion. Right, a pie diagram of a typical ICF capsule is shown. The outer layer is the ablator, the DT ice serves as fuel, and the DT gas fill is compressed into a hot-spot, which undergoes fusion. If all goes well, the hot-spot will produce enough energy to cause a propagating burn-wave in the DT fuel.

discussed above. Any initial perturbations on an interface will first grow linearly, due to the Richtmyer-Meshkov process, as each shock crosses it. The perturbations will then grow exponentially via the Rayleigh-Taylor instability as the interfaces experience steady accelerations. Convergence effects also amplify any initial perturbations.

Low mode asymmetries are introduced by drive asymmetries or engineering features, e.g. the thin plastic film used to hold the capsule in place. In addition to disrupting stagnation itself, misalignment between the incoming shock and interfaces will complicate instability growth. When a shock is oblique (i.e. non-normal), it will drive shear flow across an interface in addition to acceleration in the direction of shock propagation. This leads to the Kelvin-Helmholtz instability. This complication motivates this work: how is instability growth modified by oblique shocks and the inclusion of shear flow? Does the presence of low-mode asymmetries in implosions alter the evolution of high-mode asymmetries? Within some limit of small perturbation amplitude and smaller tilt (or small perturbation amplitude and large tilt), the instability growth is dominated by either RM or KH alone early in time. However, even for an interface that is dominated by a single instability early in time, the question of late-time behavior remains, as was discussed above. The higher growth rate and different morphology of self-similar KH as compared to self-similar RM imply that an anomalous transition to KH dominated behavior would have important ramifications for the performance of ICF experiments.

1.6 Contributions

My contributions to the work presented in this dissertation spans both experiment and theory. The experiments presented in Chapter 3 were designed by some combination of Kirk Flippo, Jon Hager, and John Kline as an extension of prior work performed on Omega-EP by Michigan students. However, I was present for the experiments included in Chapter 3, and while I did not plan the experiments, I was put in charge of target alignment and choosing timings on the day. I furthermore analyzed all of the data presented herein. To my knowledge, the experiments presented in Chapter 3 were the first published experiments to observe instability evolution on an oblique interface with a single-mode perturbation.

I was the experimental PI for numerous multi-mode RM experiments using essentially this experimental platform with a different interface perturbation which are published in Di Stefano, 2017 [15]. Carlos Di Stefano performed all of the RAGE simulations seen in this dissertation. Any analysis of RAGE simulations was performed by me except where otherwise noted. The experiment presented in Chapter 4 was designed by me in the sense that I chose the perturbation and experimental timing, however, Di Stefano provided pre-experiment simulations and was the experimental PI.

The novel theory work in Chapter 2 involves the extension of prior descriptions of baroclinic vorticity deposition to oblique interfaces with perturbations. To my knowledge, I present the first calculations of self-consistent vortex sheet evolution in the single-mode oblique case, whereas previous efforts have calculated either the RM only, RT only, or KH only case. I know of no prior single-mode work, either theoretical, experimental, or computational in which interface evolution is dominated by RM while the interface behaves linearly, but evolves to a KH-like state at late times.

The discussion of baroclinic vorticity deposition in Chapter 2, in particular the method given for predicting instability evolution from the baroclinic vorticity deposition, diverges strongly from prior work in the HED regime. I present arguments as to why the new approach is needed in Section 2.5.1.

1.7 Description of chapters

In Chapter 2, I first discuss shock-interface interactions for the heavy-to-light oblique case. I then discuss the deposition of baroclinic vorticity on interfaces via shocks for this case in the limit of weak transmitted and reflected waves. The calculated vorticity distributions are shown to capture both KH and RM experiments well in a qualitative sense. I then consider the oblique case in detail, showing that the vorticity distribution can be used to predict both the early and late-time behaviors of the interface. I will show that certain vorticity distributions lead to instability growth which is

RM-like early in time but KH-like at late times.

In Chapter 3, I will discuss experiments on the Omega-EP laser to measure instability growth which exhibits the mixed behavior described in Chapter 2. I will describe the laser drive, diagnostics, as well as the targets used. RAGE simulations of the experiment will be described as well, and the combination of experimental data and simulation will be used to infer the bulk properties of the hydrodynamics in the experiment. I then compare the theory from Chapter 2 to simulation and experiment.

In Chapter 4, I discuss an experimental schema to produce sets of point vortices with independently varying spatial scales and strengths. This experiment is designed to produce interface evolution which is well described by the discrete vortex model presented in Hurricane, 2008 [32]. I estimate the growth rate for the incompressible, single-mode, case where each vortex has the same size and strength. I then give a dimensionless parameter which describes when compressibility should be important in terms of shock crossing time per wavelength and an eddy turnover time. I present preliminary experimental results, and compare the observed perturbation evolution to both simulation and theory.

Chapter 2

Baroclinic Vorticity Deposition

The interaction of shocks and interfaces is important to the understanding of fluid instabilities in the context of HED experiments. Even for the blast-wave driven RT instability, the shock-interface interaction both determines the post-shock perturbation size and the initial instability velocity (via the RM process). KH experiments in the HED regime utilize shocks to create the bulk shear flows needed to drive the instability. These shock-interface interactions are tied together by baroclinic vorticity deposition: non-parallel density and pressure gradients source vorticity according to

$$\frac{D\vec{\omega}}{Dt} + \vec{\omega}\nabla \cdot \vec{u} - \vec{\omega} \cdot \nabla\vec{u} = \left[\frac{\nabla\rho \times \nabla p}{\rho^2}\right]_{\text{baroclinic}} \tag{2.1}$$

where $\frac{D}{Dt}$ is the convective derivative, $\vec{u}$ is the velocity, $\vec{\omega} = \nabla \times \vec{u}$ is the vorticity, p is the pressure, and ρ is the density. In HED hydrodynamic instability experiments, the strongest (and therefore most important) pressure gradient is often the primary shock, and the strongest density gradient is often the contact surface on which instabilities grow.

The integral amount of vorticity over some surface of integration, referred to as the circulation, is useful when considering the bulk properties of an interface as it relates to the shear across an interface in a straightforward manner. It is calculated by

$$\Gamma = \iint_S \vec{\omega} \cdot d\vec{S} = \iint_S (\nabla \times \vec{u}) \cdot d\vec{S} = \oint_{\partial S} \vec{u} \cdot d\vec{\ell}, \tag{2.2}$$

where S is some surface of integration, $\vec{S}$ is the local surface normal of S, ∂S is the boundary of S, and $\vec{\ell}$ is everywhere parallel to ∂S. I assume two-dimensional Cartesian symmetry in the rest of this work, so that vorticity only has a non-zero value in the $\hat{z}$ direction. So long as the flow is incompressible (i.e. $\nabla \cdot u = 0$) the velocity in all space may be calculated from the vorticity using a Biot-Savart law. For a point vortex (also referred to as a vortex filament as it extends infinitely in the z direction) at the origin the flow in the surrounding fluid is given by

$$\vec{u} = \frac{\Gamma}{2\pi r}\hat{\phi}, \tag{2.3}$$

27

where Γ is referred to as the vortex strength, r is the distance from the origin, and $\hat{\phi}$ is the azimuthal basis vector for a polar coordinate system. This follows from symmetry considerations and the definition of Γ. Eq. 2.3 can be extended to a point vortex at $\vec{x}'$ and a test point at $\vec{x}$ by

$$\vec{u}(\vec{x}, \vec{x}') = \frac{\Gamma}{2\pi|\vec{x} - \vec{x}'|}\hat{z} \times \frac{\vec{x} - \vec{x}'}{|\vec{x} - \vec{x}'|} \tag{2.4}$$

Eq. 2.4 is directly analogous to the calculation of the magnetic field at point $\vec{x}$ due to an infinitely long, straight, wire carrying uniform current at point $\vec{x}'$.

If the vorticity is distributed along a line (referred to as a vortex sheet) rather than concentrated at a single point, the velocity at a single point is instead given by the integral [80]

$$\vec{u}(\vec{x},t) = \frac{1}{2\pi}\int_{-\infty}^{\infty} ds \left[\frac{d\Gamma}{ds}(s,t)\hat{z} \times \frac{\vec{x} - \vec{x}'(s,t)}{|\vec{x} - \vec{x}'(s,t)|^2}\right], \tag{2.5}$$

where s parameterizes the vortex sheet and $d\Gamma/ds$ is the circulation per unit length or vortex sheet strength. When written in terms of complex numbers, this is known as the Birkhoff-Rott equation [39]. If one restricts $\vec{x}$ to lie along the vortex sheet, this equation may be used to calculate the self-consistent evolution of the vortex sheet in the limit that there is no secondary baroclinic vorticity deposition, i.e. no additional vorticity is created during vortex sheet evolution. In general, this assumption only holds in the limit of small Atwood number. Regularized and discretized versions of this equation have previously been used to model the Kelvin-Helmholtz instability [38]. Versions of this calculation with the vorticity assumed to be localized to points at the centers of vortices have also been used when modeling the late time behavior of both RM [65] and KH [64]. This localized vorticity assumption has also been used when modeling shock wave driven KH in the HED regime [32]. More sophisticated formulations can take steady deposition of baroclinic vorticity deposition by secondary processes into account so long as the flow remains incompressible. This formulation of vortex sheet evolution also allows the modeling of RT and late-time processes in RM [80, 81].

While vortex sheet computations have previously been used to model all of RM, RT, and KH, to my knowledge it has never been used to model the combined RM, RT, and KH instabilities which occur on shocked, sinusoidally perturbed, oblique interfaces. In this chapter, I will first discuss baroclinic vorticity deposition by shocks on oblique interfaces with no perturbation. This treatment will closely follow the discussion of Samtaney, 1998 [72] which fully takes into account the reflected and transmitted waves. The assumptions which underly this calculation break down for some relevant tilts and density discontinuities across interfaces which are relevant to the HED regime. When treating oblique interfaces with perturbations I therefore use the approximation of Hurricane, 2008 [32], which neglects the transmitted and reflected waves when calculating the amount of vorticity deposited by the shock-interface interaction. Hurricane calculated the amount

of circulation deposited per wavelength along a sinusoidally perturbed interface by a shock in the KH geometry (with the shock front orthogonal to the mean interface). I extend this calculation to arbitrary tilts between the mean interface and shock, and furthermore calculate the vorticity distribution along the interface. I then estimate interface evolution using a vortex sheet model, and discuss what can be predicted about interface evolution both qualitatively and quantitatively using this approximation.

2.1 Shock fronts incident on parallel interfaces (non-oblique shocks)

A sufficiently strong shock incident on a discontinuity in density, pressure, or polytropic index will typically produce both a reflected and transmitted wave, see Fig. 2.1. The transmitted wave is typically a shock, whereas the reflected wave is either a shock or a rarefaction depending on the sound speeds on either side of the pre-shock interface. When the shock is incoming in the material with the faster sound speed the reflected wave will be a shock, whereas when the shock is incoming in the material with slower sound speed the reflected wave is a rarefaction. These regimes are therefore sometimes referred to as "fast/slow" and "slow/fast", respectively. The sound speed in a polytropic gas is given by $c_s = \sqrt{\gamma p / \rho}$, so that a lighter material will be "faster" and a heavy material will be "slower" provided that the materials have the same polytropic index and pressure. The "slow/fast" and "fast/slow" regimes are also referred to as "heavy-to-light" and "light-to-heavy", respectively, for this reason. The jargon of "heavy-to-light" and "light-to-heavy" are used almost exclusively in the HED hydrodynamic instability literature, so I will typically use that jargon here. The case of a normally incident shock is not relevant in a quantitative sense to the rest of this dissertation, so I point you to Drake, 2006 [18] for a detailed solution.

2.2 Oblique shock interface interactions in the heavy-to-light case

At first glance, the inclusion of a finite tilt between the interface and shock appears to significantly complicate the picture above. However, in the centered case all waves in the system emanate from a single point, referred to as the node, and the math becomes simpler as the entire problem may be solved in one reference frame. A schematic of the oblique shock-interface interaction in the heavy-to-light case is shown in 2.2. The node is at the intersection of the shock and interface, and I will solve the problem in the frame of this node. Let θ be the angle between the shock and interface,
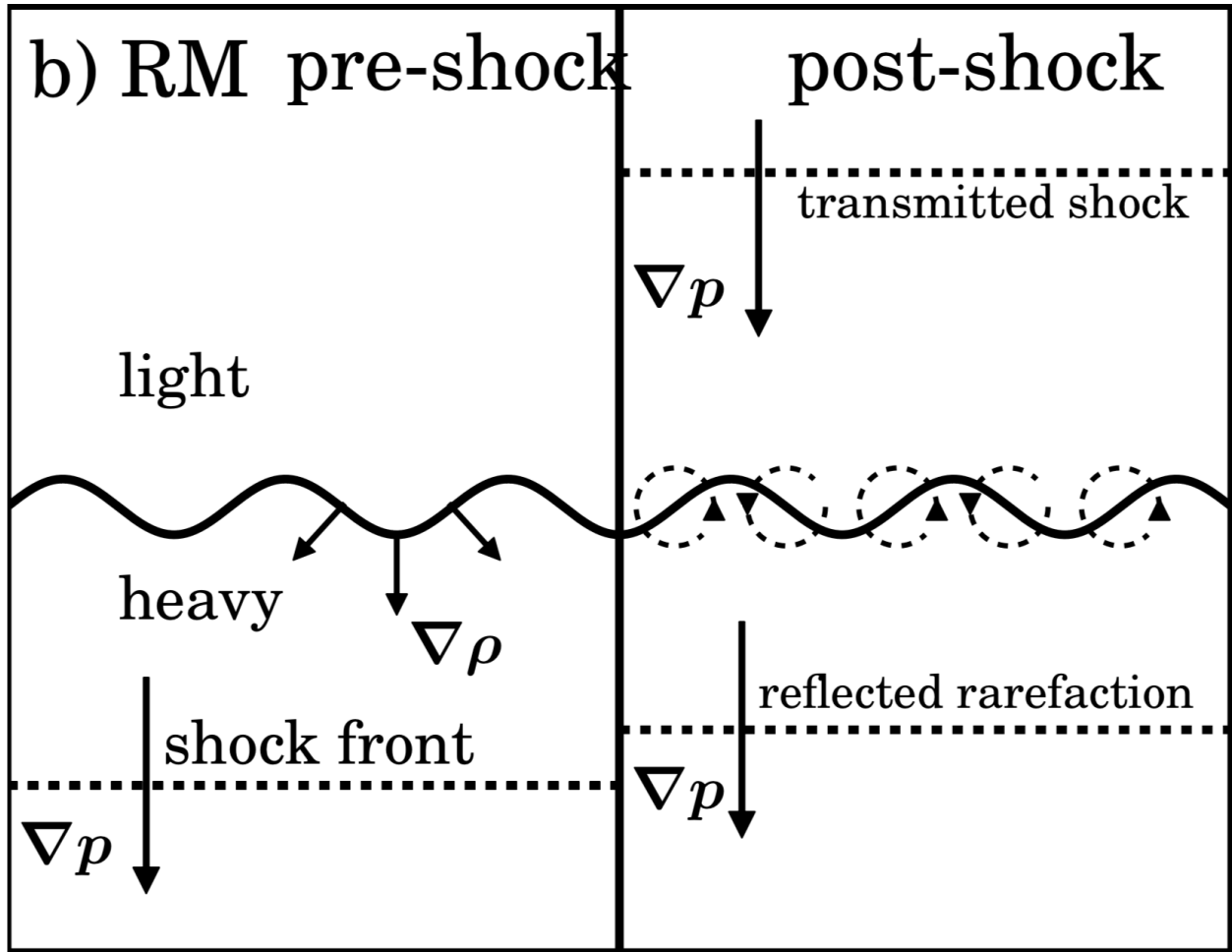
Figure 2.1   A figure showing the typical shock-interface interaction in the heavy-to-light case. Left, a shock in incident from the bottom. Right, the incoming shock has interacted with the interface, producing a transmitted shock and reflected rarefaction. In the light-to-heavy case a reflected shock will occur rather than a reflected rarefaction. Shocks propagate anti-parallel to the associated pressure gradient, whereas rarefactions propagate parallel to their pressure gradient.

so that they are parallel when $\theta = 0$, define the lab frame to be one where the pre-shock interface is at rest (i.e. the pre-shock heavy and light materials are at rest), and define u_s to be the shock speed in the lab frame. The node frame tracks the shock-interface interaction point so that it is stationary, and therefore must move up with speed u_s and right with speed $u_s/\tan\theta$ relative to the lab frame. In the node-frame, the pre-shock material is flowing parallel to the pre-shock contact surface with speed $u = u_s/\sin\theta$. A schematic of the flow in this frame is shown in Fig. 2.3.

The upstream materials, i.e. the pre-shock heavy and light materials, are both incident with velocity u. However, their Mach numbers will be different as

$$\frac{M_H}{M_L} = \frac{c_L}{c_H} = \frac{\sqrt{\gamma_L p_L/\rho_L}}{\sqrt{\gamma_H p_H/\rho_H}}. \tag{2.6}$$
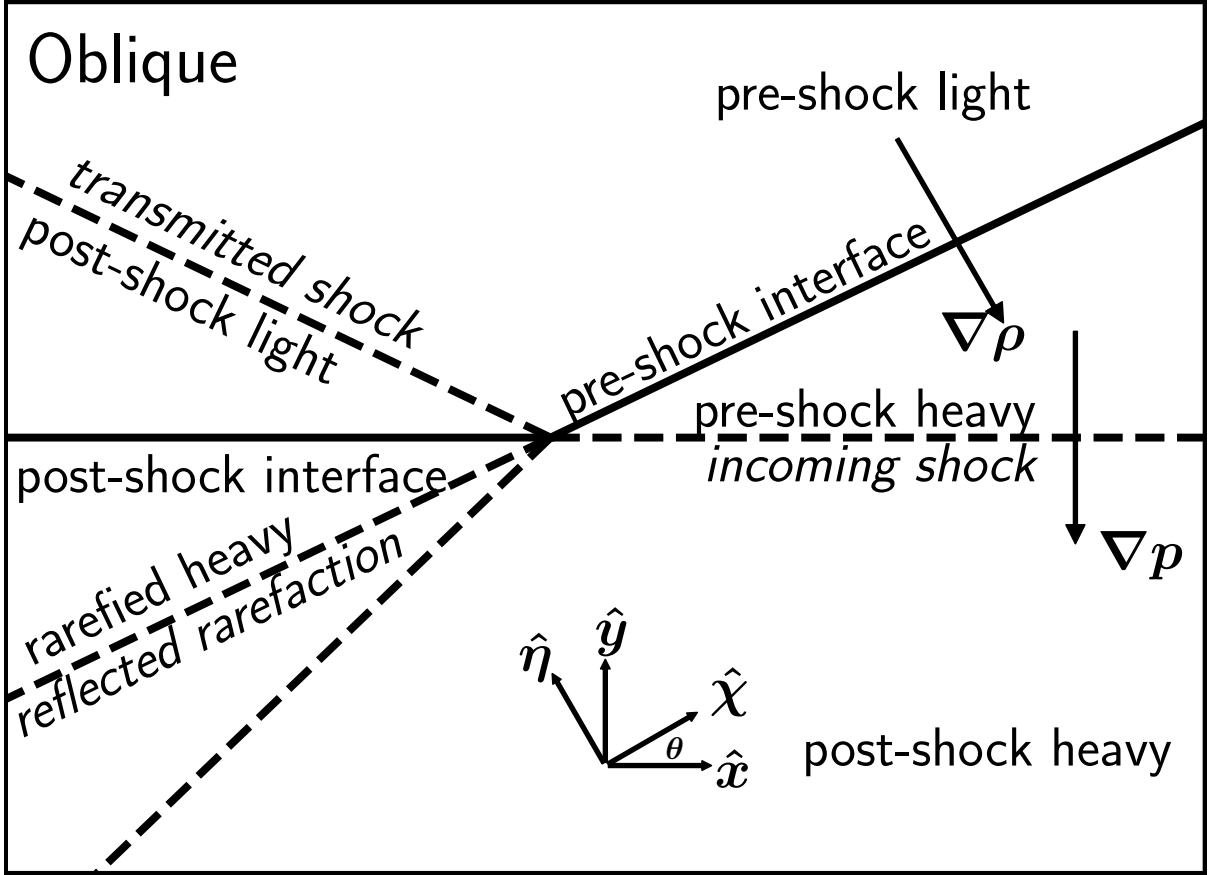
Figure 2.2 A schematic of the oblique shock, interface interaction. Waves are labeled in italics, whereas material regions and interfaces are not. As no velocities (or quantities directly dependent on velocity) are shown, this schematic is frame invariant under Galilean transformation.

Where H and L refer to the heavy and light regions respectively. Assuming that the materials are isobaric pre-shock and have the same polytropic index this becomes:

$$\implies \frac{M_H}{M_L} = \sqrt{\frac{\rho_H}{\rho_L}}. \tag{2.7}$$

Three waves are required to solve the oblique shock-interface interaction. An incoming shock, as well as a transmitted shock and reflected wave, either a rarefaction or shock. The rarefaction here takes the form of a Prandtl-Meyer expansion fan, i.e. the rarefaction of a supersonic flow around a sharp corner [11]. In the heavy-to-light case the reflected wave will be a rarefaction, whereas in the light-to-heavy case it will be a shock, similar to the non-oblique case. In order to solve for the transmitted and reflected wave properties two boundary conditions are required: the post-shock flow must have the pressure on either side of the post-shock contact surface, and there must be no material flux across the post-shock contact surface. The no material-flux condition takes the form of
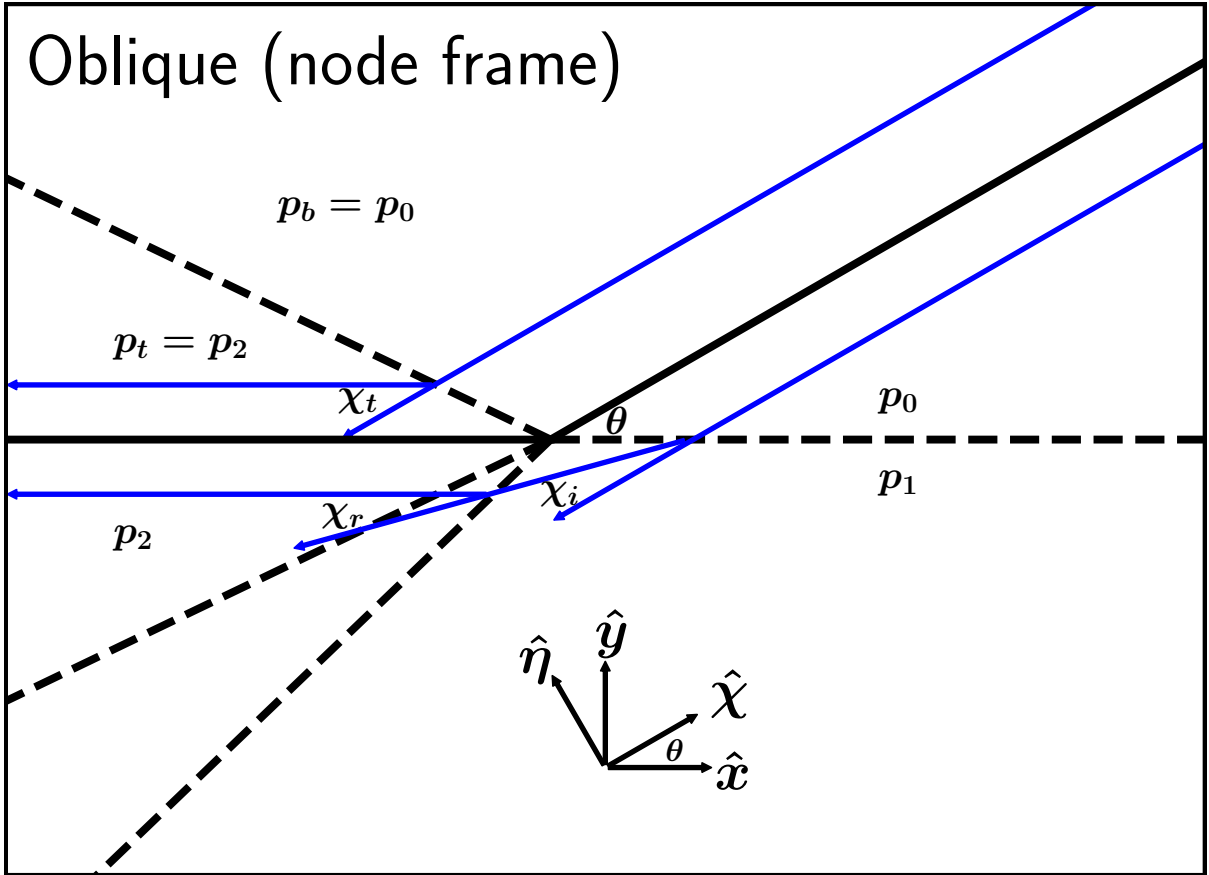
Figure 2.3 A schematic of the oblique shock-interface interaction in the frame of the interaction node. Each of the waves is stationary in this frame. The material regions are labelled as follows: region b is the pre-shock light, region t is the post-shock light, region 0 is the pre-shock heavy, region 1 is the post-shock heavy, and region 2 is the rarefied heavy. χ_t is the flow deflection angle across the transmitted shock, χ_i is the deflection angle across the incoming shock, and χ_r is the deflection angle across the rarefaction. The flows in the pre-shock regions are parallel to the pre-shock interface, and the flows in regions t and 2 are parallel to the post-shock interface. This implies that $\chi_t = \chi_i + \chi_r$. The flow directions and deflection angles are not invariant under Galilean transformation, so that this schematic is only valid in the node-frame.

a constraint on flow direction: the flow on either side of the contact surface must be parallel to it in the node frame, see Fig. 2.3. Is this figure, p_0 is the pressure of the pre-shock heavy material, p_1 is the pressure of the post-shock heavy material, p_2 is the pressure in the rarefied heavy material, p_b is the pressure of the pre-shock light material, p_t is the pressure of the post-shock light material, χ_i is the flow deflection angle across the incoming shock, χ_t is the deflection angle across the transmitted shock, and χ_r is the flow deflection angle across the rarefaction.
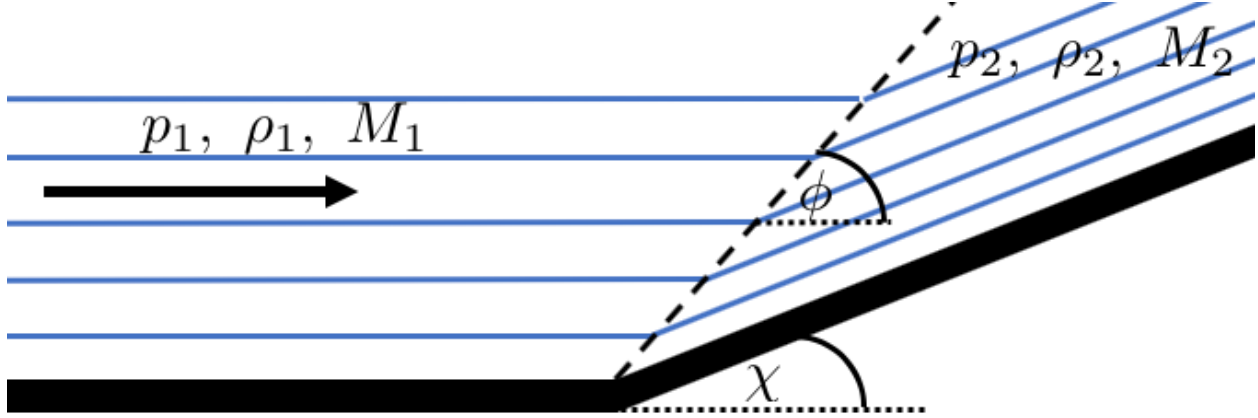
Figure 2.4 An image of a supersonic flow incident on a corner bent into the flow, which results in an oblique shock. The oblique shock bends the flow to be parallel to the interface in this context.

2.2.1 Oblique shocks

The simplest context in which an oblique shock occurs is a supersonic flow incident past a corner bent "into" the flow, see Fig. 2.4. The flow is deflected a set angle so that it is parallel to the outgoing boundary. The jump conditions across an oblique shock are given by [43]

$$
\begin{aligned}
p_2 &= p_1 \left(1 + \frac{2\gamma}{\gamma+1}(M_1^2 \sin^2\phi - 1) \right), \\
\rho_2 &= \rho_1 \left(\frac{2(M_1^2 \sin^2\phi - 1)}{(\gamma-1)M_1^2 \sin^2\phi + 2} \right), \\
\cot\chi &= \tan\phi \left[\frac{(\gamma+1)M_1^2}{2(M_1^2 \sin^2\phi - 1)} - 1 \right], \text{ and} \\
M_2^2 &= \frac{2+(\gamma-1)M_1^2}{2\gamma M_1^2 \sin^2\phi - (\gamma-1)} + \frac{2M_1^2 \cos^2\phi}{2+(\gamma-1)M_1^2 \sin^2\phi}.
\end{aligned}
\tag{2.8}
$$

These parameters are shown in Fig. 2.4. The indices 1 and 2 denote the upstream and downstream quantities respectively, p is the pressure, ρ is the density, γ is the polytropic index, ϕ is the angle of the shock relative to the incoming flow, and χ denotes the deflection angle of the flow across the oblique shock.

2.2.2 Rarefactions around corners: Prandtl-Meyer expansion fans

In contrast, a Prandtl-Meyer expansion fan occurs when a supersonic flow is incident on a sharp corner bent "away from" the flow, see Fig. 2.5. While the gradient in material properties is of finite extent, the solution may be found in terms of the properties at the upstream and downstream edges
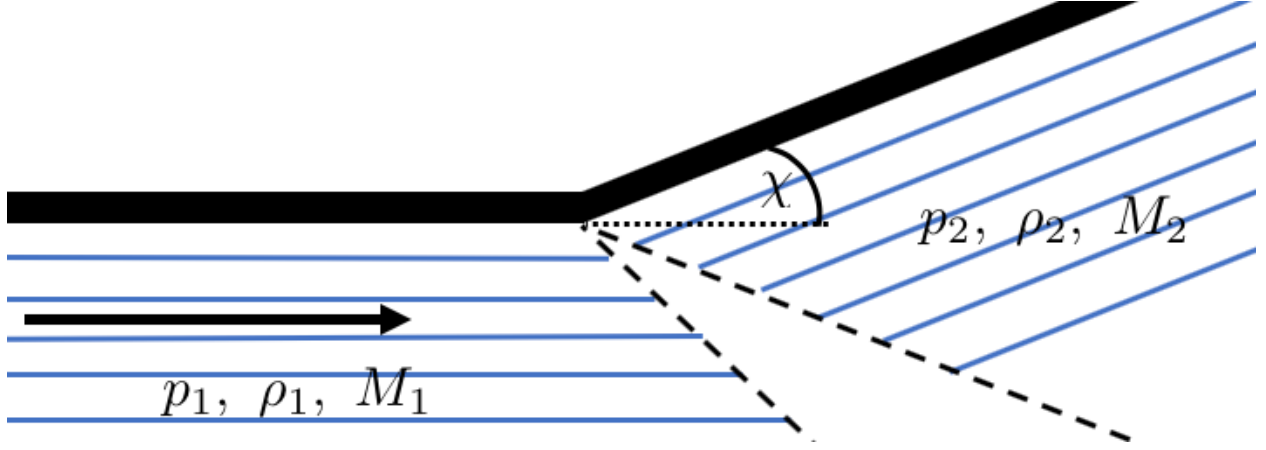
Figure 2.5   An image of a Prandtl-Meyer expansion fan (i.e. rarefaction around a corner). The corner is bent "out of" the supersonic flow, which decompresses while turning the corner. The rarefaction bends the flow so that it is parallel to the post-corner interface in this context.

of the expansion fan alone. The upstream edge refers to the pre-rarefaction material, and the down-stream edge to the post-rarefaction material. The fan extends at the Mach angle, $\alpha = \sin^{-1}(1/M)$, relative to the flow on either side of the fan. The change in fluid parameters across a Prandtl-Meyer expansion fan is given by the set of equations [43]:

$$
\begin{aligned}
p_2 &= p_1 \left(\frac{1 + \frac{\gamma-1}{2} M_1^2}{1 + \frac{\gamma-1}{2} M_2^2} \right)^{\gamma/(\gamma-1)}, \\[2mm]
\rho_2 &= \rho_1 \left(\frac{1 + \frac{\gamma-1}{2} M_1^2}{1 + \frac{\gamma-1}{2} M_2^2} \right)^{1/(\gamma-1)}, \\[2mm]
\chi &= v(M_2) - v(M_1), \text{ and} \\[2mm]
v(M) &= \sqrt{\frac{\gamma+1}{\gamma-1}} \arctan \sqrt{\frac{\gamma-1}{\gamma+1}(M^2 - 1)} - \arctan \sqrt{M^2 - 1}.
\end{aligned}
\tag{2.9}
$$

These parameters are shown in Fig. 2.5. The indices 1 and 2 denote the upstream and downstream quantities respectively, p is the pressure, ρ is the density, γ is the polytropic index, $v(M)$ is called the Prandtl-Meyer function, and χ denotes the deflection angle of the flow across the rarefaction.

2.2.3   Solving for the transmitted and reflected waves

The interaction of an oblique shock with an interface may be thought of as coupled oblique shocks and rarefactions. The equations above are oriented towards solving the individual problems for a set

34

deflection angle (set by the angle of a corner either into or out of the flow). As was stated above, the post-shock flow in both materials must be isobaric and parallel. Each of these boundary conditions may be calculated from the initial conditions given the jump conditions for oblique shocks and PM expansion fans. To solve for the deflection angle across the transmitted and reflected waves, the pressure, density, and polytropic index of the pre-shock materials are typically specified in addition to the incoming shock speed, u_s, and the mean tilt between the interface and incoming shock, θ.

Assuming that the initial pressures in the pre-shock materials are equivalent ($p_0 = p_b$), the pressure boundary condition at the post-shock contact surface may be simplified as follows

$$
\begin{aligned}
p_t &= p_2 \\
\implies p_b \frac{p_t}{p_b} &= p_1 \frac{p_2}{p_1} \\
\implies p_b \frac{p_t}{p_b} &= p_0 \frac{p_1}{p_0} \frac{p_2}{p_1} \\
\implies \frac{p_t}{p_b} &= \frac{p_1}{p_0} \frac{p_2}{p_1}.
\end{aligned}
\tag{2.10}
$$

I have explicit expressions for each of these fractions in Eqs. 2.8 and 2.9 in terms of the shock angle and post-fan Mach number.

As the incoming flows are initially parallel, and the flows at the post-shock contact surface are also parallel, the boundary condition for flow direction can be restated as the requirement that flow deflection is equivalent in both materials. This can be stated as

$$
\chi_i + \chi_r = \chi_t,
\tag{2.11}
$$

where the indices refer to the deflection through each wave. That is, i, r, and t refer to the incident, reflected, and transmitted waves respectively.

In a practical sense, one way to solve the problem is to note that the pressure jumps and flow deflections across each wave are functions of the same parameters, so that if the deflection angles across each wave are known the pressure jumps are also known. One can numerically compute the pressure jumps as a function of deflection angle and determine at which deflection angle the pressures are equal across the post-shock contact surface to find the solution. I have posed the problem with the upstream parameters of the materials known, however, the problem may also be solved for different sets of knowns. E.g., the downstream fluid properties and incoming shock speed could be specified and the upstream fluid properties found.

The amount of shear flow across the interface can be extracted from the Mach numbers and sounds speeds in the post shock-regions, i.e. $\Delta v = c_2 M_2 - c_t M_t$. Shear is invariant under Galilean transformation, so that this is also Δv in the lab frame. Recalling that the circulation is defined as

$\Gamma = \oint \vec{u} \cdot d\ell$, the circulation in a length L along the post-shock interface is $\Gamma(L) = L\Delta v$.

2.3 Baroclinic vorticity deposition on high-Atwood number oblique interfaces

The calculation in the previous section holds so long as the shock-interface interaction is centered, which is typically the case at smaller tilts between the interface and shock. In particular, the interaction may be uncentered in the KH case ($\theta = 90°$), as the post-shock heavy material will be subsonic relative to the shock and therefore the node. This does not guarantee that the shock-interface interaction will be uncentered, but does make the state of the post-shock incoming material (including centeredness) dependent on downstream boundary conditions [11]. Previous work in the HED regime has calculated baroclinic vorticity deposition in the KH geometry from the pressure gradient from the incoming shock and density gradient from the pre-shock contact surface alone, see Hurricane, 2008 [32]. This solution necessarily loses some accuracy by ignoring the transmitted and reflected waves. In the rest of this section, I extend the work in Hurricane, 2008 to include both the effects of a mean tilt between the shock and interface, as well as to calculate the vorticity distribution along the interface. After calculating the vorticity distribution along the post-shock interface, I will use vortex sheet methods to predict interface evolution from the calculated vorticity distribution.

A schematic of the oblique shock-interface interaction, including a perturbation, is shown in Fig 2.6. As above, there are three waves in the system: the incoming shock, the transmitted shock, and the reflected rarefaction. In both the KH and RM literatures, the x ordinate is typically taken to span the interface. The choice of co-ordinate system is simpler in those frames as the orientation of the interface remains relatively unchanged between the pre- and post-shock systems. When interpolating between the RM and KH geometries, I could recover both of these orientations by choosing the x-axis to always be aligned with the pre-shock interface. However, In the following sections I will be discussing system evolution in the approximation that the post-shock interface is nearly parallel to the incoming shock, and as such I choose the x-axis to align with the primary shock front (and therefore post-shock interface). This choice of frame should not impact the result of the calculation. Rather, the coordinate frame has been chosen to be convenient for the calculation of the post-shock system evolution. The calculations of circulation and vorticity should only be considered accurate to an overall factor of (± 1), the correct sign can be determined by ensuring the correct bulk inversion behavior after shock crossing in RM-like cases, or by ensuring that rollups form in the correct orientation in KH-like cases.

The vorticity and circulation along the interface are calculated by integrating the vorticity
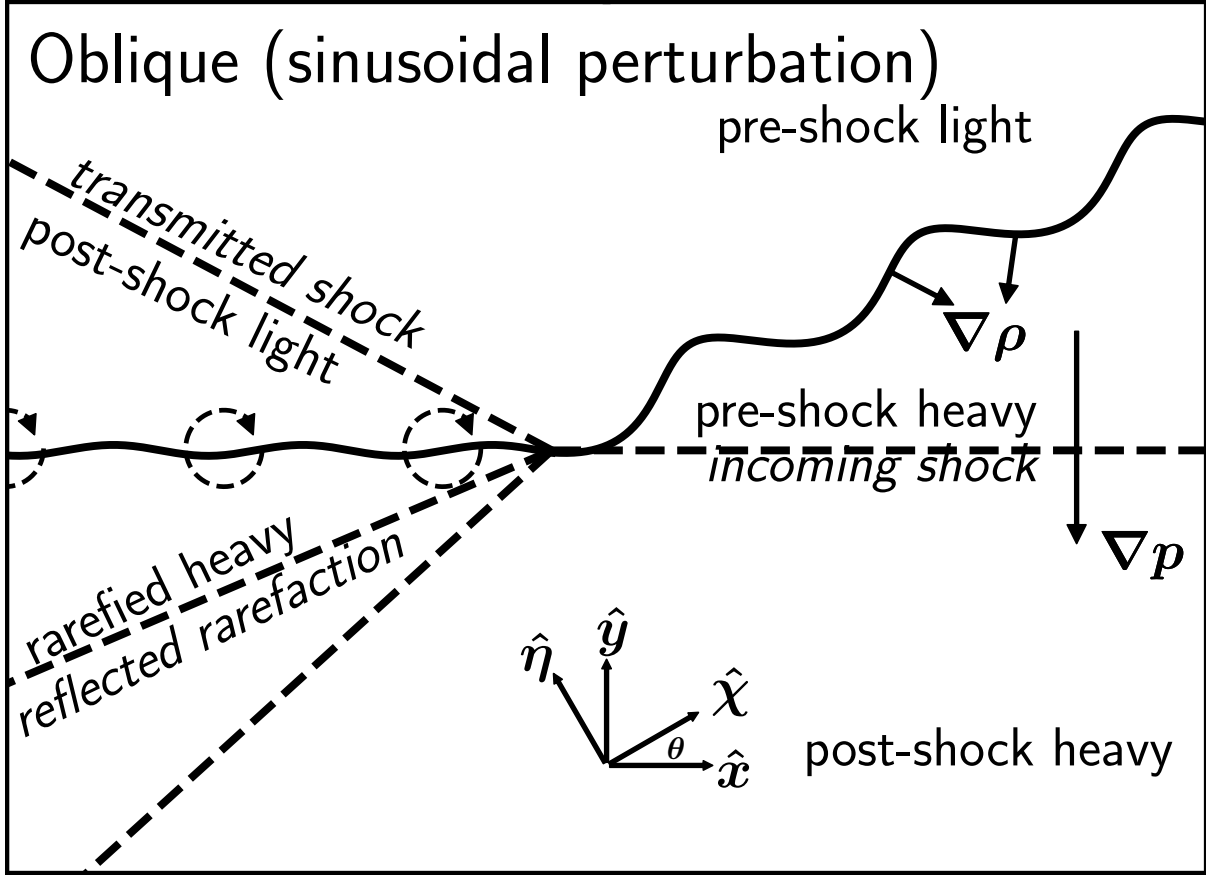
Figure 2.6 A schematic of the oblique shock, interface interaction is shown. The primary shock is incident from the bottom, traveling in the $+\hat{y}$ direction.

equation, Eq. 2.1. This work extends the procedure in Hurricane [32] to include the calculation of the vorticity distribution, as well as the inclusion of an arbitrary tilt of the shock relative to the mean interface structure. Hydrodynamic instability experiments in the HED regime typically utilize perturbations with 2D Cartesian symmetry. These experiments are typically limited to imaging diagnostics which integrate through the line-of-sight, so that only two-dimensions can be resolved. As such, I assume 2D Cartesian symmetry, with $\hat{z}$ as the symmetry direction, for the interface perturbations going forward. Thus, $\hat{z}$ is out of the page in Fig. 2.6.

Using the co-ordinate frame shown in Figs. 2.2, 2.3, and 2.6, this simplifies the vorticity equation (Eq. 2.1) by implying $\frac{\partial}{\partial z} = 0$. As a consequence, $\vec{\omega} = \omega \hat{z}$ and $\vec{\omega} \cdot \nabla = \omega \frac{\partial}{\partial z} = 0$. To first order, $\nabla \cdot \vec{u}$ is zero everywhere other than the waves in the system, and $\vec{\omega}$ is zero upstream of the shock. Therefore, the third term of Eq. 1.1 is zero, and to first order the second term is limited to the deformation of the interface, which will be calculated later, and as such is assumed to be zero here.

The circulation deposited along the interface over some finite interval may then be calculated by

integrating the vorticity equation over all time, over all y, and over some interval in x:

$$\Gamma(x) = \int_{-\infty}^{\infty} dt \int_{-\infty}^{\infty} dy \int_0^x dx' \left[\frac{D\vec{\omega}}{Dt} \right]$$
$$= \int_{-\infty}^{\infty} dt \int_{-\infty}^{\infty} dy \int_0^x dx' \left[\frac{\nabla\rho \times \nabla p}{\rho^2} \right]. \tag{2.12}$$

Similarly, the vorticity distribution is calculated by integrating the vorticity equation over all time alone:

$$\omega(x,y) = \int_{-\infty}^{\infty} dt \left[\frac{D\vec{\omega}}{Dt} \right]$$
$$= \int_{-\infty}^{\infty} dt \left[\frac{\nabla\rho \times \nabla p}{\rho^2} \right]. \tag{2.13}$$

In order to proceed $\nabla\rho$, ∇p, and ρ must be defined in sufficient detail that they can be numerically integrated.

The shock is assumed to be propagating in the $+\hat{y}$ direction, so that the shock front extends in the $\hat{x}$ direction. The pressure, and pressure gradient due to the shock in the heavy material is given by

$$p = \Delta p H(u_s t - y) + p_o$$
$$\nabla p = -\Delta p \delta(y - u_s t)\hat{y}, \tag{2.14}$$

where Δp is the pressure jump across the shock, δ is the Dirac delta, u_s is the shock speed in the heavy material, and H is the Heaviside step function. These equations describe a pressure discontinuity of magnitude Δp traveling with speed u_s in the $+\hat{y}$ direction.

The density and density gradient are respectively given by:

$$\rho = \Delta\rho H((-1)(y - y_1(x))) + \rho_L$$
$$\nabla\rho = -\Delta\rho \delta((-1)(y - y_1(x)))\hat{n}, \tag{2.15}$$

where $\Delta\rho$ is the density jump across the interface, ρ_L is the density of the light material, $H(x)$ is the Heaviside step function, $y_1(x)$ defines the pre-shock interface location, and $\hat{n}$ is the surface normal of the interface. These equations describe a density discontinuity across the curve $y_1(x)$ with magnitude $\Delta\rho$, with the heavier material below the curve. This representation assumes that the curve is a function of x, if the curve is not a function of x a sum of Heaviside step functions and Dirac deltas might instead be required.

A schematic of the shock interface interaction in the oblique case is shown in Fig. 2.6. The

x, *y* co-ordinate system is the natural co-ordinate system of the shock, so that the shock front is parallel to $\hat{x}$, and the shock propagates along $\hat{y}$. The χ, η co-ordinate system is taken to be the natural co-ordinate system of the pre-shock interface, so that $\hat{\chi}$ is aligned with the mean interface, and $\hat{\eta}$ is aligned with the perturbation. The tilt of the interface, θ, is then given by $\hat{\chi} \cdot \hat{x} = \cos\theta$. A graphical representation of the relation between the two co-ordinate frames is shown towards the bottom of Figs. 2.2, 2.3, and 2.6.

Up until this point, no assumption has been made about the structure of the interface. Going forward, I will assume a sinusoidal perturbation. This is largely done out of convention, as sinusoids are the typical spatial structure used in instabilities given that simple solutions can be found for the evolution of these perturbation structures for RM, KH, and RT in the linear regime. A single sinusoid is a single point in Fourier space, and is a natural way to interpret interface structure. In Chapter 4 I will discuss a different type of interface structure.

Let $\vec{\gamma}(\tau)$ be a parameterization of the pre-shock interface. Then, in the χ, η co-ordinate system, I define the interface by

$$
\begin{aligned}
\vec{\gamma}(\tau) \cdot \hat{\chi} &= \tau \text{ and} \\
\vec{\gamma}(\tau) \cdot \hat{\eta} &= a\sin(k\tau).
\end{aligned}
\tag{2.16}
$$

The variable τ corresponds to length along the mean interface axis. The surface normal is then given by

$$
\hat{n}_{\chi,\eta}(\tau) = \frac{\hat{\eta} - ka\cos(k\tau)\hat{\chi}}{\sqrt{1 + (ka)^2\cos(k\tau)^2}},
\tag{2.17}
$$

where $\hat{\eta}$ and $\hat{\chi}$ are shown in Fig. 2.6. This is transformed into the *x*, *y* frame by

$$
\hat{n}_{x,y}(\tau) = (\hat{n}_{\chi,\eta}(\tau) \cdot \hat{x})\hat{x} + (\hat{n}_{\chi,\eta}(\tau) \cdot \hat{y})\hat{y}.
\tag{2.18}
$$

The map $y_1(x) = \vec{\gamma}(\tau_x(x)) \cdot \hat{y}$ may then be calculated numerically, where $\tau_x(x)$ is the numerically calculated inverse of $\vec{\gamma}(\tau) \cdot \hat{x}$. Similarly, $\tau_y(y)$ is defined to be the numerically calculated inverse of $\vec{\gamma}(\tau) \cdot \hat{y}$. $\tau_x(x)$ and $\tau_y(y)$ may not be functions depending on the tilt and perturbation, in which case care must be taken to define appropriate sections along the curve. The cross product $\hat{n} \times \hat{y}$ will be required for computations and may be calculated from Eq. 2.18 to be

$$
\hat{n} \times \hat{y}(\tau) = (-1)\frac{\sin\theta + ka\cos\theta\cos(k\tau)}{\sqrt{1 + (ka)^2\cos(k\tau)^2}}\hat{z}.
\tag{2.19}
$$

Substituting Eqs. 2.14, 2.15, and 2.17 into Eq. 2.12 to calculate the circulation yields

$$
\Gamma(x) = \frac{\Delta p \Delta \rho}{\bar{\rho}^2} \int_{-\infty}^{\infty} dt \int_{-\infty}^{\infty} dy \int_{0}^{x} dx' [\delta(y - y_1(x'))
$$
$$
\delta(y - u_s t) \hat{n} \times \hat{y}],
$$
(2.20)

where $\bar{\rho} = (\rho_H + \rho_L)/2$

Evaluating the integral over x' and y, and assuming $y_1(x)$ is monotonic, the circulation becomes

$$
\Gamma(x) = \frac{\Delta \rho \Delta p}{\bar{\rho}^2} \int_{0}^{y_1(x)/u_s} dt [\hat{n} \times \hat{y}(\tau_t(t))],
$$
(2.21)

where $\tau_t(t) = [\tau_y(y)]_{y=u_s t}$. When $y_1(x)$ is non-monotonic, the integral must be evaluated separately between extrema, and appropriate sections $\tau_y(y)$ must be used in each subdomain. As one would expect, when $\theta = 90°$ the above derivation of the circulation becomes nearly identical to that in Hurricane, 2008 [32].

Substituting Eqs. 2.14, 2.15, and 2.17 into Eq. 2.13 to calculate the vorticity distribution:

$$
\omega(x,y) = \frac{\Delta p \Delta \rho}{\bar{\rho}^2} \int_{-\infty}^{\infty} dt [\delta(y - y_1(x))
$$
$$
\delta(y - u_s t) \hat{n} \times \hat{y}].
$$
(2.22)

Evaluating the integral over t, the vorticity becomes

$$
\omega(x,y) = \frac{\Delta p \Delta \rho}{u_s \bar{\rho}^2} \delta(y - y_1(x)) \hat{n} \times \hat{y}.
$$
(2.23)

The resulting vorticity and circulation distributions along a single wavelength for several tilts and perturbation amplitudes are plotted in Fig. 2.7. In each case, the abscissa of the plot is taken to be along the mean position of the post-shock interface. For the plot of the vorticity distribution, $\omega(x)$, the Dirac delta is disregarded and assumed to have units of $1/\mu$m. The wavelength for all perturbations is 100 μm, which is a typical wavelength used in HED hydrodynamic instability experiments.

Eqs. 2.21 and 2.23 are suspect at extremely large density gradients. Consider the case of a shock in a light material next to a much denser material in the KH geometry. If $\rho_H \gg \rho_L$ the heavy material should act as a rigid boundary, so that it remains relatively unperturbed by the shock in the light material. This would imply that the circulation per unit length should asymptote to some constant determined by the post-shock fluid speed in the light material. However, Eqs. 2.21 and 2.23 predict that the density dependence goes as $\Gamma \propto \Delta \rho / \bar{\rho}^2$ which goes to zero when $\rho_H \to \infty$.

In Fig. 2.7a typical features of vorticity distribution leading to KH growth can be seen ($\theta = 90°$).

When $\sin\theta \gg ka\cos\theta$, as in this case, the vorticity takes on a roughly uniform, finite value. This corresponds to bulk shear flow across the interface. As the perturbation size increases, circulation deposition is reduced where the surface normal is altered, but the sign of the vorticity remains unaltered. As the perturbation size is increased the amount of circulation deposited per unit wavelength decreases, as was previously noted in [26]. Compare this to the vorticity distribution used in Krasny, 1986 [38], in which KH was modeled using vortex sheet methods.

In Fig. 2.7b typical features of vorticity distribution leading to RM growth can be seen ($\theta = 0°$). When $\sin\theta \ll ka\cos\theta$, as in this case, the circulation over a single wavelength is zero, and there is vorticity of both signs deposited on either side of a sine wave. As the perturbation size increases, the amplitude of each vortex increases, but the overall circulation per wavelength remains zero. Compare this to vorticity distribution used in Sohn, 2004 [80], in which RM was modeled using vortex sheet methods.

In Fig. 2.7c, several vorticity distributions with a $30°$ tilt between the interface and incoming shock are shown. For the smallest amplitude perturbation (red line) the vorticity distribution is qualitatively similar to the that created in the KH geometry (Fig. 2.7a). The vorticity distribution has some finite mean value and only small fluctuations relative to the mean, this a consequence of the relative size of ka to the tilt as $\sin\theta \gg ka\cos\theta$. As the magnitude of a is increased, the magnitude of fluctuations in the vorticity distribution increase in kind. Inspecting Eq. 2.19, when $\sin\theta = ka\cos\theta$, the cross product $\hat{n} \times \hat{y}(\tau)$ (and therefore the vorticity distribution) will oscillate between zero and some finite value. In a qualitative sense, one "vortex blob" is deposited per wavelength and the vortices all co-rotate. A vorticity distribution with $\sin\theta \approx ka\cos\theta$ is shown in Fig. 2.7c (black line). In the limit that $\sin\theta \ll ka\cos\theta$ (not pictured) the amplitude of fluctuations in the vorticity distribution will be much greater than the mean, and the growth is expected to behave as RM.

2.4 Modeling periodic vortex-sheet evolution using a desingularized Birkhoff-Rott equation

The case where $\sin\theta \approx ka\cos\theta$ is a middle-regime between KH and RM. The early time growth in this regime is impulsive, as in RM. However, as was alluded to in Section 1.1.5, the late time behavior is that of late-time KH. The vorticity distribution can be used to predict this behavior using the Bikrkhoff-Rott equation, Eq. 2.5. In the introduction to this chapter, I gave a sketch of the derivation of the Birkhoff-Rott equation. The perturbation discussed in the previous section is periodic. Assuming that the shock crossing time is fast compared to the post-shock system evolution, the vorticity distribution along the post-shock interface will also be periodic. The amount

of deformation during the shock crossing is not directly important to periodicity, as each subsequent period of the perturbation will undergo the same deformation during shock crossing. However, there is typically a correlation between the amount of deformation and the speed of post-shock system evolution, so that a strongly deformed interface will often evolve on a time-scale comparable with the shock crossing time. This is a conundrum, as I am discussing the post-shock evolution of strongly deformed interfaces. The vortex sheet methods can not describe the shock-interface interaction, so as a practical matter, it is necessary to assume that the post-shock system does not evolve until after the shock has passed. The periodicity of the vorticity distribution can be incorporated in the differential equation governing the evolution of the system, so that only one wavelength of the system needs to be considered. I will first give the periodic solution for the flow surrounding a single point vortex per wavelength, and then give the periodic solution for a vortex sheet.

An infinite set of point vortices on a line, separated by the wavelength λ, is assumed. This set of points is described by the set of co-ordinate pairs $(n\lambda, 0)$ where n is an integer. The evolution of the flow in such a system is given by [32, 64]:

$$
\begin{aligned}
\frac{dx}{dt} &= \frac{\Gamma(\lambda)}{4\lambda} \frac{\sinh(\frac{2\pi y}{\lambda})}{\cos(\frac{\pi(x-.5\lambda)}{\lambda})^2 + \sinh(\frac{\pi y}{\lambda})^2} \\
\frac{dy}{dt} &= \frac{\Gamma(\lambda)}{4\lambda} \frac{\sin(\frac{2\pi(x-.5\lambda)}{\lambda})}{\cos(\frac{\pi(x-.5\lambda)}{\lambda})^2 + \sinh(\frac{\pi y}{\lambda})^2},
\end{aligned}
\tag{2.24}
$$

where $\Gamma(\lambda)$ is the circulation over one wavelength. To estimate the resulting evolution of interface structure, an initial spatial profile is assumed, and the envelope of the resulting particle trajectories are taken to give the mixing width. The flow in such a system is invariant with time: while any surface contour (or set of test points) placed in it will evolve in time, the vorticity distribution is stable.

A periodic, regularized, Birkhoff-Rott equation is given by [38]:

$$
\begin{aligned}
\frac{dx}{dt}(x,y,t) &= \frac{1}{4\lambda} \int ds \left[\frac{d\Gamma}{ds} \frac{\sinh(\frac{2\pi(y-y'(s,t))}{\lambda})}{\cos(\frac{\pi(x-x'(s,t)-.5\lambda)}{\lambda})^2 + \sinh(\frac{\pi(y-y'(s,t))}{\lambda})^2 + \delta^2} \right] \\
\frac{dy}{dt}(x,y,t) &= \frac{1}{4\lambda} \int ds \left[\frac{d\Gamma}{ds} \frac{\sin(\frac{2\pi(x-x'(s,t)-.5\lambda)}{\lambda})}{\cos(\frac{\pi(x-x'(s,t)-.5\lambda)}{\lambda})^2 + \sinh(\frac{\pi(y-y'(s,t))}{\lambda})^2 + \delta^2} \right],
\end{aligned}
\tag{2.25}
$$

where x and y have been written individually rather than as a vector, $(x'(s,t), y'(s,t))$ is some parameterization of the vortex sheet, $d\Gamma/ds$ is the vortex sheet strength, and δ is a regularization parameter which is used to avoid numerical instabilities introduced by rounding errors. The sheet strength,

$d\Gamma/ds$, is also a function of time. Depending on the update rule chosen for $d\Gamma/ds$ this calculation is referred to as either kinematic or dynamic. In the kinematic description, the circulation over one wavelength is conserved and the sheet strength is only updated according to local changes in arc length. More sophisticated approaches can take into account the secondary baroclinic vorticity deposition which occurs along the interface when there is a density contrast (e.g., the vortex sheet computations reported on in several manuscripts by Sohn [80, 82, 81]).

When numerically computing the evolution of a vortex sheet, it is discretized into the sum

$$\begin{aligned}
\frac{dx_i}{dt}(t) &= \frac{1}{4\lambda} \sum_{j \neq i} \left[\Gamma_j \frac{\sinh\left(\frac{2\pi(y_i - y_j)}{\lambda}\right)}{\cos\left(\frac{\pi(x_i - x_j - .5\lambda)}{\lambda}\right)^2 + \sinh\left(\frac{\pi(y_i - y_j)}{\lambda}\right)^2 + \delta^2} \right] \\
\frac{dy_i}{dt}(t) &= \frac{1}{4\lambda} \sum_{j \neq i} \left[\Gamma_j \frac{\sin\left(\frac{2\pi(x_i - x_j - .5\lambda)}{\lambda}\right)}{\cos\left(\frac{\pi(x_i - x_j - .5\lambda)}{\lambda}\right)^2 + \sinh\left(\frac{\pi(y_i - y_j)}{\lambda}\right)^2 + \delta^2} \right],
\end{aligned}$$
(2.26)

where Γ_i is the strength of the ith vortex, (x_i, y_i) is the position of the ith vortex, and δ is again a regularization parameter. At each time step, rounding errors accumulate in the vortex positions (x_i, y_i). These rounding errors lead to the KH instability unphysically arising at short length scales, the parameter δ suppresses the $1/r$ dependence of vortex interactions at short distances, reducing the susceptibility to numerical instabilities [38]. The number of points in the vortex sheet discretization, time step for system integration, maximum time for system evolution, and regularization parameter δ must all be chosen so that the discretization behaves reasonably.

2.4.1 Non-dimensionalization of periodic vortex sheet evolution

As was discussed in Section 1.3, non-dimensionalization of a dynamical system allows the comparison of system evolution across parameter spaces and physical regimes. I present only dimensionalized computations for vortex sheet evolution in this work, however, having the non-dimensionalization available will be useful for extensions of this work, as well as comparisons to non-dimensionalized computations elsewhere in the literature (e.g., [38]). To non-dimensionalize Eqs. 2.24, 2.25, and 2.26 the non-dimensional parameters

$$\begin{aligned}
x^* &= x/\lambda, \\
y^* &= y/\lambda, \text{ and} \\
t^* &= t\frac{\Gamma(\lambda)}{\lambda^2}
\end{aligned}$$
(2.27)

are used. In Eqs. 2.25 and 2.26, $\Gamma(\lambda)$ may be calculated as $\int_0^\lambda (d\Gamma/ds)ds$ and $\sum \Gamma_i$ respectively. The choice of non-dimensionalization for x and y is straightforward as the only dimensional length in the system is λ. The dimensional frequency used to non-dimensionalize time is a dimensional velocity divided by the characteristic length scale, λ. The velocity used is the average shear flow $(\Gamma(\lambda)/\lambda = \overline{\Delta v})$. As the vortex-sheet computation is being used to model vorticity distributions which will describe coupled KH and RM growth, a second dimensional velocity, the instability velocity of RM (v_{RM}) is also present. The velocity v_{RM} depends on the regularization parameter δ in addition to the shape and overall amplitude of the vorticity distribution, and is therefore a more complicated choice of dimensional velocity. As such, I use $\Gamma(\lambda)/\lambda = \overline{\Delta v}$ as the dimensional velocity here.

2.4.2 Impact of the regularization parameter δ

While the regularization parameter δ does not have a strict physical interpretation, insight into its impact can be gained by examining how it alters the flow surrounding a single periodic point vortex, i.e. considering how the addition of a regularization parameter alters Eq. 2.24. Even when considering vortex sheets, the system evolution is modeled by discretization into a finite number of point vortices, so that the distortion of the flow surrounding a single, repeating, point vortex by the regularization parameter δ will also yield insight into how the full vortex sheet calculation is modified. Eq. 2.24 with the regularization parameter included is given by

$$
\begin{aligned}
\frac{dx}{dt} &= \frac{\Gamma(\lambda)}{4\lambda} \frac{\sinh(\frac{2\pi y}{\lambda})}{\cos(\frac{\pi(x-.5\lambda)}{\lambda})^2 + \sinh(\frac{\pi y}{\lambda})^2 + \delta^2} \\
\frac{dy}{dt} &= \frac{\Gamma(\lambda)}{4\lambda} \frac{\sin(\frac{2\pi(x-.5\lambda)}{\lambda})}{\cos(\frac{\pi(x-.5\lambda)}{\lambda})^2 + \sinh(\frac{\pi y}{\lambda})^2 + \delta^2},
\end{aligned}
\tag{2.28}
$$

I will refer to this as the regularized discrete-vortex model (rDVM).

In the experimental work in Chapter 3 the initial interface perturbation is compressed by a factor of ~ 20, so that any initial post-shock perturbation on the interface can justifiably be ignored. The large compression applies to both the bulk interface tilt and any perturbation. Shocked heavy-to-light interfaces undergo phase inversion, meaning that the peaks of the initial perturbation become troughs and vice versa. This phase inversion comes in two varieties: direct (meaning that the phase inverts while the shock is crossing the interface) and indirect (meaning that the phase inverts after the shock has crossed the interface). The shock-interface interaction in Chapter 3 produces what I call "marginal direct phase inversion", so that the phase inverts during shock crossing but only by some small margin. The type of inversion is determined by the relative speeds of the incoming

shock (in the heavy material) and the post-shock interface. In this case, the post-shock interface and incoming shock differ in speed by only a few percent, so that they are nearly parallel. See Section 3.4 for more information.

Given the high compression, I assume that the interface at $t = 0$ is given by the locus of points $\{(x,y)|x \in \mathbb{R}, y = 0\}$. Given this assumption, the initial velocity profile of the interface can be found by evaluating Eq. 2.28 over the interface. Instability velocities are measurements of the rate of change of the amplitude of the interface structure, i.e. the "mixing amplitude" at any time is given by half the peak-to-valley of the interface contour. The instability velocity at $t = 0$ can therefore be determined by calculating the maximum y-velocity along the interface. At later times, when the interface has developed structure, the first time derivative of the amplitude time history must instead be taken.

The initial instability velocity is therefore given by

$$v_{\text{rDVM}}(t = 0) = \max \left(\frac{dy}{dt} \right)_{y=0}, \tag{2.29}$$

where dy/dt is taken from Eq. 2.28. The extrema can be identified by calculating the roots of

$$0 = \frac{\partial}{\partial x} \left(\frac{dy}{dt} \right)_{y=0}. \tag{2.30}$$

The roots are given by

$$x = \frac{\lambda}{2\pi} \cos^{-1} \left(\frac{-1}{2\delta^2 + 1} \right) - \frac{\lambda}{2}. \tag{2.31}$$

Plugging this into Eq. 2.28 yields

$$v_{\text{rDVM}}(t = 0) = \frac{\Gamma(\lambda)}{\lambda} \frac{1}{4|\delta|\sqrt{\delta^2 + 1}}. \tag{2.32}$$

Two general trends can be observed from this. First, when $\delta = 0$ the initial instability velocity is infinite, and the location with the maximum growth rate is at the initial vortex ($x = 0$). As δ is increased, the initial growth rate decreases and the location of maximum growth rate moves further from the point vortex. The interface envelope time history is plotted for several values of δ in Fig. 2.8. Streamlines for the rDVM with $\delta = 1$ are shown in Fig. 2.9.

While the initial instability velocity is altered by finite values of δ, the amount of shear across

the interface remains unaltered, as

$$\lim_{y \to \pm\infty} \frac{dx}{dt} = \frac{\Gamma}{4\lambda} \lim_{y \to \pm\infty} \frac{\sinh(\frac{2\pi y}{\lambda})}{\cos(\frac{\pi(x-.5\lambda)}{\lambda})^2 + \sinh(\frac{\pi y}{\lambda})^2 + \delta^2}$$

$$= \pm\frac{\Gamma}{2\lambda}. \tag{2.33}$$

This shows that the regularization parameter preserves shear without preserving the initial instability velocity. This also demonstrates that Γ/λ is the shear velocity as:

$$\Delta v = \lim_{y \to \infty} \frac{dx}{dt} - \lim_{y \to -\infty} \frac{dx}{dt}$$

$$= \frac{\Gamma}{\lambda}. \tag{2.34}$$

2.4.3   Vortex-sheet evolution

From the vorticity distribution calculated in Eq. 2.23, the interface evolution may be calculated from Eq. 2.26. The particular case of interest is the one where $\sin\theta \approx ka\cos\theta$. As was discussed earlier, this is the case when the mean tilt between the shock and interface is 30 degrees, the perturbation amplitude is 10 μm, and the perturbation wavelength is 100 μm. As above, the initial condition $\{(x,y)|x \in \mathbb{R}, y = 0\}$ at $t = 0$ is used. In addition to these physical parameters and initial conditions, the number of points for the discretization (N) and the regularization parameter (δ) must be chosen. In general, N should be chosen to be as large as is computationally achievable, and δ should be chosen in kind so that the vortex sheet computation is well behaved on whatever timescale is required.

In Fig. 2.10, the envelope amplitude history and the instability velocity are shown from $t = 0$ to $t = 5$ ns. In Fig. 2.11 the spatial structure of the vortex sheet is shown at 0.5 ns intervals from $t = 0.5$ ns to $t = 2.5$ ns. At early times, the interface has a nearly sinusoidal perturbation and the growth rate is RM-like, i.e. the amplitude grows linearly in time. As the perturbation grows the vorticity is transported along with it, leading to non-linear processes which reduce the instability velocity. The perturbation envelope eventually peaks at $\approx 0.28\lambda$, as is expected the late-time KH instability. The interface structure at late times develops the double branched spiral shape characteristic of late-time KH, e.g. compare to Krasny, 1986 [38]. In the next chapter, I will compare the results of this computation to experiment and simulation.

2.5 General considerations about vorticity distributions driven by shock-interface interactions

In Hurricane, 2008 [32] there is an implicit assumption that baroclinic vorticity deposition along a perturbed interface by a shock is uniquely associated with fluctuations between the interface and shock and distinct from the steady shear flow that results along the interface following shock passage. The discussion in Sections 2.3 and 2.4 indirectly argues that this is not the case, and shows that baroclinic vorticity deposition by shocks can result in uniform vorticity distributions. E.g., in Fig. 2.7 the amount of variation in the vorticity distribution is proportional to the size of perturbations on the pre-shock interface. Furthermore, in the KH and oblique cases significant amounts of baroclinic vorticity are deposited even without a perturbation [73, 72].

By considering the definition of circulation I will show that 1) the amount of circulation per wavelength, irrespective of any fluctuations in the vorticity distribution along the interface, determines the amount of shear across the interface, 2) baroclinic vorticity can be deposited by a shock such that the Kelvin-Helmholtz instability results, and 3) the initial instability velocity is independent of the shear flow across the interface, and is solely determined by variations in the vorticity distribution so long as there is no perturbation on the interface.

The purpose of these arguments is to show that determining the amount of circulation on an interface is insufficient to predict how perturbations on that interface will evolve, i.e. information about the distribution of vorticity on the interface is also required. These arguments together show that the method to predict interface evolution from baroclinic vorticity deposition on the interface proposed in Hurricane, 2008 [32] is incomplete.

2.5.1 The relation between circulation and shear flow across a vortex sheet

The circulation, Γ, is the vorticity flux through some surface of integration. From the definition of vorticity and Stokes' theorem we have

$$\Gamma = \iint_S \vec{\omega} \cdot d\vec{S} = \iint_S (\nabla \times \vec{u}) \cdot d\vec{S} = \oint_{\partial S} \vec{u} \cdot d\vec{\ell}, \tag{2.35}$$

where S is some surface of integration, $\vec{S}$ is the local surface normal of S, ∂S is the boundary of S, and $\vec{\ell}$ is everywhere parallel to ∂S. Assume that all vorticity in the system is localized to a flat line, referred to as a vortex sheet, which extends infinitely along the x-axis. Assume that the vorticity distribution is periodic with period λ along the vortex sheet, has 2D Cartesian symmetry, but that it is otherwise unknown. Consider a surface of integration which is a rectangle with two edges parallel to the vortex sheet, two edges orthogonal to the vortex sheet, and which the vortex sheet

47

passes through (pictured in Fig. 2.12).

Let the length of the rectangle along the interface be equal to an integer multiple of the wavelength, λ. As the system has period λ in the x direction, both the vorticity and velocity have the translational symmetry $\omega(x + n\lambda, y) = \omega(x, y)$ and $\vec{u}(x + n\lambda, y) = \vec{u}(x, y)$, where $n \in \mathbb{Z}$. This implies that when the contour integral $\oint_{\partial S} \vec{u} \cdot d\vec{\ell}$ is performed around boxes of length $n\lambda$, only the horizontal portions of the contour contribute, as the contribution of the vertical sections will cancel one another. The contributions from the horizontal sections then account for the entire integral. Above the interface the flow will have some average horizontal velocity $\overline{u_1}$, and the flow below the interface will have some average horizontal velocity $\overline{u_2}$. This yields the average shear across the interface, $\overline{\Delta v} = |\overline{u_2} - \overline{u_1}|$. The integral can then be evaluated, $\oint_{\partial S} \vec{u} \cdot d\vec{\ell} = \overline{\Delta v} \cdot n\lambda$. Denoting the circulation over one wavelength as $\Gamma(\lambda)$, one then has $n\Gamma(\lambda) = \overline{\Delta v} \cdot n\lambda \implies \Gamma(\lambda)/\lambda = \overline{\Delta v}$. This can be generalized to the situation where the vorticity has finite extent in the direction orthogonal to the sheet in a straightforward manner so long as the surface of integration is of larger extent than the vorticity in the y direction.

2.5.2   The shock driven Kelvin-Helmholtz instability

Consider the case of a shock traveling along an interface, with the shock front orthogonal to the mean interface structure. To zeroth order, and while the shock is sustained, the dominant pressure gradients in such a system are due to the shock, and the dominant density gradients are at the contact surface between heavy and light materials. Therefore, the vorticity at any point along the interface is largely determined by the relative direction of the shock and contact surface normal. For small interface perturbations, the pressure and density gradients remain nearly perfectly orthogonal along the interface, and an essentially uniform vortex sheet is deposited. In the case of an infinitesimally perturbed, tilted interface, a nearly uniform vortex sheet is also deposited on the interface by the shock. So long as the initial perturbation remains small, there are only small variations in the solution to the oblique shock. This results in the interface initially evolving as the linear KH instability, which has only small variations in both interface height and vorticity (KH is modeled in this way in Krasny, 1986 [38]). In these calculations there is no real distinction between the baroclinically deposited vorticity and the bulk shear flow across the interface. Rather, they are different ways of describing the same physical phenomena.

2.5.3   The separability of RM from KH for flat vortex sheets

In the limit that the vortex sheet is perfectly flat, it can be shown that the initial instability velocity is determined solely by fluctuations in the vorticity distribution, and does not depend on the mean

value of the vorticity distribution along the interface (i.e., it does not depend on the average shear across the interface). This argument does not depend on the periodicity of the vorticity distribution, so I use the non-periodic Birkhoff-Rott equation (Eq. 2.5) to proceed.

The y component of the non-periodic vortex-sheet velocity is given by

$$\hat{y} \cdot \vec{u}(\vec{x},t) = \frac{1}{2\pi} \int_{-\infty}^{\infty} ds \left[\frac{d\Gamma}{ds}(s,t)\hat{y} \cdot \left(\hat{z} \times \frac{\vec{x} - \vec{x}'(s,t)}{|\vec{x} - \vec{x}'(s,t)|^2} \right) \right]. \tag{2.36}$$

In the limit that the points are constrained to the locus $\{(x,y)|x \in \mathbb{R}, y = 0\}$, this becomes

$$\frac{dy}{dt}(x,t = 0) = \frac{1}{2\pi} \int_{-\infty}^{\infty} dx' \left[\frac{d\Gamma}{dx'} \frac{1}{x - x'|} \right]. \tag{2.37}$$

The vortex sheet strength can be separated into a mean component and a fluctuating component

$$\frac{d\Gamma}{dx'} = \overline{\Delta v} + \frac{d\widetilde{\Gamma}}{dx'}, \tag{2.38}$$

where $\overline{\Delta v}$ is the average circulation per unit length, and $\frac{d\widetilde{\Gamma}}{dx'}$ is the fluctuating component of the sheet strength. The integral for dy/dt can then be separated into two integrals over the fluctuating and non-fluctuating components of the sheet strength:

$$\begin{aligned} \frac{dy}{dt}(x,t = 0) &= \frac{1}{2\pi} \int_{-\infty}^{\infty} dx' \left[\left(\overline{\Delta v} + \frac{d\widetilde{\Gamma}}{dx'} \right) \frac{1}{x - x'} \right] \\ \frac{dy}{dt}(x,t = 0) &= \frac{1}{2\pi} \int_{-\infty}^{\infty} dx' \left[\overline{\Delta v} \frac{1}{x - x'} \right] + \frac{1}{2\pi} \int_{-\infty}^{\infty} dx' \left[\frac{d\widetilde{\Gamma}}{dx'} \frac{1}{x - x'} \right] \end{aligned} \tag{2.39}$$

The integral over the mean part of the sheet strength is zero. This follows from the oddness of the integrand about the point "x". As the bounds of integration are infinite, change of variables to $a = x - x'$ does not change the bounds, and the integral evaluates to zero. The initial instability velocity is therefore determined by the fluctuating component of the sheet strength alone,

$$\frac{dy}{dt}(x,t = 0) = \frac{1}{2\pi} \int_{-\infty}^{\infty} dx' \left[\frac{d\widetilde{\Gamma}}{dx'} \frac{1}{x - x'} \right]. \tag{2.40}$$

As the shear across the interface is equivalent to the average circulation per unit length along the interface, this shows that the initial instability velocity is independent of the shear flow so long as the structure on the interface is small. As the perturbation grows, the oddness argument breaks down, and shear will alter instability evolution.

2.6   Conclusion of the chapter

In summary, I have given an approximation for vorticity deposition by shocks on perturbed, oblique interfaces. I then used this approximation to estimate interface evolution using a periodic, regularized, Birkhoff-Rott equation in the case of a tilt between shock and interface of 30 degrees, and a sinusoidal perturbation with a 100 μm wavelength and 10 μm amplitude. In the next chapter, I will present experiments on Omega-EP which reproduce this interface tilt and perturbation as well as RAGE simulations of the same. I will compare the results of both experiment and simulation to the work in this chapter.
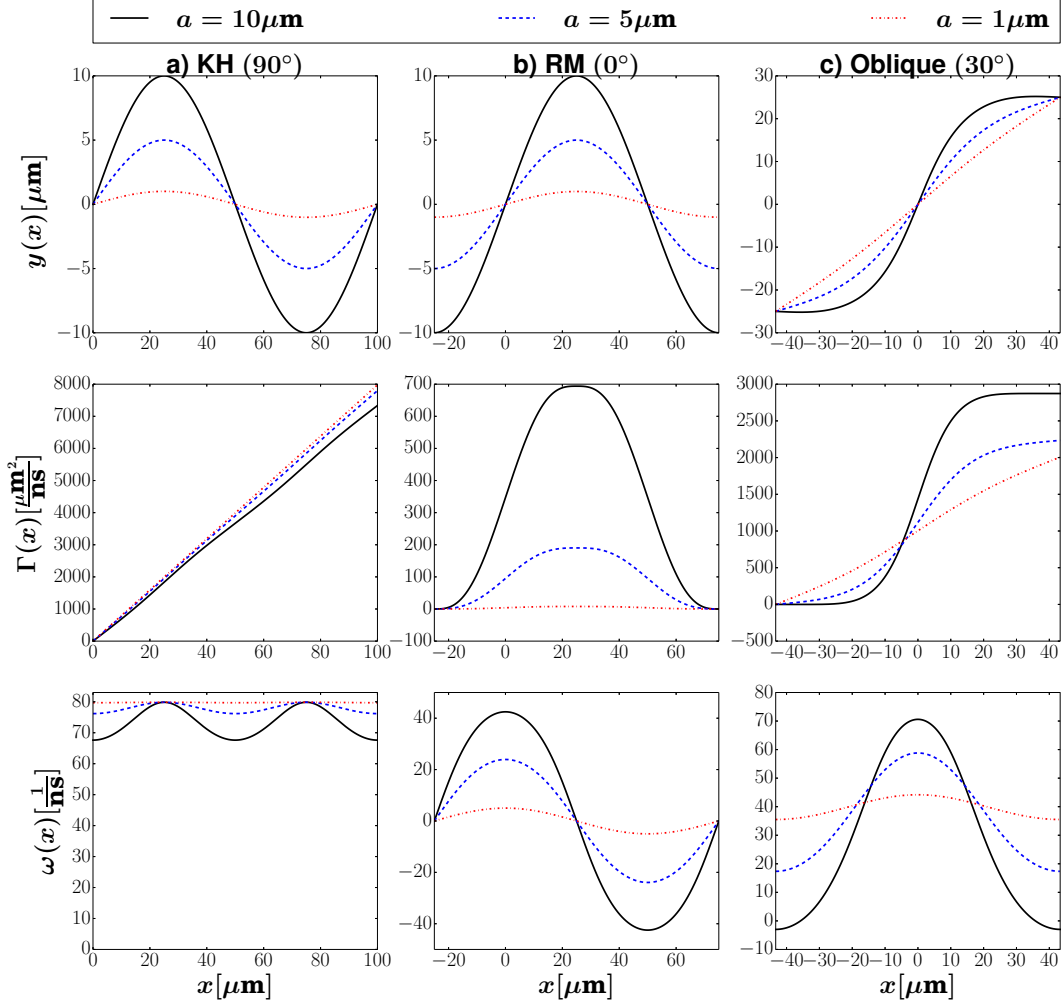
Figure 2.7 The height profile (top), circulation deposition (middle), and vorticity (bottom) are plotted over a single wavelength for each configuration shown in Fig. 1.2. The shock-interface orientations are the same as in Fig. 1.2, so that the shock propagates in the $\hat{x}$ direction in the KH case (left), and in the $\hat{y}$ direction in the other cases. For each tilt, a 10 μm (solid black), 5 μm (blue dashed), and 1 μm (red dash-dot) perturbation are shown. The perturbation wavelength is taken to be 100 μm in all cases. The physical parameters used to calculate the amplitudes of the circulations and vorticity distributions are given in Table 3.1. The plots of vorticity assume the delta function in Eq. 2.23 has units of μm^{-1}.
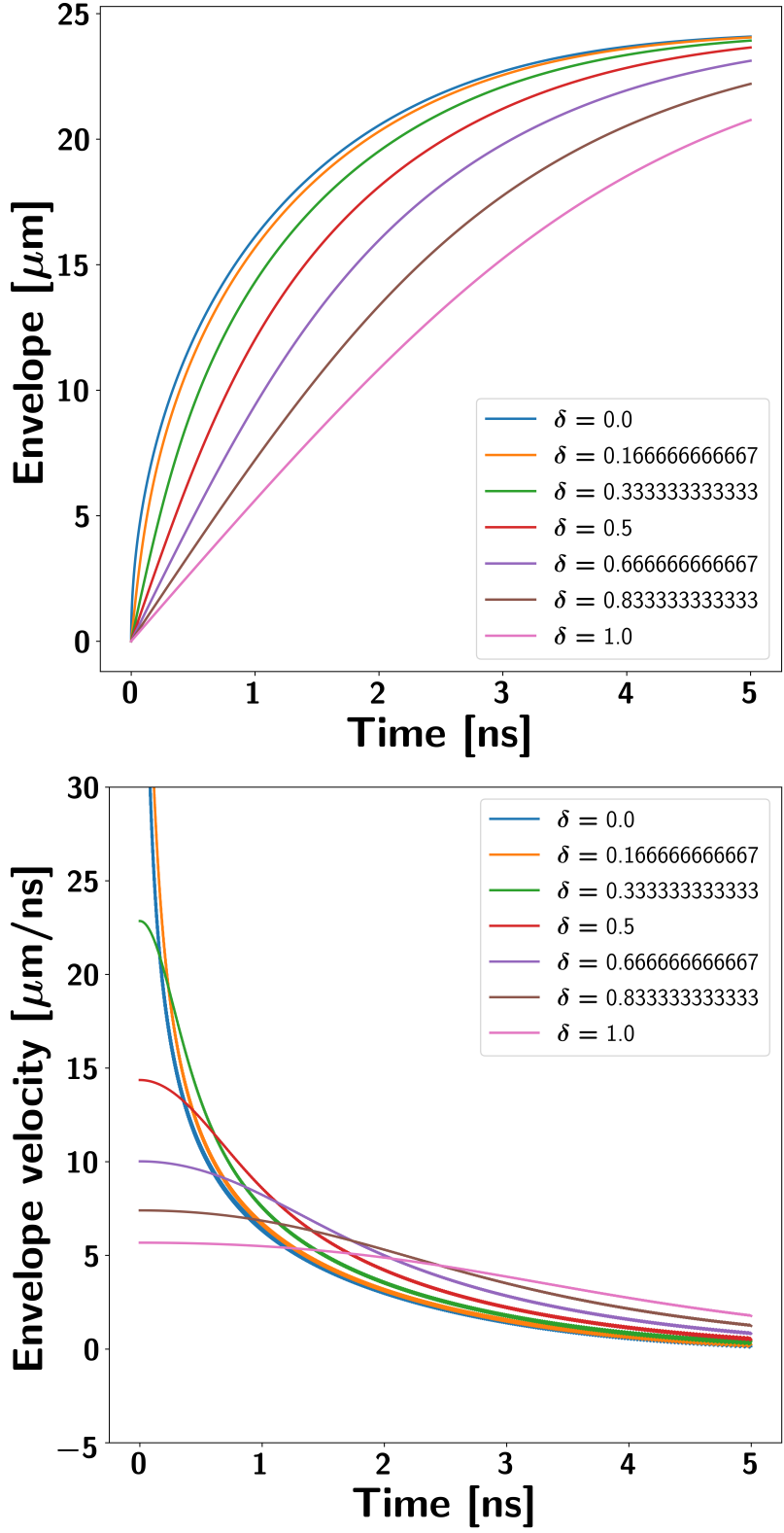
Figure 2.8 The interface envelope (top), and the envelope velocity (bottom) of rDVM flow with the initial condition $\{(x,y)|x \in \mathbb{R}, y = 0\}$ at $t = 0$ are plotted for several values of the regularization parameter δ, $0 \leq \delta \leq 1$. The physical parameters used to generate this plot are $\Gamma(\lambda) = 2871 \ \mu\text{m}^2 \ \text{ns}^{-1}$ and $\lambda = \cos(30°)100\mu\text{m}$, as in Table 3.1. Several values of the regularization parameter δ, with $0 \leq \delta \leq 1$, are plotted. The typical single-mode saturation amplitude for KH is $0.28\lambda \approx 24 \ \mu\text{m}$
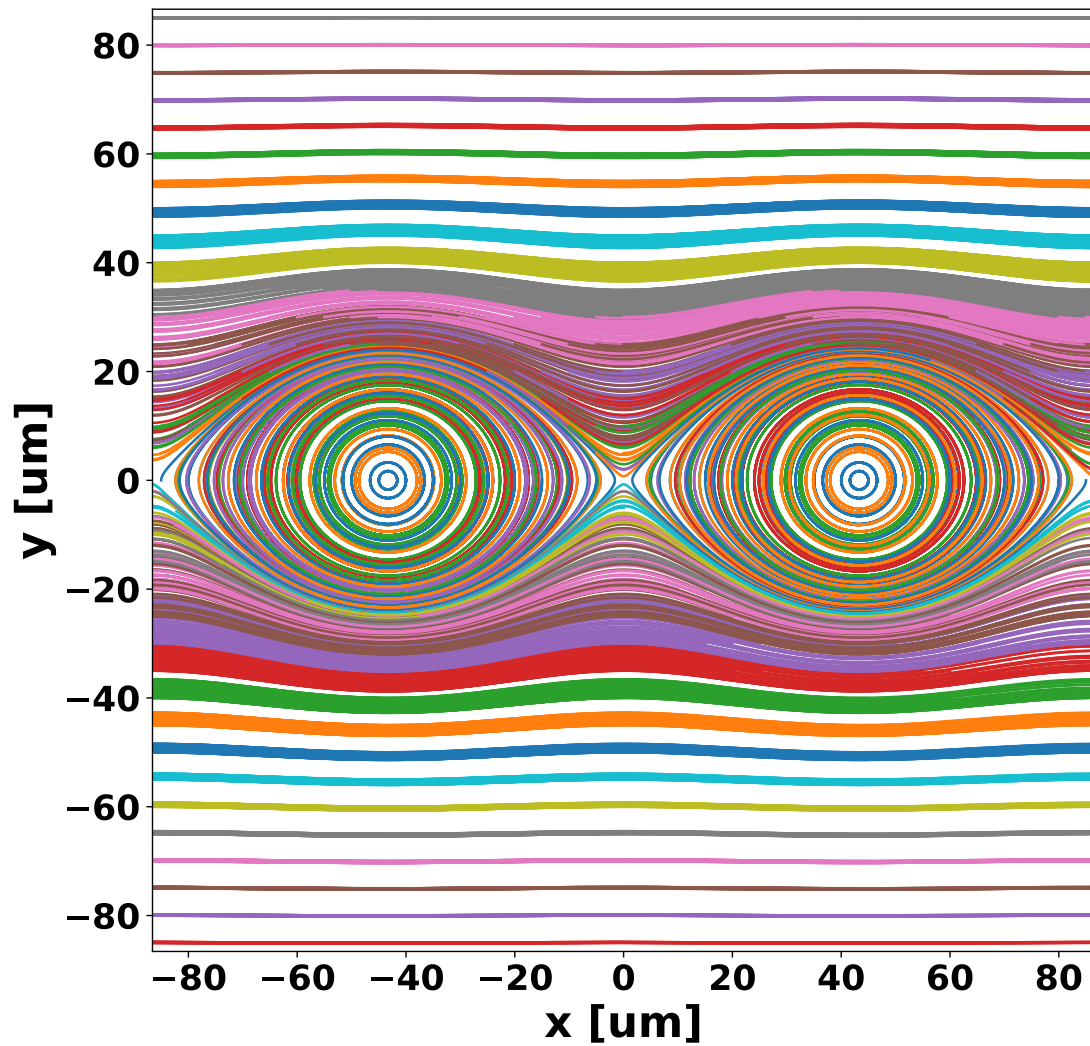
Figure 2.9 Streamlines from rDVM flow with $\delta = 1$ and $\lambda = \cos(30°)100\mu$m are plotted over two wavelengths. Notice that inside of each "vortex" the flow lines are closed, whereas outside the vortices the flow moves either to the left or to the right, and approximates uniform shear flow as one looks further from the interface. A stationary vorticity distribution is assumed, so that the streamlines are equivalent to streaklines.
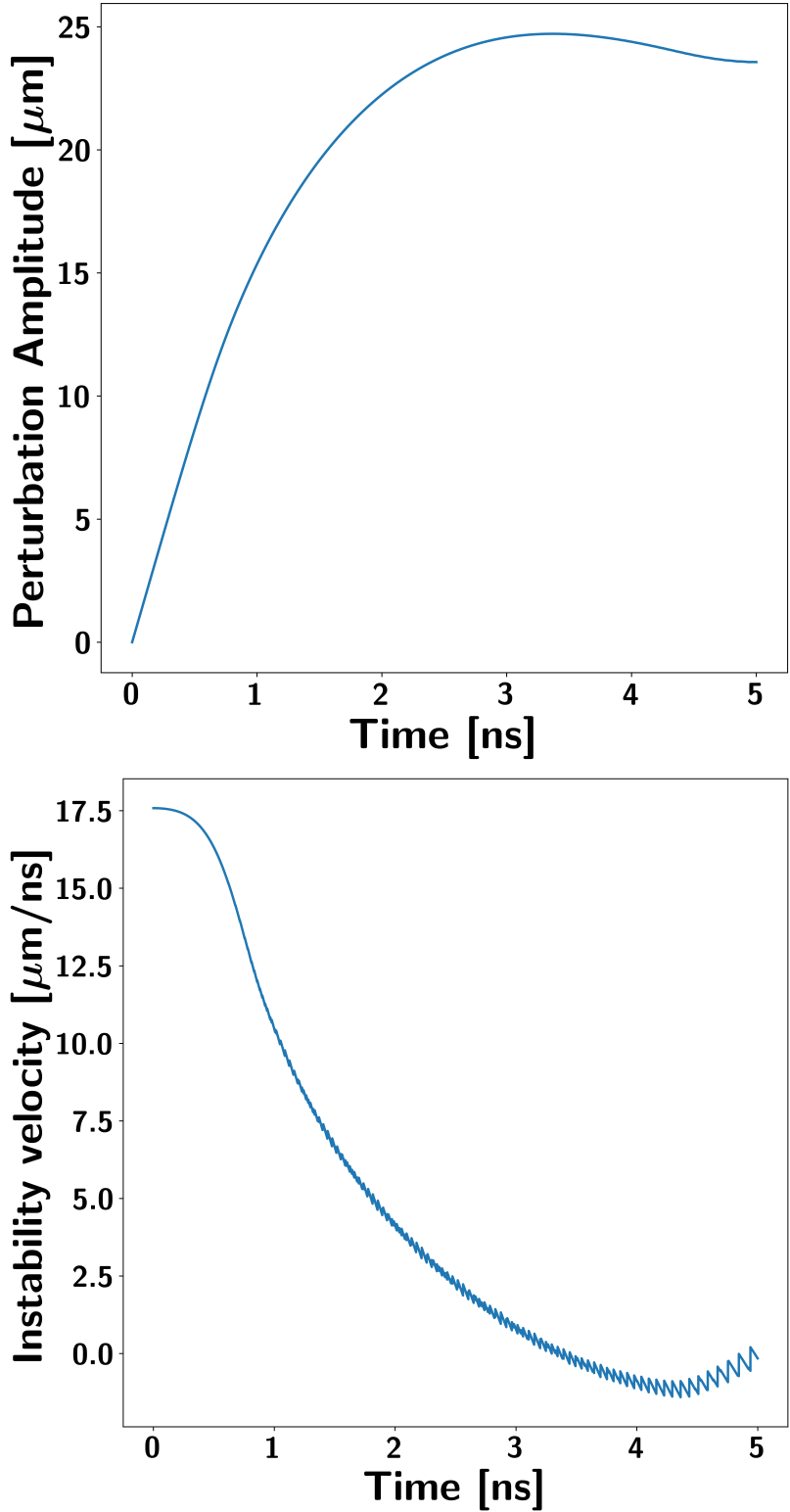
Figure 2.10 The envelope history (left) and instability velocity history (right) are plotted. The vorticity distribution is taken from Eq. 2.23 with $a = 10\,\mu$m, $\lambda = 100\,\mu$m, and $\theta = 30°$. Other physical parameters are taken from Table 3.1, so that the circulation per wavelength is $\Gamma(\lambda) = 2871\,\mu\text{m}^2\,\text{ns}^{-1}$. The initial condition $\{(x,y)|x \in \mathbb{R}, y = 0\}$ at $t = 0$ is used. The regularization parameter is $\delta = 0.1$.
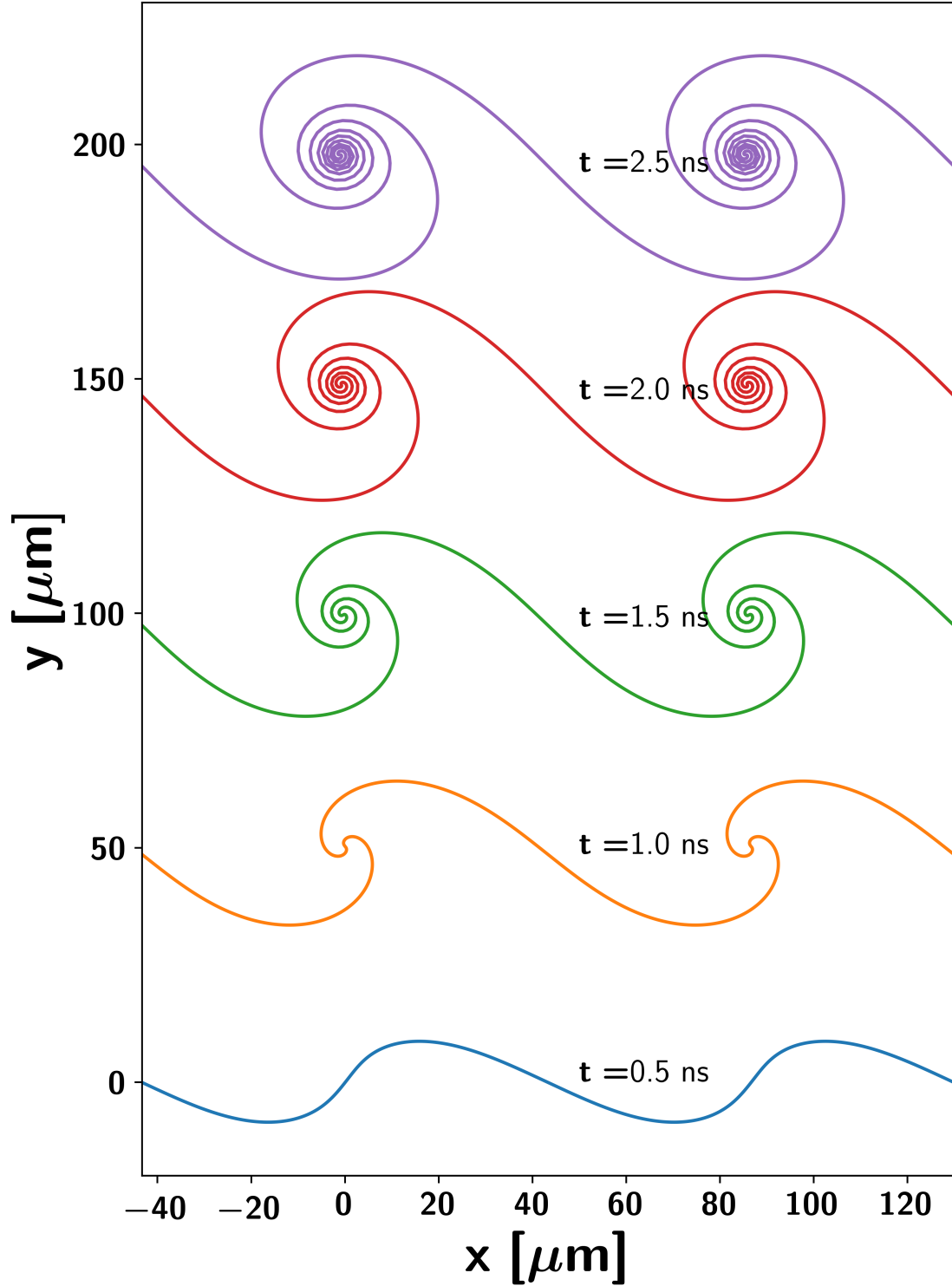
Figure 2.11 The vortex sheet contour is plotted at times between 0.5 ns and 2.5 ns at 0.5 ns intervals. The interface has been given an artificial velocity in the y direction so that the plotted contours do not overlap. The vorticity distribution is calculated with Eq. 2.23 with $a = 10$ μm, $\lambda = 100$ μm, and $\theta = 30°$. Other physical parameters are taken from Table 3.1, so that the circulation per wavelength is $\Gamma(\lambda) = 2871$ μm^2 ns^{-1}. The initial condition $\{(x,y)|x \in \mathbb{R}, y = 0\}$ at $t = 0$ is used. The regularization parameter is $\delta = 0.1$.

Figure 2.12 A diagram of the Stokes box integrated over in Eq. 2.35. The arrows on the edge of the box show the direction of $d\vec{\ell}$. The velocity in each half of the image has magnitude $\Delta u/2$, and is traveling to the right (left) on the top (bottom) of the interface. The flow is everywhere parallel to the interface.

Chapter 3

Omega-EP experiments to measure shock-driven mixing on oblique interfaces

Previous experimental work in the HED regime has taken place in configurations designed to produce KH ($\theta = 90°$) or RM ($\theta = 0°$). Here, I present novel experimental work with $\sin\theta \approx ka\cos\theta$, a regime which was discussed in the previous chapter. This work builds on a great deal of experimental and design work previously done by Carlos Di Stefano, Willow Wan, and Guy Malamud pioneering the study of both RM and KH using the sustained pulses available on Omega-EP [90, 91, 83, 14, 51, 52]. Omega-EP has four Nd:YLF laser beams, each with about 4 kJ of energy available with a pulse length of 10 ns when converted to 3ω (i.e. a wavelength of 351 nm) [92]. Three of these beams are typically used to create a shock for a given experiment, and the remaining beam is used to create an x-ray source, which is used in conjunction with an x-ray diagnostic to image the evolution of the interface perturbation.

In this chapter, experiments in which a supported shock interacts obliquely with an interface in the heavy-to-light geometry are presented. The shock has a 30 degree tilt relative to the mean interface, and the interface has a machined sinusoidal perturbation with an amplitude of 10 μm and a wavelength of 100 μm (the case which was discussed in detail in Section 2.4). At the end of the laser pulses sustaining the shock, a rarefaction is launched into the experimental system. Once this rarefaction reaches the interface it will cause both decompression and the Rayleigh-Taylor instability, processes which will increase the spike and bubble heights. This leads to two phases of growth: one in which the shock is sustained so that the interface structure evolves as a consequence of the shock-interface interaction alone, and a second phase in which the additional rarefaction alters instability growth.

In order to differentiate what mechanisms are important for interface structure evolution at different times, I compare experimentally measured perturbation heights to several computations. I compare experimental results to:

1. Vortex sheet computations, as were described in Section 2.4.

2. Two dimensional RAGE simulations, which utilize a mass-inlet condition to create the shock. The mass-inlet condition does not model the laser turn-off rarefaction.

3. One dimensional HYADES simulations, which do model the laser (including the laser turn-off rarefaction). The parameters needed to calculate the decompression and RT growth of the interface structure are extracted from HYADES, and used to estimate the additional growth due to the rarefaction (see Eq. 3.2) as compared to RAGE simulations.

4. Linear growth rates for RM and KH.

Comparisons between (1), (2), and the experiment are used to assess the validity of the vortex sheet model, while (3) is used to determine over what range of times decompression and RT can be neglected (see Fig. 3.5). (1) and (4) will be compared to discuss the relative merits of using the linear instability picture vs using the vorticity picture of interface structure evolution. Finally, I will discuss some inconsistencies between the vortex sheet computations and RAGE simulations and how they might be resolved in future work.

3.1   Experimental platform description

The experimental system is composed of two stacked layers of material, see Fig. 3.1. A 510 μm thick layer of polyamide-imide (PAI, $C_{22}H_{14}O_4N_2$) with density 1.45 g cm^{-3}, followed by a 990 μm thick layer of 0.1 g cm^{-3} CH foam. A density matched, iodinated CHI ($C_{50}H_{47}I_3$) 100 μm long, 100 μm deep strip is inserted into a trench cut into the PAI along the interface with the foam to provide contrast in x-ray transmission radiographs. These materials are all inside a 900 μm inner diameter, 1300 μm outer diameter CH shock tube. A similar platform was used in Di Stefano, 2017 to study broadband RM mode coupling [15]. In the oblique case, the height of the PAI layer varies as a function of x. Instability growth occurs at the boundary between the PAI/CHI and foam. The initial condition is set by machining a single mode, sinusoidal, perturbation into the face of the PAI and CHI adjacent to the CH foam. The perturbation is given by

$$\eta(\chi) = 10\mu m \sin\left(\frac{2\pi\chi}{100\mu m}\right), \tag{3.1}$$

where $\hat{\chi}$ is taken to be in the plane of the mean interface and perpendicular to the diagnostic imaging axis, and $\hat{\eta}$ is taken to be normal to the mean interface, see Fig. 1.2c. The mean tilt is $\theta = 30°$ so that $\hat{x} \cdot \hat{\chi} = \cos(30°)$.

Three, 351 nm, Omega-EP laser beams irradiate the bottom of the PAI layer, creating a strong shock. The beams have a 10 ns square pulse temporal profile, ~ 14 kJ total energy, and are fired

simultaneously. Each beam is smoothed with distributed phase plates, and has a super-gaussian profile of the form $\exp[-(r/550\mu m)^8]$, with an irradiance of 1.4×10^{14} W cm^{-2}, where r is the distance from the beam axis. The resulting shock speed is measured to be 38 μm ns^{-1} in experiments.

A fourth, 1053 nm, 20 ps pulse duration, ~ 1 kJ, short-pulse beam is used to produce Cu Kα
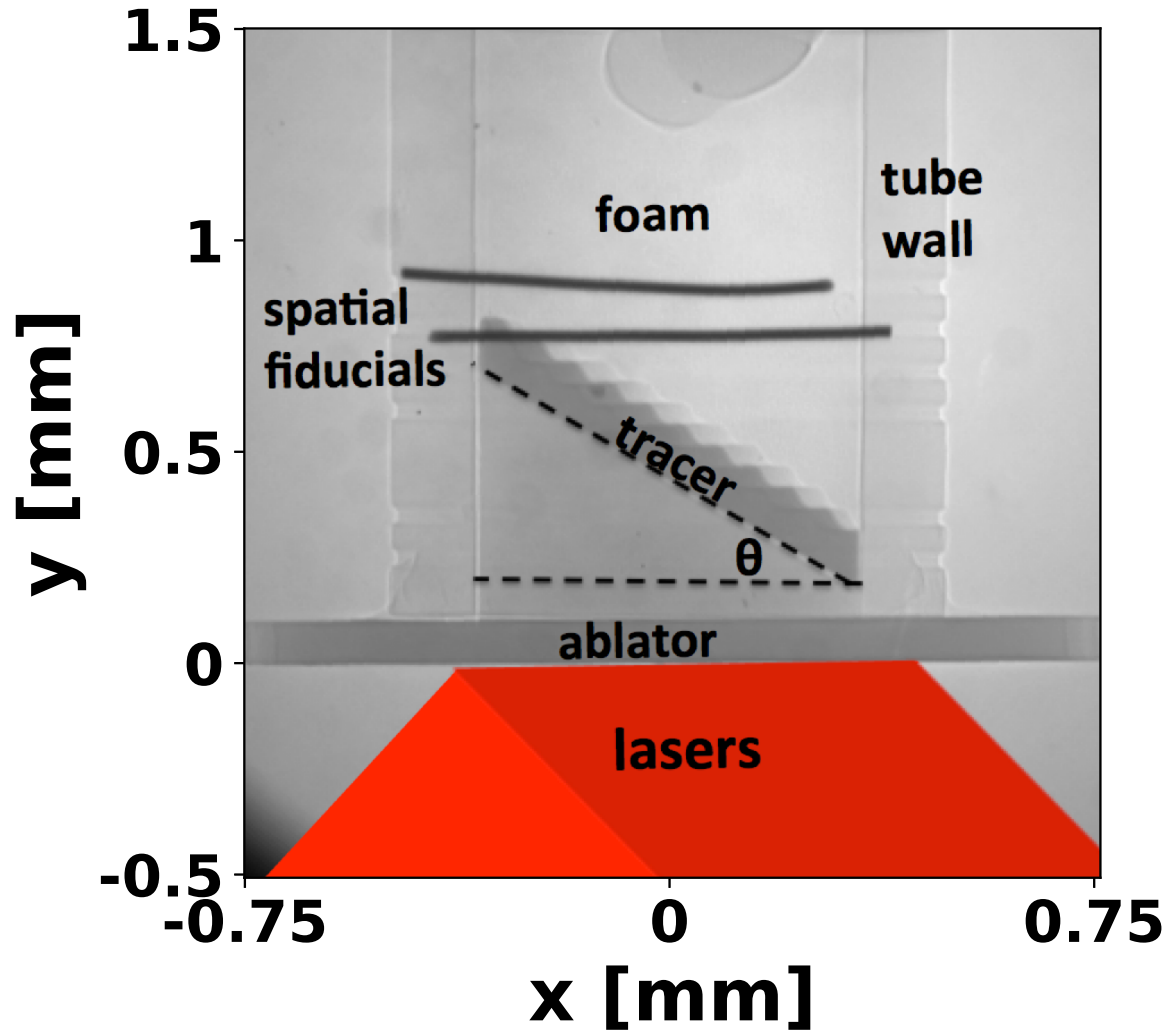
Figure 3.1 A pre-shot radiograph of a target, taken from the diagnostic field of view. The experiment takes place inside a 200 μm thick, 1.5 mm long, 900 μm inner diameter CH shock tube. The ablator is made of PAI ($\rho = 1.45$ g cm^{-3}), and varies in thickness between 150 and 670 μm. The lasers irradiate the bottom of the PAI, and are incident from the bottom of the image. A 100 μm thick, density matched, CHI tracer layer is inserted into the center of the last 100 μm of the ablator to provide contrast for x-ray transmission radiographs. The remainder of the shock tube is filled with 0.1 g cm^{-3} CH foam. The angle of the ablator-foam interface is varied with respect to the shock tube axis in order to vary the relative importance of KH to RM and RT. The stalk tip and associated glue glob are visible at the top of the radiograph. Some ghosting is apparent at the interface due to rotational misalignment of the target relative to the pre-shot radiography axis, this alignment system is independent of that used at Omega-EP, and does not reflect the as-shot alignment accuracy.
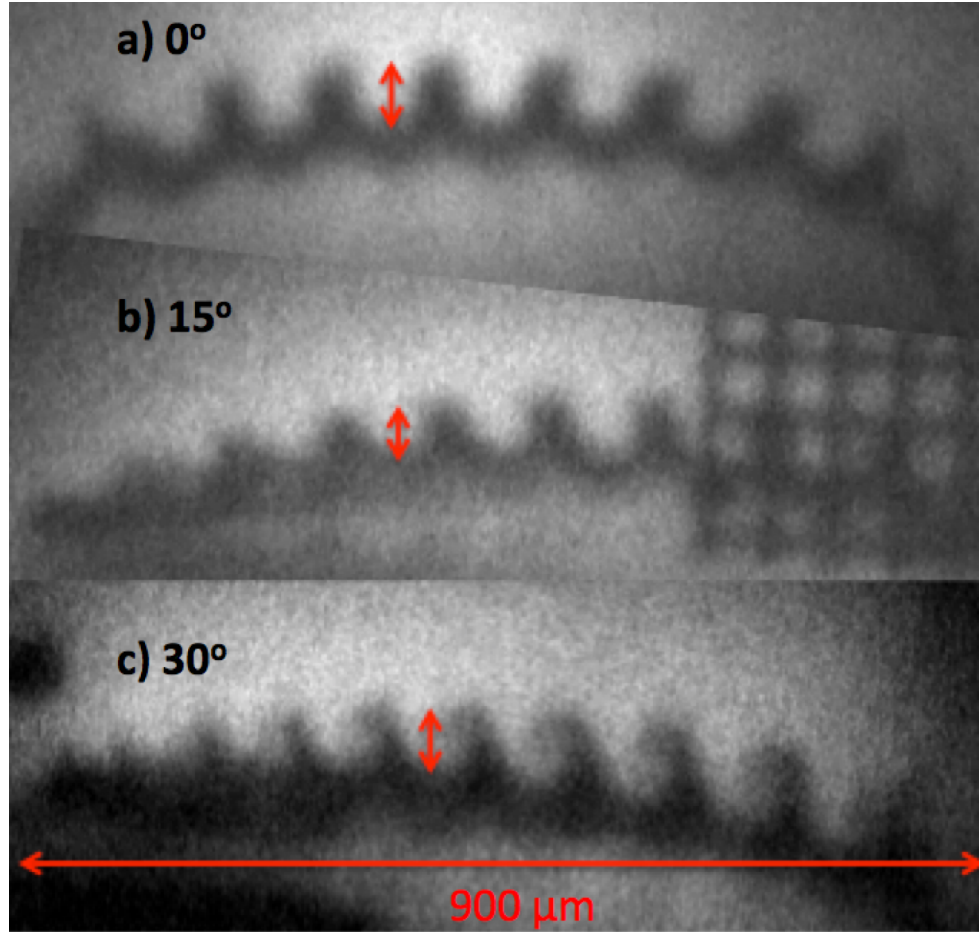
Figure 3.2 Examples of experimental radiographs taken with the SCI sometime after shock breakout of the tracer layer. The shock is incident from the bottom of the images, and travels vertically. The top image (a) shows an experiment with no tilt between the shock and interface. The middle image (b) shows interface evolution with a 15° tilt. The bottom image (c) shows an experiment with a 30° tilt between the shock and interface. Both interfaces had a single mode, machined, perturbation as described in Eq. 3.1. The arrows at each interface roughly indicate the perturbation peak-to-valley. Images (a), (b), and (c) were taken at 21, 19, and 21 ns after the onset of the shock drive, respectively. For image (a), this is 7 ns after shock breakout, for image (b) the timing relative to shock breakout varies from 2→6 ns left-to-right up to the grid, whereas for image (c) the timing relative to shock breakout varies from $1 \rightarrow 11$ ns left to right. The grid in (b) is a fiducial feature, used to confirm diagnostic resolution and magnification. The grid is located outside of the shock tube and does not alter the hydrodynamics of the interface.

photons through the irradiation of a thin Cu foil. The Cu Kα photons are focused by a crystal onto an image plate to produce an experimental x-ray radiograph with a magnification of ≈ 10, and a resolution of ≈ 10 μm [84].

Radiographs showing the typical results of experiments with 0°, 15°, and 30° tilts are shown

Table 3.1 Bulk flow parameters are reported. The shock speed in the heavy material is estimated experimentally from the shock breakout time along the interface. All other quantities are determined from 2D RAGE simulations which have been tuned to the measured parameter. γ_{eff} is calculated from the compression across the primary and transmitted shocks, respectively, u_{s} is the shock speed in each material, P_{s} is the post-shock pressure in each pressure, and u_{y} is the post-shock fluid speed in the direction of shock propagation in the lab frame. The post-rarefaction pressure in the heavy material will be equal to the post-shock pressure in the foam.

	γ_{eff}	u_{s}	P_{s}	u_y
plastic	1.90	$38\frac{\mu\text{m}}{\text{ns}}$	13.5 Mbar	$25.1\frac{\mu\text{m}}{\text{ns}}$
foam	1.57	$52\frac{\mu\text{m}}{\text{ns}}$	2.1 Mbar	$39.9\frac{\mu\text{m}}{\text{ns}}$

in Fig. 3.2. For the untilted targets, the shock arrives at the interface at 13.5 ns after the onset of laser irradiation. For the oblique targets, shock arrival time varies along the interface. In all images, the shock travels from bottom to top. The bottom-most light area corresponds to the undoped PAI. The dark region above this corresponds to the doped layer of CHI. Above this, the light region is the CH foam. The shock front is curved as a result of the laser intensity profile, as well as a rarefaction resulting from the shock interacting with the shock tube wall. As one would expect from the discussion in Chapter 2, the spike and bubble morphologies noticeably change as a function of tilt, with the 0° case showing no rolling-over, and the 30° case displaying well formed KH rollups. Perturbation amplitude in the 30° case is plotted in Figs. 3.5 and 3.6. Time for each vortex is offset by the time of shock arrival for the corresponding part of the pre-shock interface in the plots.

3.2   RAGE Simulations

To simulate hydrodynamic instability growth on the interface, two-dimensional Radiation Adaptive Grid Eulerian (RAGE) simulations [22] were performed. At the time this work was done, RAGE lacked a working laser package in 2D, so a mass-inlet condition was used to drive hydrodynamics. A mass-inlet condition sources material at the post-shock conditions of the ablator (reported in Table 3.1) on a boundary of the simulation, here set to be a thin layer adjacent to the initial placement of the ablator. The simulations use SESAME polystyrene equations of state for all materials [48], initialized at their respective solid densities, and pressure balanced to avoid unphysical pre-shock diffusion at the interface. The initial pressure has been set at 60 kbar, which is two orders of magnitude weaker than the incoming shock pressure. The perturbed interface is resolved to 1 μm, while the rest of the medium is resolved to 2 μm.

Some bulk experimental observable must be used to calibrate the mass-inlet condition. The easiest to measure observables are the combination of shock speed in the ablator and the post-shock interface speed, see Table 3.1. In particular, the shock speed is easily measured on oblique targets,

Table 3.2 Parameters describing the properties of the interface. The pre (post) shock Atwood number is given by A_{pre} (A_{post}). The experimental post-shock interface velocity, $u_{\text{i}}(\exp)$, is estimated experimentally from the mean interface location in radiographs of the post-shock interface. The simulated post-shock interface velocity is given by u_{i}. The circulation over one wavelength predicted by Eq. 2.21 for $a = 10$ μm, $\lambda = 100$ μm, and $\theta = 30°$ is given by $\Gamma_{\text{model}}(\lambda)$. The mean shear flow, $\overline{\Delta v}$ is reported from RAGE simulations with no perturbation (with a perturbation, the localization of the vorticity makes it harder to determine $\overline{\Delta v}$ from the fluid velocity directly). This corresponds to a circulation over one wavelength of $\Gamma(\lambda) = \overline{\Delta v}\lambda \approx 1400\frac{\mu\text{m}^2}{\text{ns}}$. The circulation per wavelength from RAGE simulations with a perturbation, $\Gamma_{\text{RAGE}}(\lambda)$, is extracted by integrating the vorticity output over a box of width 87 μm and of height large enough to contain the interface. There is some ambiguity in this number due to vorticity deposited in the shocked foam region due to curvature in the transmitted shock (imprinted from the universe), this leads to $\pm 200\frac{\mu\text{m}^2}{\text{ns}}$ variation in the measured circulation depending on the region of integration chosen, and time after shock-breakout chosen to perform the integration. The large discrepancy between $\Gamma_{\text{model}}(\lambda)$ and $\Gamma_{\text{RAGE}}(\lambda)$ is discussed in Appendix A.

	A_{pre}	A_{post}	u_{i}	$u_{\text{i}}(\exp)$	$\overline{\Delta v}$	$\Gamma_{\text{model}}(\lambda)$	$\Gamma_{\text{RAGE}}(\lambda)$
interface	0.87	0.67	$39.5\frac{\mu\text{m}}{\text{ns}}$	$40\frac{\mu\text{m}}{\text{ns}}$	$16\frac{\mu m}{ns}$	$2871\frac{\mu\text{m}^2}{\text{ns}}$	$1400\frac{\mu\text{m}^2}{\text{ns}}$

as the shock takes several nanoseconds to traverse the interface, and the interaction point is readily seen. See Fig. 3.4 for a streaked density plot from 1D RAGE simulations, with the post-shock interface trajectory over-plotted as white circles [15]. The data here are from non-oblique shots in the RM geometry ($\theta = 0°$). About 18 ns after the laser pulses are incident on the ablator, the rarefaction from laser turn-off reaches the interface and decelerates it. In practice, we optimize for getting the shock breakout time right in simulations, and the subsequent interface trajectory has some mismatch due to a combination of 1) getting the laser turn-off rarefaction wrong, 2) getting the ablator EOS wrong, and 3) getting the foam EOS wrong. In principle, the mass-inlet condition could be varied in the 2D simulation until shock and interface trajectories are found which match the experiment, however, in practice its more time efficient to do the coarse tuning with a 1D code, and then only tune the 2D code as EOS differences demand (the 1D RAGE and 2D RAGE simulations were done with the same EOS, so this is not an issue). A similar procedure has been used in previous simulations of HED hydrodynamic instability experiments on Omega-EP [51, 52, 15, 83, 14, 90, 91]. We performed 2D RAGE simulations both with, as in the experiment, and without a perturbation on the interface. The simulations with a perturbation are compared to data in Fig. 3.5, and the simulations with no perturbation are used to extract bulk hydrodynamic properties, which are used to estimate linear KH and RM growth, see Table 3.1. Interface contours extracted from RAGE simulations via an unsharp-mask are shown in Fig. 3.3.
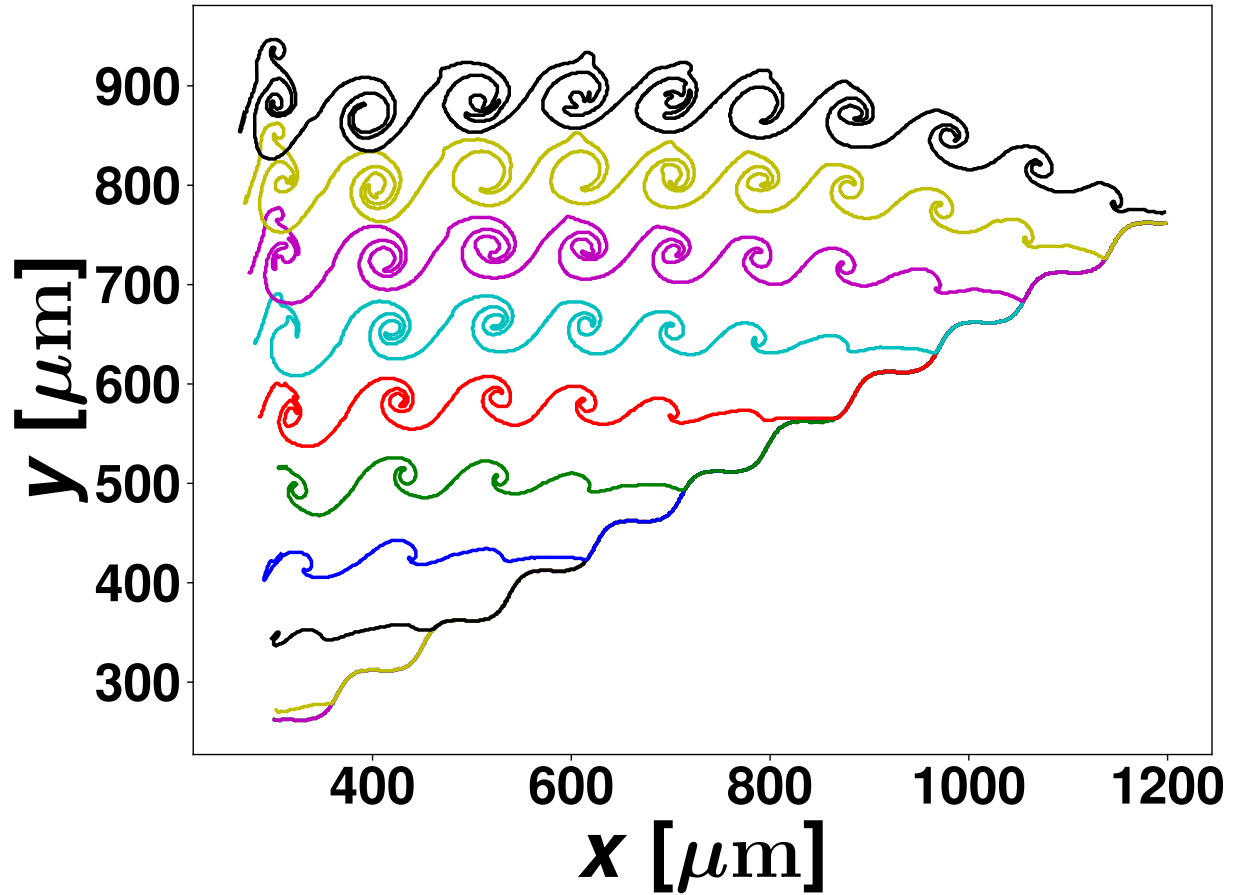
Figure 3.3 Contours of interface evolution from RAGE simulations are shown. The contours are at 2 ns intervals, and the last time plotted is 24 ns (topmost black line). The shock is incident from the bottom of the plot and the mean tilt is 30°. The perturbation is a sinusoid with a 10 μm amplitude and 100 μm wavelength, as was described in Eq. 3.1.

3.3 Decompression and deceleration

At the end of the laser pulse a rarefaction is launched into the ablator. This phenomenon cannot be replicated with the mass inlet drive. The rarefaction decompresses and decelerates the interface. The decompression results in stretching, and the deceleration causes Rayleigh-Taylor (RT) instability

growth [85, 87]. Both of these processes result in additional growth of the interface structure amplitude. The bulk interface properties from HYADES simulations were extracted, and used in a model (Eq. 3.2) which added RT growth and stretching to the interface perturbation growth from 2D RAGE simulations. HYADES is a Lagrangian radiation hydrodynamics code which includes a laser package [44]. In particular, the velocity and density on either side of the interface is required for the model. In addition to qualitatively capturing the impact of the rarefaction on interface evolution at late times, this work provides an estimate of the range of times over which the mass-inlet approximation is valid. Rayleigh-Taylor and decompression are found to be of negligible importance to interface perturbation evolution before $t \approx 5$ ns after shock breakout, confirming that the mass-inlet condition is a valid way to model the experiment before this time.

To model the effect of deceleration and decompression on the interface perturbation the following
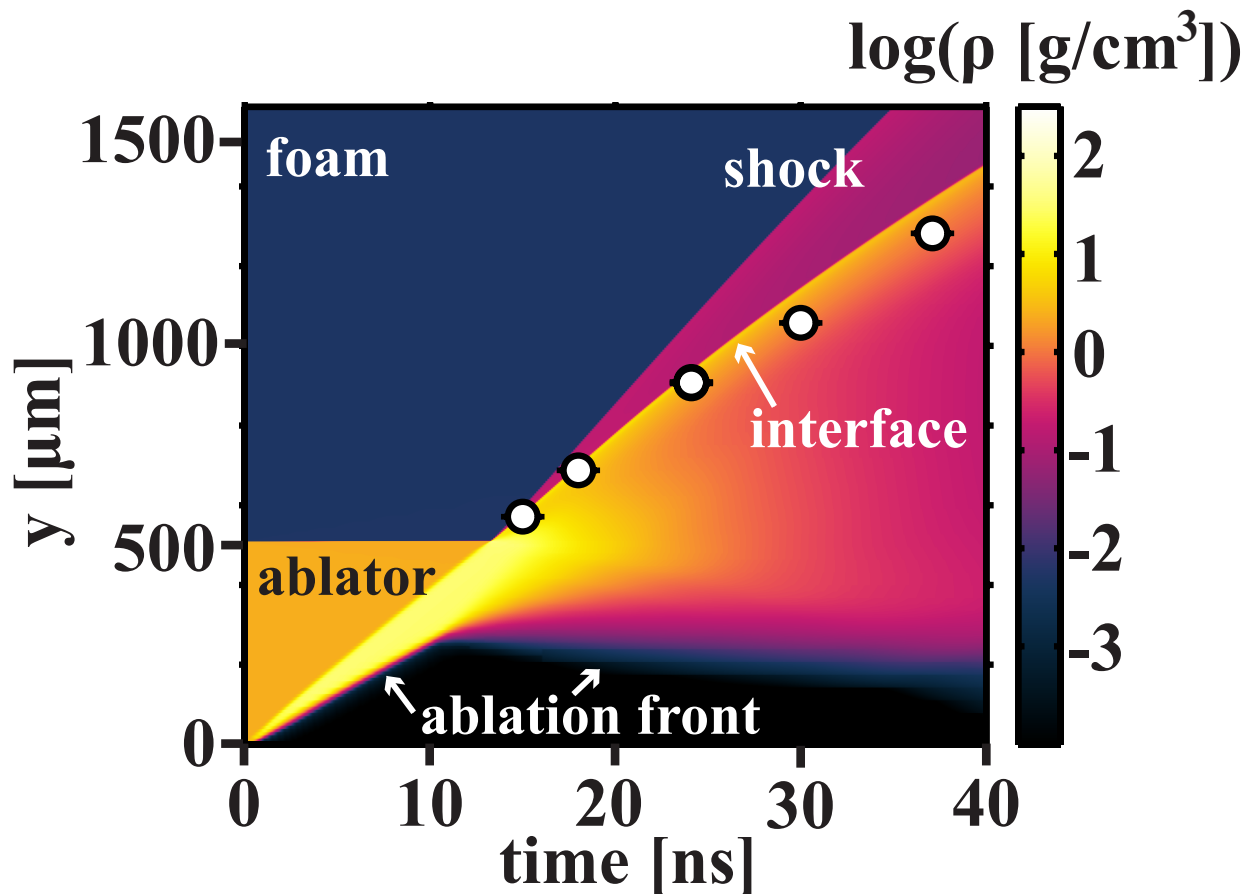
Figure 3.4 This is Fig. 4 from Di Stefano et al., 2017 [15]. The Di Stefano paper and this chapter use a common experimental platform, i.e. the ablator, foam, tracer, and laser drive are all the same, other than the tilt and perturbation of the ablator-foam interface. The contour plot shows the mass density from 1D RAGE simulations, including a laser package. The post-shock fluid conditions and wave timings (i.e. shock and rarefaction) are substantially similar between 1D RAGE and 1D HYADES simulations.

equation is integrated:

$$\frac{d\eta}{dt} = v_{\text{RAGE}}(t) + \omega(t)\eta(t) + v_{\text{b}}(t) + v_{\text{s}}(t), \tag{3.2}$$

where $v_{\text{b/s}}(t)$ are the late time RT bubble and spike velocities from Goncharov [24], given by

$$v_{\text{b/s}}(t) = \sqrt{\frac{2A(t)}{1 \pm A(t)} \frac{g(t)}{3k}}, \tag{3.3}$$

v_{RAGE} refers to the instability velocity from RAGE simulations (i.e., the first time derivative of the perturbation amplitude history taken from RAGE simulations), $A(t)$, $g(t)$, and $\omega(t) = \left[\frac{\partial u}{\partial x}\right]_{x=x_{\text{int}}(t)}$ are taken from HYADES simulations. The RT bubble and spike velocities are the asymptotic, late time velocities, and as such should be expected to be overestimates of the growth rate early in time. Late in time, once KH roll-up structures have formed, it is unclear what validity the late-time RT solutions will have. Future computational work will utilize RAGE's new laser package to study coupled RT and KH growth on oblique interfaces.

Fig. 3.5 shows the instability growth from this model, compared to simulation and experimental results. The model is initialized at $t = 2.25$ ns in order to avoid the shock crossing the interface. Regularized vortex-sheet evolution, as described in Eq. 2.26, is also plotted. To predict the interface evolution from Eq. 2.26, the vorticity distribution is calculated from Eq. 2.23 assuming a 30° tilt, 10 μm initial perturbation height, and 100 μm initial wavelength. Other parameters are taken from Table 3.1, giving a circulation over one wavelength of $\Gamma(\lambda) = 2871\frac{\mu\text{m}^2}{\text{ns}}$. The wavelength after direct phase inversion, $\lambda_{\text{eff}} \approx \lambda \cos\theta$, is used in Eq. 2.26. An initially flat spatial profile is assumed for the perturbation, and the resulting particle trajectories are numerically integrated. The perturbation envelope of the vortex sheet computation is labeled as VS in Figs. 3.5 and 3.6. The perturbation envelope from a second vortex sheet computation is also shown. For this computation, the vorticity distribution shape is kept the same as above, but the vorticity distribution is normalized so that $\Gamma(\lambda) = 1400\frac{\mu\text{m}^2}{\text{ns}}$ in order to match RAGE simulations. The normalized vortex sheet computation matches simulation and experiment better than the un-normalized computation. The large discrepancy in $\Gamma(\lambda)$ between simulation and the calculation in Chapter 2 is discussed in Appendix A.

Experiment, simulation, and the regularized vortex sheet model with $\Gamma(\lambda)$ normalized to RAGE simulations match well until $t \approx 5$ ns. After this time, all three diverge. The vortex sheet model incorporates no physical effects other than the initial vorticity deposition, so it is expected to diverge from both experiment and simulations once secondary baroclinic vorticity deposition or other waves in the system become relevant. The RAGE simulation has a sustained pressure source, so that it does not include the laser turn-off rarefaction. The results from RAGE are therefore

65
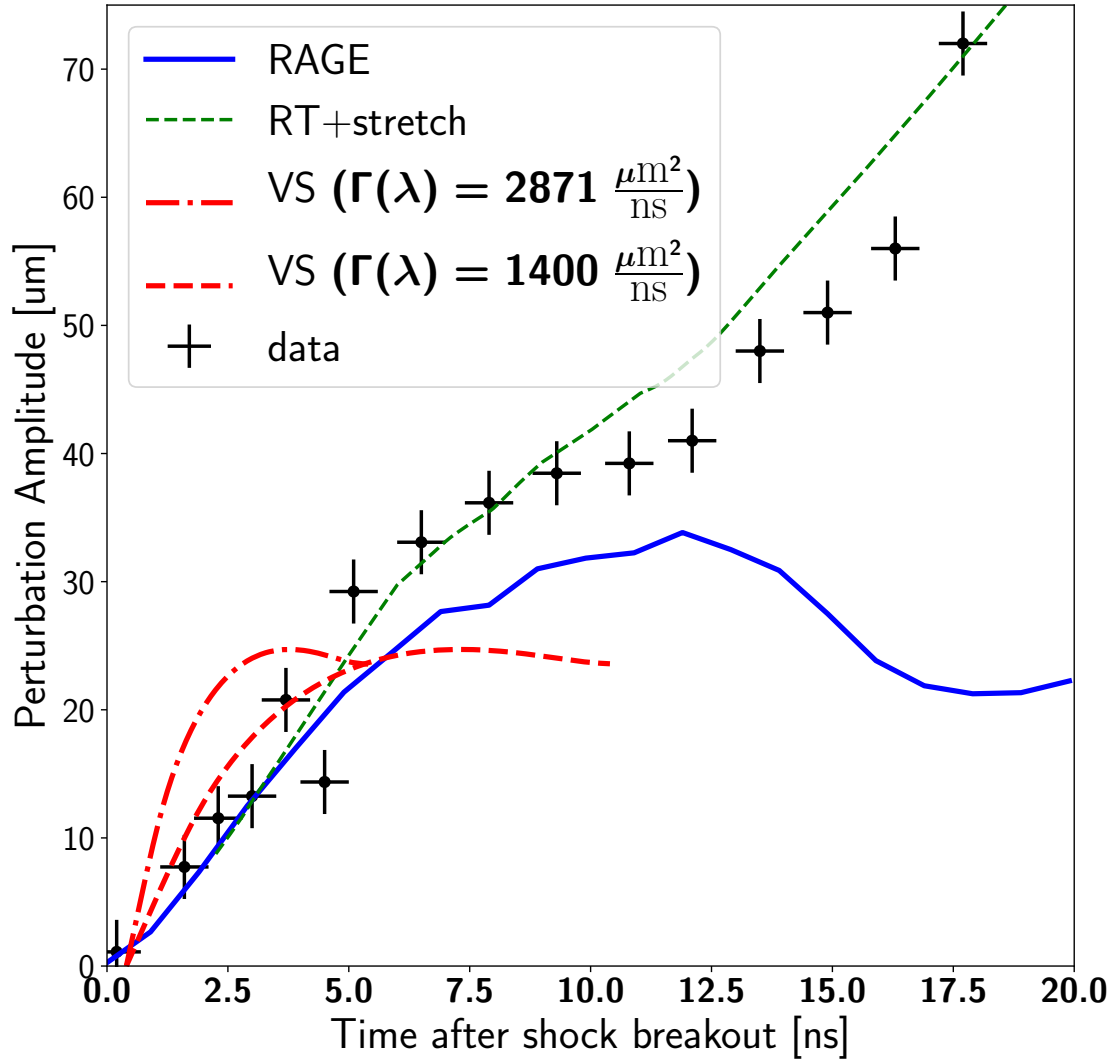
Figure 3.5 Experimentally measured perturbation amplitudes (cross bars) from experiments are compared to RAGE simulations (blue solid). The RAGE simulation with decompression and RT growth added in after the fact (see Eq. 3.2) from 1D simulations are plotted in green (dashed). Growth estimated from the vortex sheet model of Eq. 2.26 are plotted in red (dash-dot and dashed). The pre-shock perturbation for each of the plotted time histories is assumed to be a sinusoid with a 10 μm amplitude and 100 μm wavelength. The mean tilt between the shock and pre-shock interface is 30°.

expected to diverge from experiment after the impingement of the laser turn-off rarefaction and from vortex sheet computations due to secondary baroclinic vorticity deposition on the interface (due to both instability evolution and additional rarefactions from, e.g., the shock wall interaction). While the vortex sheet computation with the vorticity distribution exactly as calculated as in Eq. 2.23 over-predicts the mixing width growth rate at early times, note that it still reproduces the qualitative features from experiments and simulations well: the early time growth is impulsive, and in non-linear times the growth saturates (albeit temporarily for experiments) while the spikes and bubbles simultaneously develop co-rotating roll-up structures. This type of qualitative behavior is due to the shape of the vorticity distribution on the interface: the distribution is both strongly fluctuating and of approximately one sign.

3.4   Comparison between experiment and single mode, early time, RM and KH theory

For comparison, the growth rates predicted by the typical ansatz for RM and KH in the linear regime are calculated below. A sinusoidal perturbation with an amplitude of 10 μm and a wavelength of 100 μm is assumed. Bulk hydrodynamic parameters taken from RAGE simulations are used in the RM and KH ansatzes. The calculated instability growth rates predict that RM will dominate over KH at early times for which the assumptions of linearity hold. See Fig. 3.6.

The deformation of the interface by the passage of the shock is needed to estimate subsequent instability growth. The deformation depends on the relative speeds of the shock in the heavy material, s_{PAI}, and the post-shock speed of the interface, u_i. The perturbation on a shocked interface undergoes direct phase inversion when

$$u_i > s_{PAI} \tag{3.4}$$

is satisfied [31]. In this case, the velocity of the shocked material exceeds the shock velocity due to a reflected rarefaction at the interface, and the perturbation inverts during shock crossing. As reported in Table 3.1, $u_i = 40$ km s^{-1} whereas $s_{PAI} = 38$ km s^{-1}. The initial post-shock perturbation amplitude is then given by

$$\eta^* = \eta_0(1 - s_{PAI}/u_i), \tag{3.5}$$

which gives a post-shock amplitude of 0.5 μm. The interface as a whole undergoes this inversion as well, and as such the post-shock interface is roughly parallel to the initial shock.

In the incompressible linear limit, the Meyer & Blewett ansatz is used to estimate the RM
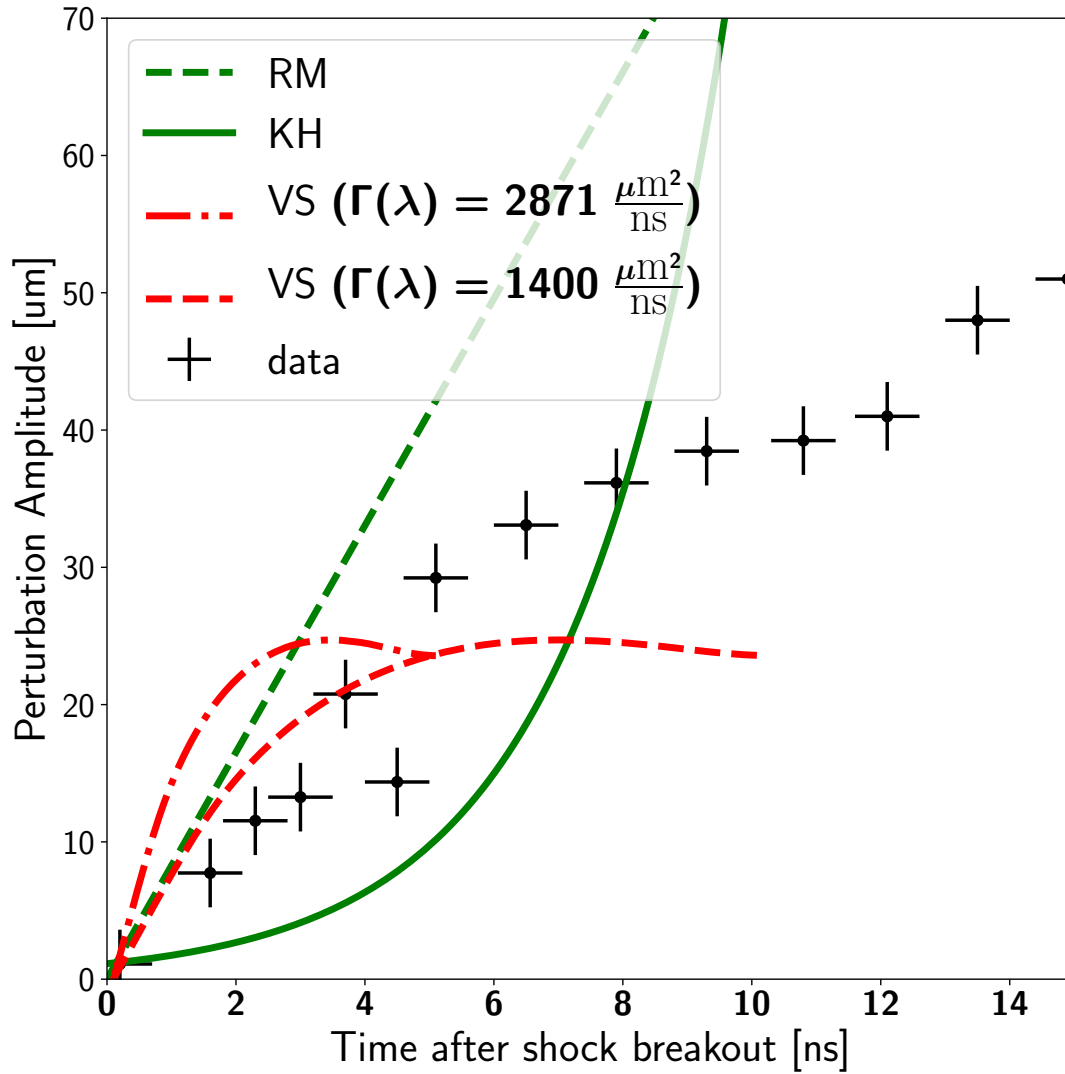
Figure 3.6 Perturbation amplitude time histories are plotted for experiment (cross bars), the vortex sheet model (dot-dashed and dashed red), KH (solid green), and RM (dashed green) predictions of interface growth. The experimental data and vortex sheet lines are identical to those shown in Fig. 3.5, i.e. with a 30° mean tilt and sinusoidal perturbation with an amplitude of 10 μm and wavelength of 100 μm.

growth for the reflected rarefaction case [57]. The ansatz gives the instability velocity as

$$v_{\text{MB}} = \left(\frac{\eta_0 + \eta^*}{2} \right) A_{\text{post}} u_{\text{i}} k,$$ (3.6)

where A_{post} is the post-shock Atwood number, u_{i}, is the post-shock interface velocity, $k = 2\pi/\lambda$ is the perturbation wavenumber, η_0 is the pre-shock perturbation amplitude, and η^* is the post-shock perturbation amplitude. This predicts an instability velocity of 9.5 μm ns^{-1}, which is approaching the shock recession speed (i.e., the speed at which the transmitted shock recedes from the interface) of 12 μm ns^{-1}. Previous work has demonstrated that compressibility effects become important when the spike velocity approaches the shock recession speed from the interface [33, 23, 31], as is the case here. We can obtain a more exact asymptotic linear growth rate following the method of Wouchuk [95], which shows how to calculate the growth rate for the rarefaction-reflected case, with arbitrary Atwood numbers at the interface and arbitrary shock strength. Following this calculation, we predict the slightly lower value of $v_{\text{RM}} = 8.3$ μm ns^{-1}. This growth rate is plotted in Fig. 3.6 (green dashed).

The Kelvin-Helmholtz growth rate is given by

$$\gamma_{\text{KH}} = \frac{k\overline{\Delta v}}{2} \sqrt{1 - A_{\text{post}}^2},$$ (3.7)

where $\overline{\Delta v}$ is the magnitude of the shear flow across the interface. The instability grows according to

$$\frac{d^2\eta}{dt^2} = \gamma_{\text{KH}}^2 \eta(t).$$ (3.8)

When there is no other forcing on the interface this leads to the perturbation time history

$$\eta(t) = \eta^* \exp(\gamma_{\text{KH}} t).$$ (3.9)

Taking the needed parameters from Table 3.1, $\gamma_{\text{KH}} = 0.43$ ns^{-1}. The time history given by Eq. 3.9 is shown in Fig. 3.6 (green solid) assuming $\eta^* = .5$ μm. In the case where linear RM and linear KH are coupled this will be a poor estimate of the KH growth, as the forcing is dependent on the amplitude of the perturbation. Furthermore, the assumptions underlying linearity are violated almost immediately, and the late time KH amplitude is expected to saturate at $0.28\lambda \approx 24\mu$m (as is observed in the vortex sheet computation).

The above estimates illustrate the importance of inspecting the shape of the vorticity distribution on an interface with a finite pre-shock perturbation and tilt. In the estimates given in this section, RM growth is predicted to dominate at early times, and the reduction of growth at intermediate

times will be predicted via late-time, single mode RM models which exhibit $log(t)$ dependence [71]. However, correctly noting the dominance of RM-like growth of the interface perturbation envelope will not predict the correct interface morphology, or distribution of vortices, in the late-time flow. Examining the vorticity distribution on the interface at early times allows one to both predict the type of growth at early times, while simultaneously allowing one to make a reasonable guess as the late time state of the interface.

3.5   Conclusion

In conclusion, experiments were performed to measure interface evolution on a shocked, oblique interface with a 10 μm amplitude, 100 μm wavelength sinusoidal perturbation and 30° tilt were conducted on Omega-EP. Experimental results were compared to both RAGE simulations and vortex sheet computations. The vortex sheet model of Chapter 2 was found to overpredict the amount of shear on the interface as well as the initial instability velocity, but still captured qualitative features of interface perturbation well. After normalizing the vorticity distribution, the vortex sheet computation matches experiments and simulations well at early times. RAGE simulations and experiment agree well until the onset of the laser turn-off rarefaction at $t \approx 5$. Future work will go in several directions. For the vortex sheet model, computational studies are needed to validate the vortex deposition approximation. Future work in RAGE will utilize the laser package to model the laser turn-off rarefaction, allowing 2D simulations of coupled RM, KH, and RT growth on oblique interfaces. Future experimental work will investigate intermediate tilts, in order to study instability evolution where the asymptotic state is some intermediate between KH and RM. Experiments studying mode coupling, and broadband, late time mixing layer behavior will be of particular interest, as the theory contained herein can hopefully be extended to predict whether late-time mixing layer growth rates are dominated by RM like or KH like processes.

Chapter 4

Tailored vorticity distributions on HED interfaces.

In the work of Chapter 2, I extended the circulation calculation of Hurricane, 2008 [32] to include a mean tilt between the shock and interface, as well as calculate the vorticity distribution in addition to the circulation over one wavelength. This lead to a difference in the way instability growth was predicted: in Hurricane, the vorticity was assumed to be localized to one point per wavelength starting at t=0 (referred to as the discrete vortex model), whereas in Chapter 2 the vortex sheet evolution was predicted using a discretized, regularized, Birkhoff-Rott equation which took into account the spatial distribution of vorticity along the post-shock interface. An interesting question is: can the work of Chapter 2 be used to predict what interface would evolve according to the discrete vortex model presented in Hurricane, 2008 [32]?

In Chapter 2, I estimated the vorticity distribution on a shocked, sinusoidally-perturbed interface, and found that (Eqs. 2.19 and 2.23)

$$
\omega(x,y) = \frac{\Delta p \Delta \rho}{u_s \bar{\rho}^2} \delta(y - y_1(x)) \hat{n} \times \hat{y}, \text{ where}
$$

$$
\hat{n} \times \hat{y}(\tau) = (-1) \frac{\sin\theta + ka\cos\theta\cos(k\tau)}{\sqrt{1 + (ka)^2\cos(k\tau)^2}} \hat{z}.
$$

(4.1)

Recall that Δp is the pressure jump across the incoming shock, $\Delta \rho$ is the density jump across the pre-shock interface, u_s is the incoming shock speed, $\bar{\rho}$ is the average of the heavy and light pre-shock densities, $y_1(x)$ gives the pre-shock interface curve, $\hat{n}$ is the interface surface normal, and $\hat{y}$ is the incoming shock normal. The mean tilt between the interface and incoming shock is given by θ, a is the amplitude of the initial sinusoidal perturbation, k is the wavenumber of the initial sinusoidal perturbation, and τ is a parameter of the interface.

As is discussed in Appendix A, this equation for the vorticity distribution is really an expression for the local tilt (between the pre-shock interface and incoming shock) along the interface, and the assumption of a sinusoidal perturbation was unnecessary. Due to the extremely large compression of the initial interface structure ($\eta_o/\eta^* \sim 20$), it is reasonable to assume the interface has no spatial

structure immediately post-shock. Letting $\hat{x}$ point along the shock front (as above), the vorticity distribution is a function of the local tilt, i.e.

$$\frac{d\Gamma}{ds}(x) \propto \tan(\theta(x)) \propto \frac{dy_1}{dx}. \tag{4.2}$$

From this, given some desired vorticity distribution, we can estimate the pre-shock interface needed to produce that vorticity distribution along the post-shock interface.

The discrete vortex model assumes a set of point vortices each separated by the same distance. Given the relation between sheet strength and and tilt on the interface in Eq. 4.2, I can guess that in order to have vorticity concentrated at a countable number of points, the tilt must also be concentrated at a countable number of points. This corresponds to a staircase perturbation.

In this chapter, I will first show how to make flows which grow approximately according to the unregularized discrete vortex model (DVM) analytically. I will then compare predictions from the DVM to RAGE simulations of the discussed interfaces. I will also discuss preliminary experiment results which measure this instability growth.

4.1   Periodic, discrete, vortices from oblique interfaces

A schematic of what I will call a "single-mode" staircase is shown in Fig. 4.1. Each step of the stair-case consists of a horizontal section (parallel to the shock front), and a vertical section (normal to the shock front). The width is called λ, and the height ℓ. Accordingly, the density gradient at the interface will be parallel to the shock pressure gradient on the horizontal portions, and orthogonal to the pressure gradient on the vertical sections of the staircase. Assuming marginal direct phase inversion, the interface will be nearly flat post-shock and roughly parallel to the x-axis. This will result in a vorticity distribution which is approximated by a sum of delta functions,

$$\omega(x,y) = \sum_n \Gamma(\ell)\delta(x-n\lambda)\delta(y), \tag{4.3}$$

where $\Gamma(\ell)$ is the vortex strength (which to first order is a function of ℓ alone), δ is the Dirac delta, and n is summed over the integers from $-\infty$ to $+\infty$.

The circulation per vortex (or vortex strength) $\Gamma(\ell)$ may be estimated as follows. Recall from Chapter 3 that the circulation calculation from Chapter 2 (in particular, Eq. 2.21) disagrees with RAGE simulations. Appendix A shows that the vorticity deposition model in Chapter 2 is problematic. I will therefore posit as an ansatz that the vortex strength will grow linearly with the stair
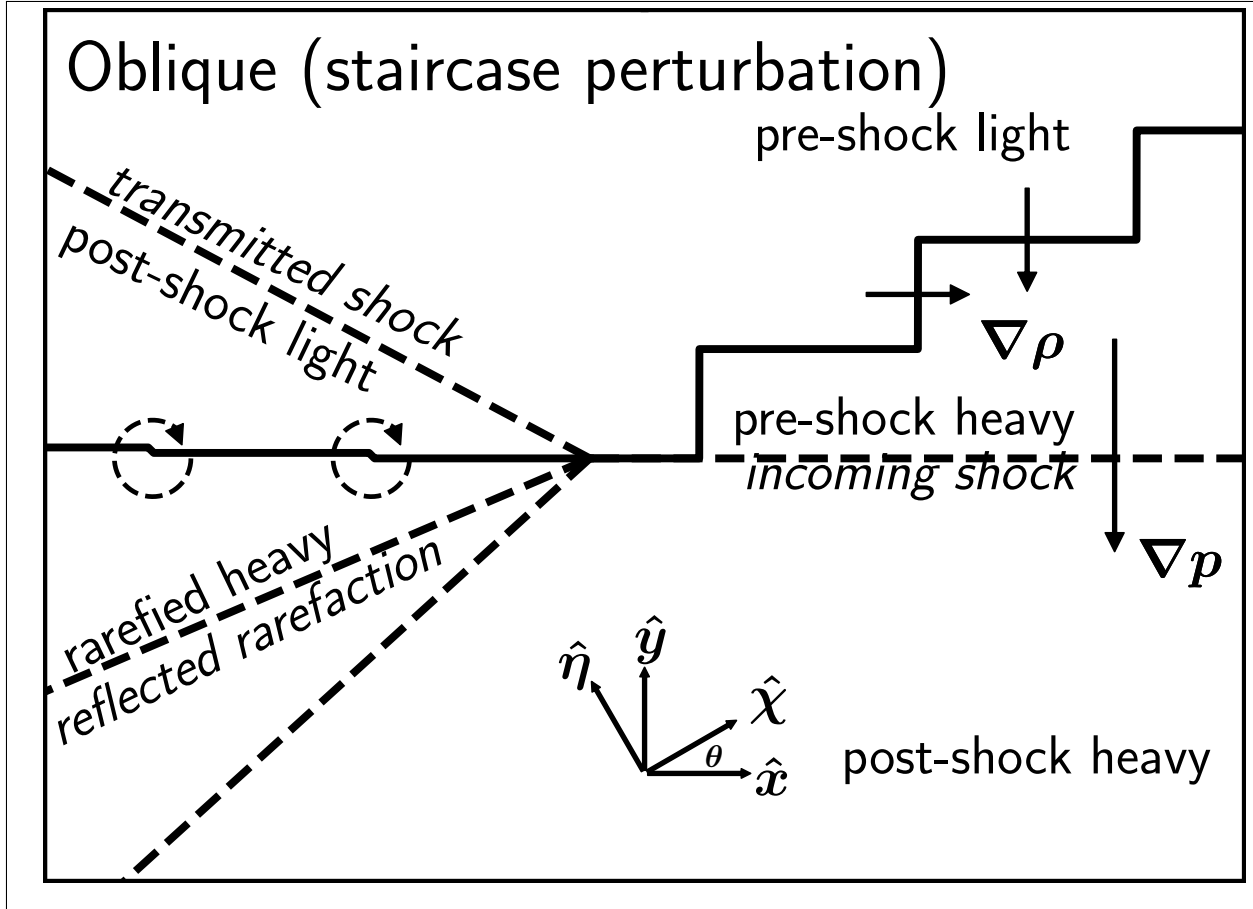
Figure 4.1 A schematic of the single-mode staircase perturbation. The stair width is 100 μm and the stair height is 50 μm, giving a mean tilt of 30 degrees. The shock is incident from the bottom and traveling upwards.

height, and extract the proportionality from RAGE simulations. In mathematical form this is

$$\Gamma(\ell) = \frac{d\Gamma}{d\ell}\ell. \tag{4.4}$$

As above, ℓ is the stair height, $\Gamma(\ell)$ is the vortex strength (or circulation per vortex), and $d\Gamma/d\ell$ is the sheet strength created by the incoming shock interacting with the vertical portion of a stair (which will be taken from RAGE simulations). For the shock and material properties from experiments and simulations in Chapter 3, the sheet strength is $d\Gamma/d\ell \approx 27$ μm ns^{-1}.

4.1.1 Expected growth rates and saturation heights for staircase perturbations

We can then predict the evolution of an interface with the vorticity distribution of Eq. 4.3 using Eq. 2.24 with the regularization parameter, δ, set to zero. Restating Eq. 2.24 with $\delta = 0$:

$$\frac{dx}{dt} = \frac{\Gamma(\ell)}{4\lambda} \frac{\sinh(\frac{2\pi y}{\lambda})}{\cos(\frac{\pi x}{\lambda})^2 + \sinh(\frac{\pi y}{\lambda})^2}$$
$$\frac{dy}{dt} = \frac{\Gamma(\ell)}{4\lambda} \frac{\sin(\frac{2\pi x}{\lambda})}{\cos(\frac{\pi x}{\lambda})^2 + \sinh(\frac{\pi y}{\lambda})^2}. \tag{4.5}$$

For the regularized Discrete Vortex Model, the initial instability velocity is given by

$$v_{rDVM} = \frac{\Gamma(\ell)}{4\lambda |\delta| \sqrt{\delta^2 + 1}}. \tag{4.6}$$

This implies the instability velocity asymptotes to infinity as δ goes to zero, so that the initial DVM instability velocity is always infinite. However, the instability velocity is only infinite at exactly t=0 (equivalently, the interface is exactly flat), so that the amplitude remains finite. The saturation height is the typical late-time KH saturation,

$$h(t \to \infty) = 0.28\lambda. \tag{4.7}$$

An example of the evolution of such an interface is shown in Fig. 4.2. The initial condition is shown on the bottom, and the late-time state of the interface is shown on the top. As in Fig. 4.1 the shock is incident from the bottom.

How well the discrete vortex model will predict the post-shock interface rests on the following conditions: 1) there is no initial post-shock physical structure on the interface, 2) the vorticity is deposited quickly compared to the dynamics of the system so that the vorticity can uniformly be treated as if it is deposited at $t = 0$, and 3) there is no other vorticity in the system. Condition (1) requires that either the pre-shock interface perturbation is small, or that the shock strongly compresses any structure on the interface. Condition (2) requires that the perturbation is small. Condition (3) requires that any secondary sources of vorticity be small, this includes both finite Atwood effects at the interface (secondary baroclinic vorticity generation) and that any fluctuations in the transmitted and reflected waves are small. In general, these conditions are best satisfied when the perturbation on the interface is small ($\lambda \gg \ell$) and complications will arise as the perturbation height increases.

Condition (1) is broadly satisfied for the shock and material properties described in Chapter 3.
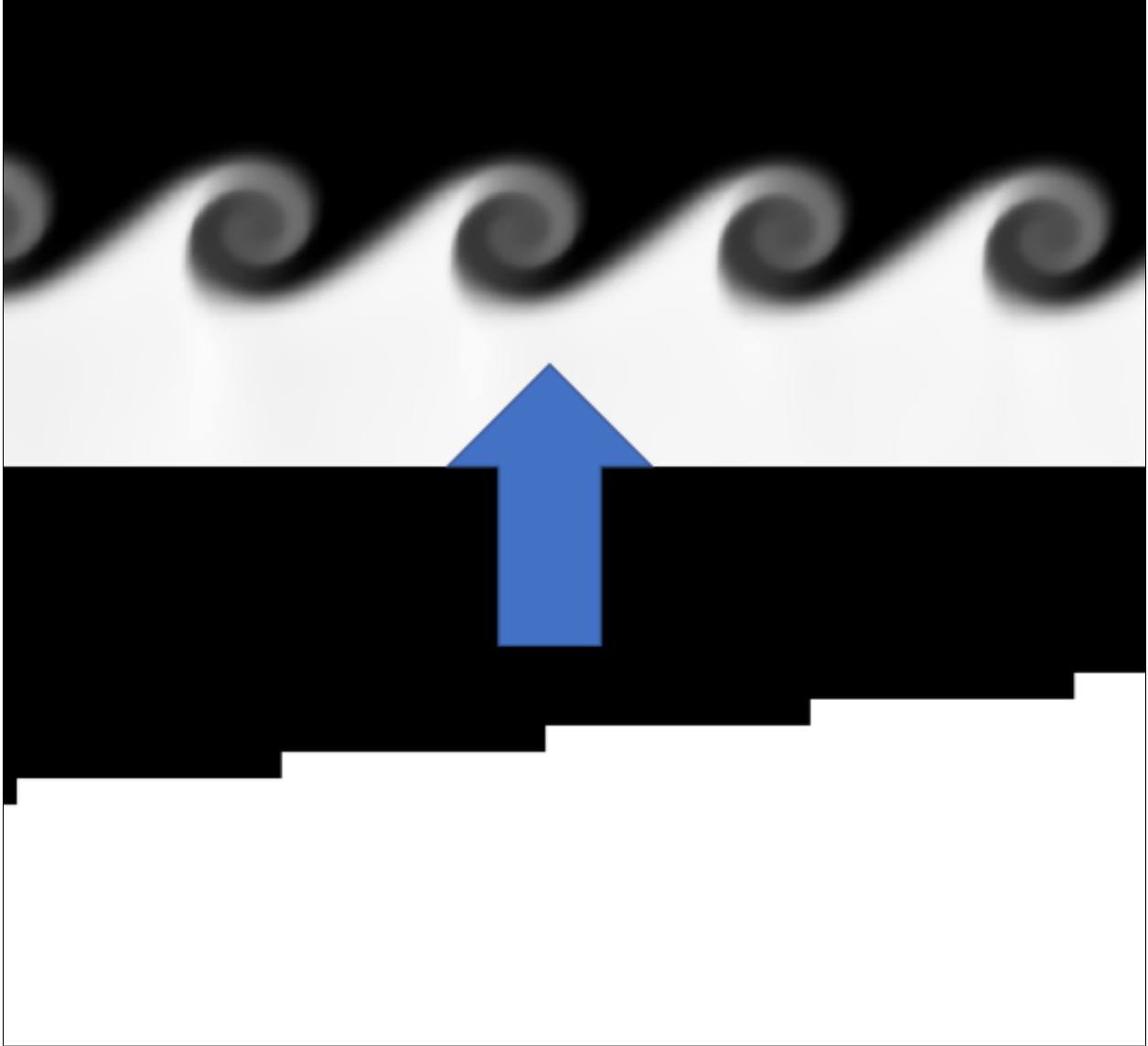
Figure 4.2 An example of the time evolution of a stair-step perturbation. The shock and material properties are the same as in the work discussed in Chapter 3. The shock is incident from the bottom of the image. In the bottom image the initial condition is shown (i.e. the interface is unshocked). In the top image, the interface is shown ~ 30 ns post-shock. The two images show the same range of x values, but the y window is shifted to follow interface movement. Each stair has a height of 10 μm and a width of 100 μm, so that secondary effects remain unimportant and the DVM predicts interface growth well. The envelope growth is saturated in the top image, and the full width is 56 μm ($= 0.56\lambda$), as is expected from the discrete vortex model.

In particular, the interface undergoes marginal direct phase inversion during the shock passage, so that any initial structure on the interface is compressed by a factor of ~ 20. The post-shock stair height (ℓ^*) will therefore be small compared to the stair width even for large pre-shock aspect ratios. E.g., a pre-shock aspect ratio of width:height of 100:50 will become a post-shock aspect ration of 100:2.5.

Condition (2) can be quantified by comparing the dynamic timescale of the interface evolution to the shock crossing time for a single perturbation. The dynamic timescale is taken to be an eddy-turnover time for a vortex on the interface. The velocity profile around a single vortex is given by $\vec{u} = \Gamma/2\pi r\hat{\phi}$. The radius of each vortex is $\lambda/2$, so that the velocity on the "outside" of each vortex can be approximated as $u = \Gamma(\ell)/\pi\lambda$. The time for a vortex to undergo one rotation is then

$$\tau_{\text{eddy}} = \frac{2\pi r}{u} = \frac{(\pi\lambda)^2}{\Gamma(\ell)} = \frac{2\pi^3}{k_\lambda^2 \Gamma(\ell)},$$ (4.8)

where $k_\lambda = 2\pi/\lambda$. This is typically referred to as an eddy turnover time. Note that this time decreases with ℓ and increases with λ.

The shock crossing time, τ_ℓ is the time it takes the shock to propagate a distance ℓ, the height of one staircase, is given by

$$\tau_\ell = \frac{\ell}{u_s}.$$ (4.9)

I will call the ratio of these two characteristic times f, i.e.

$$\begin{aligned}
f &= \frac{\tau_{\text{eddy}}}{\tau_\ell} \\
&= \frac{2\pi^3}{k_\lambda^2 \Gamma(\ell)} \frac{u_s}{\ell} \\
&= \frac{2\pi^3}{k_\lambda^2 \frac{d\Gamma}{d\ell}\ell} \frac{u_s}{\ell} \\
&= \frac{2\pi^3}{(2\pi)^2 \frac{d\Gamma}{d\ell}} \frac{u_s \lambda^2}{\ell^2} \\
&\approx 2.2 \left(\frac{\lambda}{\ell}\right)^2.
\end{aligned}$$ (4.10)

In the last step, I have used the value of $d\Gamma/d\ell$ given in the previous section and the incoming shock speed given in Chapter 3. The post-shock interface should behave according to the discrete vortex model when $\tau_{\text{eddy}} \gg \tau_\ell$, equivalently $f \gg 1$ or $\lambda \gg \ell$. As the value of f decreases, secondary effects lead to the significant generation of secondary vorticity, which strongly alters the resultant instability evolution.

Condition (3), the lack of secondary vorticity generation, will most strongly be violated by the rarefaction which impinges on the experiment when the lasers incident on the ablator turn off. Therefore, any post-shock interface evolution can only be expected to evolve according to the DVM so long as that rarefaction has not impinged on the interface. Other sources will also modify instability growth. A second, counter-rotating vortex, is generated by complications of the

shock-interface interaction, which complicates growth as the stair height increases.

4.2 RAGE simulations of oblique interfaces with staircase perturbations.

In order to evaluate how well the discrete vortex model predicts instability evolution, it should be compared to simulation predictions for interface evolution. Here, RAGE (an Eulerian radiation-hydrodynamics code with adaptive mesh refinement [22]) simulations of a shock interacting with an oblique interface with a staircase perturbation are presented. The material and shock properties from Chapter 3 are advantageous for DVM experiments. In particular, the interface undergoes marginal direct phase inversion so that any initial structure on the interface is strongly compressed by the shock. As such, in this Chapter, I will use the same shock and material properties as in Chapter 3, so that the only difference is the initial perturbation and tilt of the pre-shock interface. In RAGE, this corresponds to using the same EOS and initialization conditions as were used in Chapter 3. See Section 3.2 for more details about the RAGE simulations.

The shock is incident in a 1.45 g cm^{-3} PAI plastic. A 100 mg cm^{-3} foam is adjacent to the plastic. The staircase perturbation describes the shape of the contact surface between the plastic and foam. The shock is created via a mass-inlet condition in simulations, as was described in Chapter 3. Note that this implies the simulation will only match experiments so long as the shock is supported in the experiment. The shock and interface properties are stated in Tables 4.1 and 4.2. These are essentially identical to the shock and material properties reported in Chapter 3. The primary difference is due to the different perturbation type: the amount of circulation per vortex (and therefore shear across the interface) from RAGE simulations is reported for a staircase height of $\ell = 5$ μm here. For other staircase heights, the amount of circulation per vortex can be estimated by

$$\Gamma(\ell) = \Gamma(\ell = 5 \ \mu\text{m})\frac{\ell}{5 \ \mu\text{m}}. \tag{4.11}$$

This is equivalent to Eq. 4.4 with

$$\frac{d\Gamma}{d\ell} = \frac{\Gamma(\ell = 5 \ \mu\text{m})}{5 \ \mu\text{m}}. \tag{4.12}$$

We performed RAGE simulations for 10 cases of the staircase perturbation. In each case the stair width is 100 μm, the shock and material properties are held constant, and the stair height is varied. At small stair heights, the interface evolution is well described by the DVM. As the height is increased, the behavior diverges dramatically. I will first discuss the case in which the DVM

77

Table 4.1 Bulk flow parameters are reported. The shock speed in the heavy material is estimated experimentally from the shock breakout time along the interface. All other quantities are determined from 2D RAGE simulations which have been tuned to the measured parameter. γ_{eff} is calculated from the compression across the primary and transmitted shocks, respectively, u_s is the shock speed in each material, P_s is the post-shock pressure in each pressure, and u_y is the post-shock fluid speed in the direction of shock propagation in the lab frame. Note that the post-rarefaction pressure in the heavy material will be equal to the post-shock pressure in the foam.

	γ_{eff}	u_s	P_s	u_y
plastic	1.90	$38\frac{\mu\text{m}}{\text{ns}}$	13.5 Mbar	$25.1\frac{\mu\text{m}}{\text{ns}}$
foam	1.57	$52\frac{\mu\text{m}}{\text{ns}}$	2.1 Mbar	$39.9\frac{\mu\text{m}}{\text{ns}}$

Table 4.2 Parameters describing the properties of the interface. The pre (post) shock Atwood number is given by A_{pre} (A_{post}). The experimental post-shock interface velocity, $u_i(\exp)$, is estimated experimentally from the mean interface location in radiographs of the post-shock interface. The simulated post-shock interface velocity is given by u_i. The circulation of a single vortex is reported from RAGE simulations for a 5 μm initial stair height.

	A_{pre}	A_{post}	u_i	u_i (exp)	$\Gamma_{\text{RAGE}}(\ell = 5\ \mu\text{m})$
interface	0.87	0.67	$39.5\frac{\mu\text{m}}{\text{ns}}$	$40\frac{\mu\text{m}}{\text{ns}}$	$135\ \frac{\mu\text{m}^2}{\text{ns}}$

and simulation agree well, and then discuss how non-linear effects lead to disagreements as the pre-shock stair height is increased.

4.2.1 Comparison of small stair height simulations to DVM growth

In Fig. 4.3 I show perturbation amplitude histories for staircase perturbations with a height of 5, 10, and 15 μm. In Fig. 4.3a the dimensional amplitude histories are shown, whereas in Fig. 4.3b the non-dimensional amplitude histories are shown. The non-dimensional DVM perturbation amplitude history is also plotted. The time for each history is offset so that a time of zero corresponds with the shock breakout time (i.e. when the vertical section of the stair has just been fully shocked). The perturbation amplitude is extracted from simulation using an unsharp mask. The perturbation amplitude is taken to be half of the peak-to-valley of the unsharp-mask over one wavelength.

The amplitudes are non-dimensionalized according to the same formulae given in Section 2.4.1. Restating, these are

$$
\begin{aligned}
x^* &= x/\lambda, \\
y^* &= y/\lambda, \text{ and} \\
t^* &= t\frac{\Gamma(\ell)}{\lambda^2}.
\end{aligned}
\tag{4.13}
$$

As the stair width, λ, is held constant between cases, the only difference in the non-dimensionalization
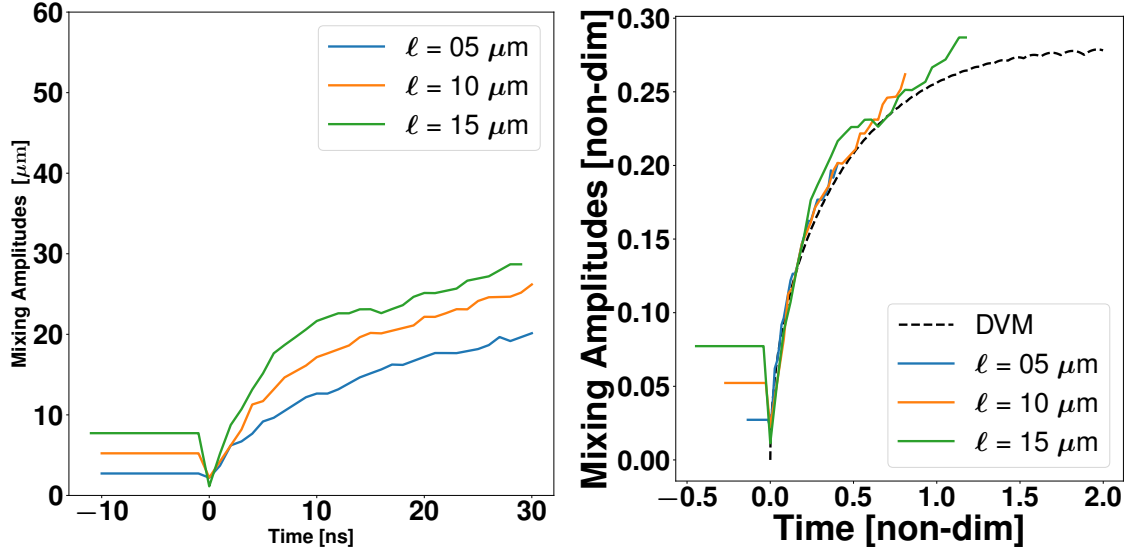
78

(a) Dimensional perturbation amplitude histories for three pre-shock stair heights.

(b) Non-dimensional perturbation amplitude histories for three pre-shock stair heights.

Figure 4.3 Both dimensional and non-dimensional perturbation amplitude histories are shown for several pre-shock stair heights. The simulations shown have a pre-shock stair height of 5 μm, 10 μm, and 15 μm. The stair width is held constant at 100 μm. In the non-dimensional plot the simulation results agree well with the DVM.

is introduced via the $\Gamma(\ell)$ dependence of the non-dimensional time. For fixed dimensional time step, this implies that the associated non-dimensional time step will increase linearly with stair height.

On the non-dimensional plot, the perturbation amplitudes for all three cases shown agree well with the DVM prediction. This indicates that the vorticity distribution posited in Eq. 4.3 is well matched in simulation. This can be seen directly by inspecting the vorticity and density in simulations. In Fig. 4.4 I show the vorticity and density from RAGE simulations of the 5 μm stair height at several time steps. In the left-most image, the shock is seen incident from the bottom, and the initial condition is seen in the density plot. In the middle image, interface evolution less than a nanosecond post-shock is shown. In the right-most image, the interface is shown $\approx$ 30 ns post-shock.

Note that some non-linear effects are evident in the vorticity distribution of the 5 μm stair height case, even though the perturbation amplitude is well is well predicted by the DVM. A smaller, counter-rotating, vortex is evident in the vorticity distribution immediately post-shock (Fig. 4.4b). The negative vorticity (blue), is dominant, and the positive vorticity (yellow) is due to non-linear effects. While the amount of positive vorticity present is non-trivial, the spatial separation between the primary and counter-rotating vortices is small. The counter-rotating vortex will only strongly impact flow in a region about the size of the separation between the two vortices. As the perturbation stair height increases, the separation between the two vortices grows as the initial stair height
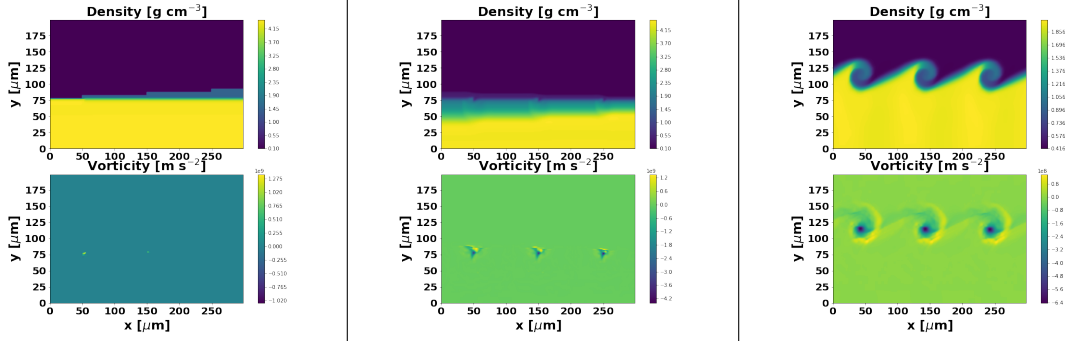
(a) The shock (incident from the bottom of the image) is seen crossing the interface.

(b) An image of interface evolution less than a nanosecond post-shock.

(c) An image of interface evolution ≈ 30 ns after shock breakout.

Figure 4.4 Plots of material density (top) and the vorticity distribution (bottom) are shown at several time steps for a pre-shock staircase perturbation with a height of 5 μm and a width of 100 μm. Left (a), the initial condition is shown. The incoming shock is seen at the bottom of the density image, and is propagating upwards. Middle (b), the interface is shown less than a nanosecond after shock breakout. Right (c), the interface is shown ≈ 30 ns after shock breakout.

increases, and the impact of the counter-rotating vortex grows in kind. For the three cases plotted in Fig. 4.3, the separation between the primary and counter-rotating vortices remains small, and the interface evolution is well approximated by the DVM.

4.2.2 Non-linear effects: Divergence from the DVM

As the perturbation height is increased, non-linear effects in the shock-interface interaction alter instability evolution. In Fig. 4.5 I plot the perturbation amplitude histories for pre-shock stair heights between 5 μm and 50 μm in 5 μm increments. Both the dimensional (Fig. 4.5a) and non-dimensional (Fig. 4.5b) amplitude histories are shown. For large values of the stair height, it is clear that the perturbation amplitude significantly diverges from the DVM prediction. As the pre-shock stair height increases the perturbation amplitude history significantly overgrows the DVM prediction, including overgrowing the expected saturation amplitude of the DVM (0.28λ).

Due to complications in the shock-interface interaction, a second, counter-rotating but weaker vortex is generated in addition to the primary vortex. As the stair height is increased, the spatial separation between the counter-rotating vortex and the primary vortex is increased. This implies that the counter-rotating vortex will have a larger effect as the stair height is increased. Density and vorticity distributions from RAGE simulations for a staircase perturbation with a pre-shock height of 25 μm and a height of 100 μm are shown at several times in Fig. 4.6. At late times, note that the counter-rotating vortex has formed a lopsided, unbalanced, RM-like mushroom cap inside of the
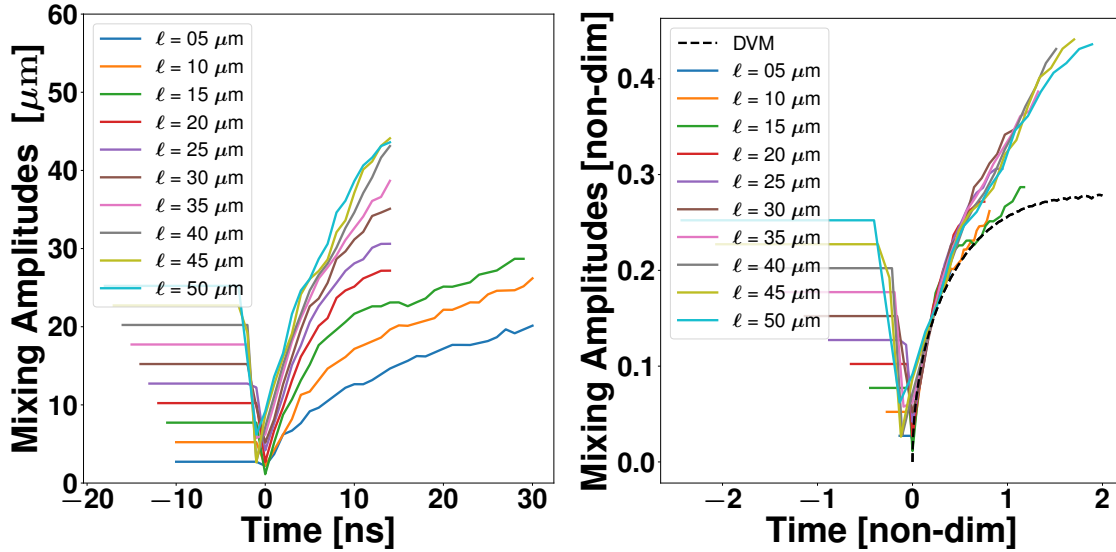
(a) Dimensional perturbation amplitude histories for ten pre-shock stair heights.

(b) Non-dimensional perturbation amplitude histories for ten pre-shock stair heights.

Figure 4.5   Both dimensional and non-dimensional perturbation amplitude histories are shown for several pre-shock stair heights. The simulations shown have a pre-shock stair height of 5 μm, 10 μm, and 15 μm. The stair width is held constant at 100 μm. In the non-dimensional plot the simulation results agree well with the DVM. For larger perturbations, the time over which the amplitude is plotted is curtailed for stair heights of 20 μm and larger. In these cases, complications in the shock-interface interaction causes the unsharp-mask to produce erratic results for the perturbation amplitude at late times.

KH roll-up. Contrast this to the 5 μm height case (Fig. 4.4), where the counter-rotating vortex has no observable impact on behavior at late times.

4.3   Preliminary experimental results

In order to confirm the results of theory and simulation, experiments are needed. In the RAGE simulations of the previous section, I kept the material properties and shock properties used in Chapter 3. This implies that I can take the experimental platform from Chapter 3, and machine a staircase perturbation onto the plastic-foam interface in order to produce DVM growth. In this section, I will first give a brief description of the experimental platform. I will then describe the diagnostic used to measure evolution. Finally I will compare experimentally measured perturbation amplitudes to both RAGE simulation and the DVM.
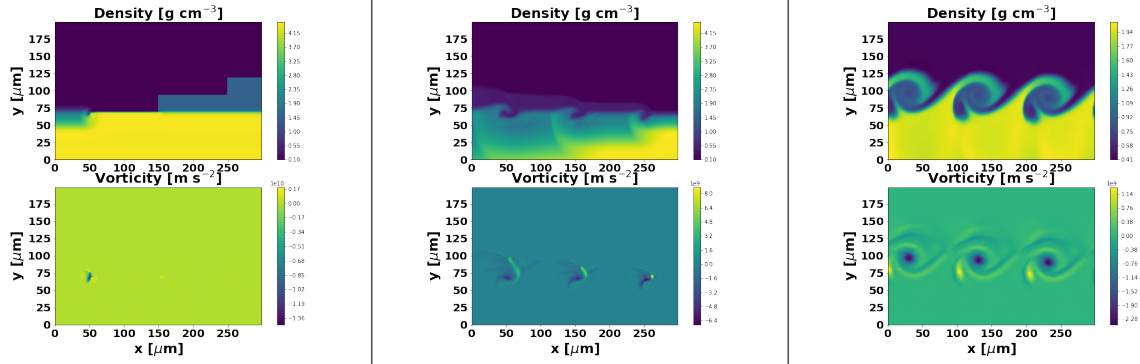
(a) The shock (incident from the bottom of the image) is seen crossing the interface.

(b) An image of interface evolution less than a nanosecond post-shock.

(c) An image of interface evolution $\approx$ 30 ns after shock breakout.

Figure 4.6 Plots of material density (top) and the vorticity distribution (bottom) are shown at several time steps for a pre-shock staircase perturbation with a height of 25 μm and a width of 100 μm. Left, the initial condition is shown. The incoming shock is seen at the bottom of the density image, and is propagating upwards. Middle, the interface is shown less than a nanosecond after shock breakout. Right, the interface is shown $\approx$ 30 ns after shock breakout.

4.3.1 Experiment description

The experimental platform consists of several stacked materials inside of a shock tube. There is a 1.45 g cm^{-3} polyamide-imide (PAI) ablator, abutted by a 100 mg cm^{-3} plastic foam. A 100 μm deep, 100 μm wide trench is machined into the PAI, and a density matched piece of iodinated plastic ($C_{50}H_{47}I_3$) is inserted into the trench. The perturbation is machined onto both the PAI/CHI, and the foam. All of these materials are located inside of a 200 μm thick plastic shock tube. Note that this experimental platform is essentially identical to that used in Chapter 3, other than the perturbation on the interface, and the use of an Mn He-α crystal with the SCI for diagnosing interface evolution.

To create a shock, three Omega-EP long pulse beams, with a wavelength of 351 nm, simultaneously irradiate the ablator. The beams have a 10 ns pulse duration and square pulse temporal profile. The beams have a combined energy of $\sim$ 14 kJ. The beams are each smoothed with a distributed phase plate (DPP), and have a 6th order super gaussian spatial profile with a 550 μm radius. This gives an irradiance of 1.4×10^{14} W cm^{-2}. The resulting shock and material properties are given in Tables 4.1 and 4.2.

To diagnose interface evolution, a fourth long pulse beam is used to create manganese (Mn) He-α photons by irradiating a thin Mn foil. A 3 ns pre-pulse is used to create an ablation plume of the foil, followed by a 500 ps square pulse. The pre-pulse has previously been shown to increase Mn He-α photon yield [21]. The manganese He-α pass through the physics package, and are then collected by a bent crystal and focused onto a CCD. The photons are preferentially absorbed in the

Figure 4.7   A radiograph of a post-shock staircase perturbation. The initial height of the stair was 25 μm, and the width is 100 μm. The image was taken 24 ns after the drive beams are first incident on the ablator. The leftmost visible spike is $\sim$ 14 ns post-shock, and each stair is shocked 0.625 ns after the vortex to its left while the shock remains planar.

CHI layer, creating contrast at the heavy-light interface.

A radiograph of a post-shock staircase perturbation is shown in Fig. 4.7. Note that the spikes and bubbles are rolled over, as is expected for a KH-like late time state. However, the diagnostic resolution is insufficient to resolve the interior structure of the roll-up. Non-dimensional perturbation amplitudes extracted from this radiograph, restricted to the three centermost vortices, are compared to perturbation amplitude time histories from both RAGE and the discrete vortex model in Fig. 4.8. The time at which the laser turn-off rarefaction arrives at the interface is indicated by the vertical line (black dotted). The experimental measurement is larger than both the RAGE simulation and the DVM prediction. Note that neither RAGE nor the DVM prediction take into account the additional perturbation growth from the laser turn-off rarefaction, so that the experiment is expected to outgrow RAGE and the DVM.

The contribution of RT and decompression to interface perturbation growth is also plotted in Fig. 4.8 (blue dashed line). As in Chapter 3, this additional growth is estimated using the equation

$$\frac{d\eta}{dt} = v_{\text{RAGE}}(t) + \omega(t)\eta(t) + v_{\text{b}}(t) + v_{\text{s}}(t), \tag{4.14}$$

83
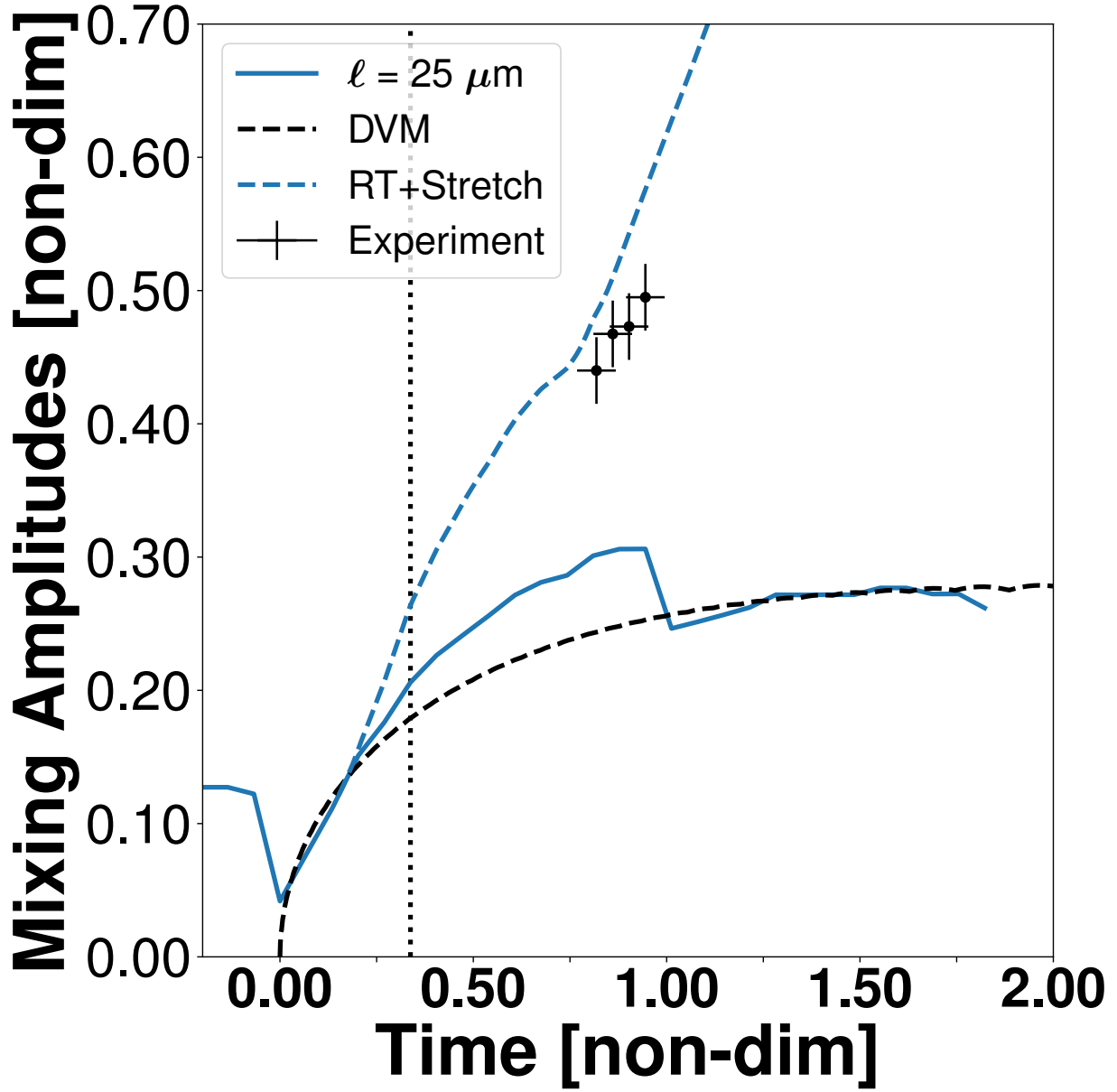
Figure 4.8 The non-dimensional perturbation amplitude histories are shown for a pre-shock stair height of 25 μm and width of 100 μm. Experimentally measured perturbation amplitudes (black cross bars), as well as perturbations from RAGE simulations (blue) and the discrete-vortex model (black dashed). The time the laser turn-off rarefaction reaches the interface is shown (black dotted line).

where $v_{b/s}(t)$ are the late time RT bubble and spike velocities from [24], given by

$$v_{b/s}(t) = \sqrt{\frac{2A(t)}{1 \pm A(t)} \frac{g(t)}{3k}},$$

(4.15)

v_{RAGE} refers to the instability velocity in the RAGE simulations, $A(t)$, $g(t)$, and $\omega(t) = \left[\frac{\partial u}{\partial x}\right]_{x=x_{\text{int}}(t)}$ are taken from HYADES simulations. HYADES is a 1D, Lagrangian, radiation-hydrodynamics code with includes a laser package [44]. Note that $A(t)$ is the time dependent Atwood number across the interface, and $g(t)$ is the time dependent acceleration of the interface. This model does a reasonable job of predicting the additional growth of the interface perturbation due to the laser turn-off rarefaction, as can be seen from inspecting Fig. 4.8.

4.4 Conclusion

In conclusion, I have shown how to create a system which evolves according to the discrete vortex model presented in Hurricane, 2008 [32]. First, theory was presented arguing that a staircase perturbation results in DVM growth. Then, theory was compared to RAGE simulations of interface evolution for a shock interacting with a staircase perturbation. When the height of each stair was small compared to the width of each stair, the simulations closely match the prediction of the DVM. As the stair height increases, post-shock evolution diverges from the DVM prediction. Preliminary experimental results were also presented.

Chapter 5
The conclusion

5.1 Summary

In Chapter 2, I presented a method for predicting the evolution of a sinusoidally perturbed, shocked interface. The tilt between the interface and incoming shock was allowed to freely vary, as was the perturbation wavelength and amplitude. There were two components to this method: a model for vorticity deposition along the interface by the shock, and a model for kinematically evolving that vorticity distribution post-shock. The vorticity deposition model is an extension of that presented in Hurricane, 2008 [32] for the calculation of baroclinic vorticity in the KH geometry (i.e., the shock front is normal to the mean interface). The evolution of the post-shock interface was calculated using a regularized, periodic, kinematic vortex sheet method [38]. Vortex sheet methods have previously been used to separately describe both early and late-time behavior of KH and RM [80, 82, 81], here I presented the first use of vortex sheet methods to describe the coupling between RM and KH. I showed that the early and late-time behaviors of instability growth can be dominated by different instabilities. In particular, a limiting case was identified where early time growth was RM-like (meaning the perturbation amplitude grew linearly with time), whereas the late time behavior of the interface was KH-like (meaning that KH rollups formed).

In Chapter 3, I reported on RAGE simulations and Omega-EP experiments which confirmed the analytic predictions of Chapter 2. In particular, the case where the early time growth is RM dominated, whereas the late time behavior is KH dominated was investigated. Qualitatively good agreement was found between theory, simulation, and experiment. The vorticity deposition model over-estimated the amount of shear across the post-shock interface by a factor of ≈ 2 when compared to RAGE simulations (we cannot measure the shear in experiments so no direct comparison is possible). The vortex sheet computation overestimated the instability velocity at early times by a factor of ≈ 2 when compared to RAGE and experiments. When the vorticity distribution was normalized to match the amount of shear from RAGE simulations, the instability velocities agreed. The disagreement in instability velocity is likely due to limitations in the vorticity deposition model,

which disregards many details of the shock-interface interaction in exchange for being able to capture any interaction geometry reasonably well.

In Chapter 4, I present preliminary work on a different type of perturbation. A staircase perturbation results in vorticity deposition on only the vertical portions of the steps. This results in a vorticity distribution which is well described by a set of point vortices all separated by the stair width λ. This is the vorticity distribution associated with the discrete vortex model (DVM), which was previously used to predict interface evolution in the KH geometry in Hurricane [32]. Chapter 2 implicitly disagrees with Hurricane, 2008 [32], as different methods are used to evolve the post-shock interface. The staircase perturbation gives insight into this disagreement by showing what shock-interface interaction produces instability evolution that is well described by the DVM. RAGE simulations of the shock-staircase interaction show good agreement with the DVM so long as the initial stair height is not too large compared to the stair width.

5.2 Conclusions

The above work significantly clarifies the role of baroclinic vorticity generation in HED hydrodynamic instability experiments. The transition between Richtmyer-Meshkov and Kelvin-Helmholtz was explored by inspecting how the vorticity deposited on the interface by some incoming shock changed as the mean tilt between the shock and interface was varied. The calculated vorticity distributions were used to predict interface evolution using a desingularized Birkhoff-Rott equation. This description of shock-interface interaction yields insights into both the early and late-time behaviors of the interface, and shows that interface perturbation growth rates can be dominated by Richtmyer-Meshkov early in time, while still becoming Kelvin-Helmholtz like in both morphology and vorticity distribution at late times.

This can occur because the early and late time type of growth depend on different characteristics of the vorticity distribution. At early times, in the limit that the spatial structure on the interface is small, the first time derivative of the perturbation amplitude (i.e., instability velocity) is determined by the fluctuations in the vorticity distribution alone, irrespective of the mean value of that vorticity distribution. However, the late time behavior of the interface is determined by the distribution of signs of the vorticity distribution. If one has equal amounts of positive and negative vorticity along the interface, an RM-like late time state will result. However, if the vorticity along the interface is of only one sign, a KH-like late time state results. If the vorticity distribution along the interface is strongly fluctuating, but the vorticity is of one sign, the interface perturbation will grow impulsively at early times (like RM), but will evolve into a KH-like state at late times. This results in interface evolution which is dominated by KH at late times even when the KH contribution to perturbation

growth at early times is negligible.

5.3   Future Work

The late time perturbation growth rate on a shocked interface strongly varies with the type of late time growth. In particular, the late-time, multimode, Kelvin-Helmholtz growth rate is much larger than the late time, multimode, RM growth rate. Correctly predicting whether an interface will be RM-like or KH-like at late times therefore has important ramifications for processes where hydrodynamic instabilities on interfaces degrade performance. E.g., in ICF hydrodynamic instability growth is seeded by surface roughness on different capsule interfaces. This surface roughness is multimode, and the incoming shocks which drive instability growth (as well as the implosion as a whole) will typically have some tilt relative to the interfaces due to, e.g., asymmetries in the radiation which produces the shocks. If one only compares the linear RM and KH growth rates to determine what growth mechanism dominates, one will dramatically overestimate the shock tilt required to make KH dominant at late times.

The immediately apparent extension of the work presented in this dissertation is then to more directly interrogate the growth of multi-mode perturbations on oblique interfaces. The experimental platform used in this dissertation has also been used to measure multimode RM growth, see Di Stefano et al, 2017 [15]. Future work will examine how the addition of a tilt between the shock and interface alters multimode interface growth experimentally and in simulations. As the vortex sheet description of single-mode growth yielded insights into both early time and late time growth, it should also be extended to the multimode case. This will require the development of models which accurately capture the deposition of baroclinic vorticity on a multimode, oblique interface by a shock.

The description of vortex sheet evolution used in this dissertation is kinematic, meaning it does not take into account secondary baroclinic vorticity created along the interface. This process occurs whenever the Atwood number is non-zero (i.e. the materials on either side of the interface have differing densities). In the experiments described in Chapters 3 and 4, as well as many applications (ICF in particular), the density contrast across the interface is large. This implies that secondary baroclinic vorticity is likely important to the detailed understanding of hydrodynamic instability growth in these contexts. Future work should utilize dynamical vortex sheet computations, which take secondary baroclinic vorticity into account, to inspect instability growth on oblique interfaces.

The staircase perturbation discussed in Chapter 4 can be used to inspect late time, multimode instability evolution in a different way. Previously, a statistical-vortex-merger model has been used to predict the evolution of the late-time Kelvin-Helmholtz instability, see Rikanat et al., 2003 [64]

and Shimony et al., 2018 [77]. The staircase perturbation can be used to produce a set of asymmetric vortices, without waiting for the linear KH instability to produce them. One can then calibrate the vortex-merger based models for KH growth by observing the vortex merger rate for different vortex distributions.

Appendices

Appendix A

Disagreements between the vorticity deposition model of Chapter 2 and RAGE simulations

The circulation over one wavelength predicted by Eq. 2.21 and that predicted by RAGE simulations differ markedly, by about a factor of two. Furthermore, $\Gamma(\lambda)$ varies strongly as a function of ka in Eq. 2.21, whereas in RAGE simulations $\Gamma(\lambda)$ remains nearly constant between the no-perturbation case and the case with a 100 μm wavelength, 10 μm amplitude sinusoidal perturbation. If the discrepancy were only an overall factor of two, and the dependence on ka were correct, this could be easily remedied by either asserting the factor of two as an ansatz or finding some other justification for it. However, the dependence of $\Gamma(\lambda)$ on ka must also be addressed. I will first discuss a potential problem with the integral for the circulation given in Chapter 2 of this book dealing with the parameterization of the pre-shock interface, and then discuss a potential problem with neglecting the transmitted and reflected waves.

A.1 A potential problem with the density gradient of perturbed interfaces from Chapter 2

The circulation over one wavelength has no dependence on the deformation of the interface according to the assumptions of Chapter 2, so that the interaction between the shock and interface can be the sole matter of inquiry. I will first restate the expressions for the density and density gradients given in Chapter 2. I will then use a method for taking the gradient of a Heaviside step function given in Osher & Fedkiw, 2003 [60] to argue that the density gradient given in Chapter 2 is incorrect. Using the corrected form results in an expression for the circulation over one wavelength which depends only on the mean tilt and wavelength (i.e. is independent of perturbation amplitude, as is indicated by simulation).

In Eq. 2.15, the density and density gradient are given. Repeating, they are given as

$$\rho = \Delta\rho H((-1)(y - y_1(x))) + \rho_L$$
$$\nabla\rho = -\Delta\rho\,\delta((-1)(y - y_1(x)))\hat{n}. \tag{A.1}$$

Note that the contact surface has been implicitly described via the use of a level set (see Chapter 1 of Osher & Fedkiw, 2003 [60]). I.e. the contact surface lies at the points for which the implicit function of the interface,

$$\phi(x, y) = (-1)(y - y_1(x)), \tag{A.2}$$

is equal to zero. The density can then be rewritten as

$$\rho = \Delta\rho H(\phi(x, y)) + \rho_L. \tag{A.3}$$

Utilizing this formalism allows me to apply results given in Osher & Fedkiw, 2003 [60] for taking the gradient of Heaviside step functions. To get the density gradient, I can then take the gradient of Eq. A.3, which yields

$$\nabla\rho = \Delta\rho\nabla H(\phi(x, y)) = \Delta\rho H'(\phi(x, y))\nabla\phi(x, y)$$
$$= \Delta\rho\,\delta(\phi(x, y))\nabla\phi(x, y). \tag{A.4}$$

This gradient will be in the direction of the unit normal to the interface everywhere. The unit normal is given by

$$\hat{n} = \frac{\nabla\phi(x, y)}{|\nabla\phi(x, y)|}. \tag{A.5}$$

This is the unit normal as ϕ is constant along the interface, and its gradient is therefore orthogonal to the interface. As $\nabla\rho$ is in the direction of the interface normal, it's magnitude can be calculated as

$$|\nabla\rho| = \Delta\rho\,\delta(\phi(x, y))\nabla\phi(x, y) \cdot \hat{n}$$
$$= \Delta\rho\,\delta(\phi(x, y))\nabla\phi(x, y) \cdot \frac{\nabla\phi(x, y)}{|\nabla\phi(x, y)|}$$
$$= \Delta\rho\,\delta(\phi(x, y))|\nabla\phi(x, y)|$$
$$= \Delta\rho\,\delta(\phi(x, y))\sqrt{1 + (\frac{dy_1}{dx})^2}. \tag{A.6}$$

In vector form, the density gradient is then

$$\nabla\rho = \Delta\rho\,\delta(\phi(x, y))\sqrt{1 + (\frac{dy_1}{dx}(x))^2}\hat{n}. \tag{A.7}$$

Note that this varies from the density gradient given in Eq. 2.15 by the factor of $\sqrt{1+(\frac{dy_1}{dx})^2}$. This factor accounts for the arc length of the interface, and is equal to the parameterization speed ds/dx. This can be seen as follows.

When parameterized by x, the interface curve is given by

$$\vec{\gamma}(x) = (x, y_1(x)). \tag{A.8}$$

The velocity and speed of this parameterization are given respectively by

$$\vec{\gamma}'(x) = (1, \frac{dy_1}{dx}(x)), \text{ and}$$
$$\frac{ds}{dx} = |\vec{\gamma}'(x)| = \sqrt{1+(\frac{dy_1}{dx}(x))^2}, \tag{A.9}$$

where ds is the differential associated with the arc length s. Note that $s(x) = \int_0^x (ds/dx')dx'$, where s is the arc length of the curve $\vec{\gamma}$ based at $x = 0$.

Rewriting the circulation integral (Eq. 2.12), plugging in the new expression for $\nabla\rho$ from Eq. A.7, and evaluating over t and y yields

$$\begin{aligned}
\Gamma(x) &= \int_{-\infty}^{\infty} dt \int_{-\infty}^{\infty} dy \int_0^x dx' \left[\frac{\nabla\rho \times \nabla p}{\rho^2}\right] \\
&= \frac{\Delta p \Delta \rho}{\bar{\rho}^2} \int_{-\infty}^{\infty} dt \int_{-\infty}^{\infty} dy \int_0^x dx' [\delta(y - y_1(x'))\frac{ds}{dx'}\delta(y - u_s t)\hat{n} \times \hat{y}] \\
&= \frac{\Delta\rho \Delta p}{\bar{\rho}^2} \frac{1}{u_s} \int_0^x dx' [\hat{n} \times \hat{y}(\tau_{x'}(x'))\frac{ds}{dx'}].
\end{aligned} \tag{A.10}$$

Let α be the local tilt of the interface relative to the shock (whereas θ is the mean tilt). This implies that $\hat{n} \times \hat{y} = \sin\alpha$ (See Fig. A.1). The local slope of the interface is dy_1/dx so that $\alpha = \arctan(dy_1/dx)$, which in turn yields

$$\hat{n} \times \hat{y} = \sin\alpha = \frac{\frac{dy_1}{dx}}{\sqrt{1+(\frac{dy_1}{dx})^2}} = \frac{\frac{dy_1}{dx}}{\frac{ds}{dx}}. \tag{A.11}$$
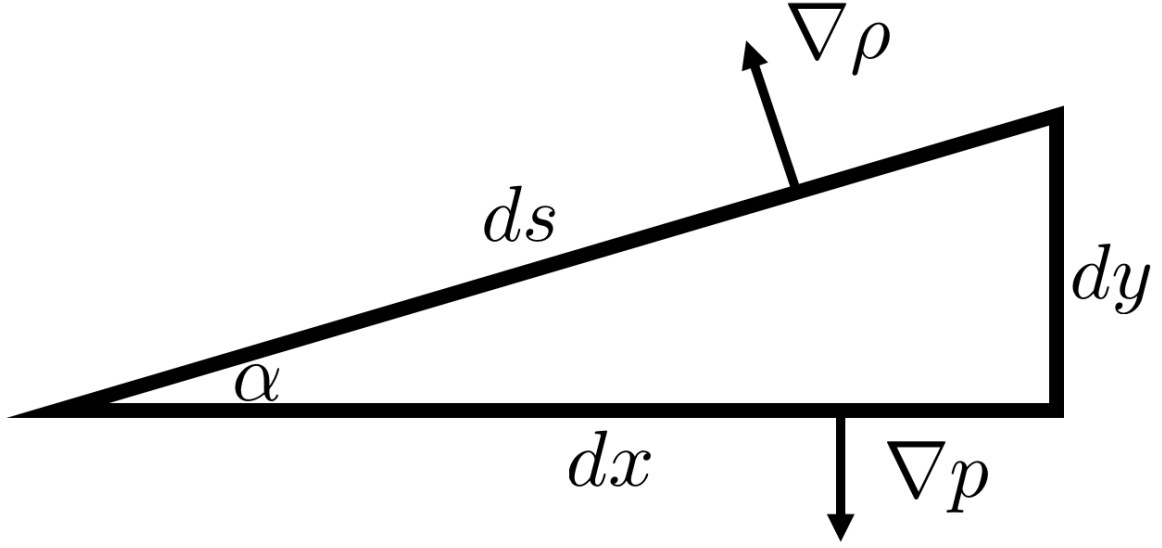
Figure A.1 A diagram showing the relations between dx, dy, and ds for a curve with some local tilt α.

Plugging this into Eq. A.10 gives

$$
\begin{aligned}
\Gamma(x) &= \frac{\Delta\rho\Delta p}{\bar{\rho}^2}\frac{1}{u_s}\int_0^x dx'[\frac{\frac{dy_1}{dx'}}{\frac{ds}{dx'}}\frac{ds}{dx'}] \\
&= \frac{\Delta\rho\Delta p}{\bar{\rho}^2}\frac{1}{u_s}\int_0^x dx'[\frac{dy_1}{dx'}] \\
&= \frac{\Delta\rho\Delta p}{\bar{\rho}^2}\frac{1}{u_s}y_1(x)
\end{aligned} \tag{A.12}
$$

Note that when x is an integer multiple of the perturbation wavelength λ, this expression will have no dependence on the perturbation.

A.2 The importance of transmitted and reflected waves for the deposition of baroclinic vorticity

In Section 2.3 it was assumed that the transmitted and reflected waves contributed negligibly to the deposition of baroclinic vorticity on the interface. The baroclinic source term is $(\nabla p \times \nabla \rho)/\rho^2$, the density jump and average density across the interface are both finite, so that if the baroclinic source associated with a given wave is to be negligible then either 1) the pressure jump across the wave must be small or 2) the density gradient and pressure gradient must be approximately parallel (or

anti-parallel). I leave point 2) unaddressed for now, as even in the case of a centered shock-interface interaction the relative tilts of each of the waves and the interface are a strongly non-linear function of the initial conditions of the problem. To address point 1), consider a centered shock-interface interaction in which the pre-shock materials are isobaric. As the final state of the heavy and light materials must also be isobaric, the total pressure jump in each material must be equivalent. Let ΔP_i be the pressure jump across the incoming shock, ΔP_t be the pressure jump across the transmitted shock, and ΔP_r be the pressure jump across the reflected wave. Note that ΔP_i and ΔP_t are strictly positive, whereas ΔP_r will be negative when the reflected wave is a rarefaction and positive when the reflected wave is a shock. With these definitions, the pressure boundary condition can be rewritten as

$$\Delta P_i + \Delta P_r = \Delta P_t \tag{A.13}$$

Given that ΔP_i is assumed to be finite, if either ΔP_r or ΔP_t is small then the other cannot be. This casts doubt on the method of calculating vorticity deposition proposed in Section 2.3, as at most one of the transmitted or reflected waves can be discounted due to pressure jump magnitude arguments.

Appendix B

Detailed Characterization of the Lawrence-Livermore National Laboratory Imaging Proton Spectrometer

B.1   Introduction

Energetic ion beams are created by ultra-intense laser pulses via a variety of acceleration mechanisms, including target-normal-sheath-acceleration[93] (TNSA) or some type of relativistic transparency[97, 20]. Energetic ion beams have a variety of applications in high energy-density (HED) physics such as iso-choric heating[30], fast ignition[67], and the diagnosing of HED conditions via either radiography[101] or deflectometry[45]. Along with these applications come efforts to better understand beam quality and generation by experimentally characterizing acceleration mechanisms, and the spatial distribution and energy spectra of these beams. Typical diagnostics include radiochromic-film (RCF) stacks[59] and Thomson parabolas. RCF stacks offer 2D imaging but limited energy resolution. Thomson Parabolas offer no spatial imaging but instead employ an electric field to permit species separation.

The LLNL-Imaging Proton Spectrometer (L-IPS) [12] offers an alternative approach. Protons enter the spectrometer via a vertical slit that is parallel to the magnetic field, which disperses the protons in energy in a direction perpendicular to the slit. Thus, the L-IPS keeps one spatial imaging direction, while using the other for high energy resolution. A similar diagnostic is the ISWASP[75], an imaging magnetic spectrometer designed to investigate higher energy ions. Three image plates can be fielded inside the L-IPS, one on each side, and one on the back facing the front end with the entrance slit. Previously published work on the L-IPS discussed the design and early characterization of the diagnostic[12]. This paper expands on earlier work, adding a more complete, 3D description of the L-IPS's magnetic field. The improved magnetic field model, coupled with numerical integration of the proton trajectories, improves the accuracy of the dispersion relation particularly for the low energy portion of the diagnostic and provides new information about the angular dispersion in the imaging direction.
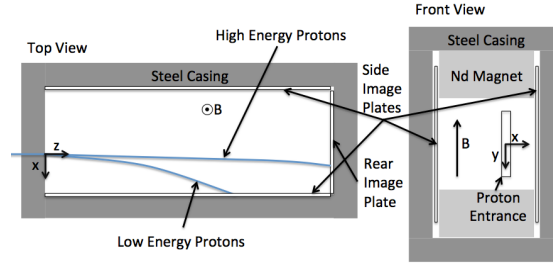
Figure B.1 A schematic of the L-IPS.

B.2 Description of the L-IPS

The L-IPS is a compact spectrometer of dimension 13 cm $\times$ 8.5 cm $\times$ 19 cm, see Figure B.1. The housing of the spectrometer consists of half inch thick steel. One-inch thick Neodymium (Nd) magnets with aligned, vertical magnetizations are located along the top and bottom plates inside the L-IPS. Protons enter the spectrometer through a 1.5 inch high slit, whose width is adjustable to optimize the trade-off between energy resolution and proton fluence. Typically, the spectrometer is fielded with a 50 μm or 100 μm wide slit. The adjustable slit assembly is attached to the front steel plate, which has .26 in $\times$ 1.75 in slot cut into it to allow free passage through the front plate. To provide spatial fiducials in the imaging direction, a thin-wire mesh it typically placed in front of the slit. The wires running perpendicular to slit create shadows in the 2D spectral images. The L-IPS entrance slit typically sits 10-70 cm from the proton source.

Image plates (IP), type BAS-TR[8] are mounted along the back face and 'positive' side, which detects positive ions, of the L-IPS to detect protons. Aluminum filters with appropriate thickness can be used to stop the heavy ions from reaching the IP and to produce proton spectra in specific energy ranges. A third IP, type BAS-MS[8] can be mounted along the other, 'negative', side of L-IPS to record electron or negative ion spectra.

The L-IPS resolves proton velocity space in both energy and angle. For proton generation mechanisms in which the protons approximately originate from a point source (e.g. TNSA) and then propagate ballistically, each proton trajectory can be specified uniquely by the vector (E_{kin}, θ, ϕ). Here, θ and ϕ are taken to be the standard spherical polar angles, with the z-axis aligned with the central axis of the L-IPS. As the entrance slit is vertical and its width is very small compared to distance to the source, the only allowed ϕ values are narrow bands around $\frac{\pi}{2}$ and $-\frac{\pi}{2}$. The trajectory of each allowed proton inside the L-IPS is then uniquely specified by its (E_{kin}, θ) prior to entering the spectrometer. The ability to resolve the θ value of each particle, in addition to its kinetic energy, gives the L-IPS its 1D imaging capability.
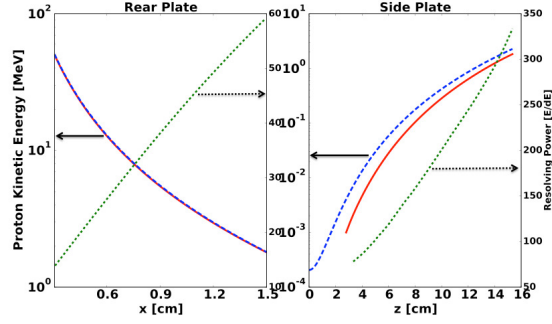
Figure B.2 The dispersion relation in the mid-plane ($y = 0$) calculated using the 3D magnetic field model (solid) is compared to the previous one based on a 2D model scaled to experiment (dashed). The resolving power of the diagnostic is plotted as well (dotted). See text.

B.3   Calculation of the Dispersion Relations

In order to calculate the dispersion relations, the magnetic field of the L-IPS must first be calculated. The magnetic field is then used to numerically integrate the Lorentz equations assuming that the protons propagate ballistically from a point source to the entrance of the spectrometer. This yields particle trajectories which are then used to determine where protons of a given (E_{kin}, θ) intersect with the side or rear image plates. The 3D finite element analysis software ANSYS® Maxwell® was used to calculate the magnetic field of the L-IPS. A CAD model of the L-IPS was made using tools available within ANSYS® Maxwell®. The bulk structure of the L-IPS is well represented, i.e. the outer casing, magnets, and entrance hole. The Nd magnets are modeled using a linear B-H curve, i.e. a constant magnetic permeability is assumed. Two parameters are then needed to specify the strength of the magnets: the magnetic permeability μ and the coercivity H_c. The two magnets are assumed to have identical, uniform, magnetic permeability and coercivity. The magnetic field strength in the calculation is tuned by altering the coercivity. The B-H curve provided by ANSYS® Maxwell® is used to model the magnetic properties of the steel casing.

Particle trajectories must be numerically integrated[36, 29] inside of the L-IPS in order to find the dispersion relations. The relevant equation is the relativistic Lorentz equation:

$$\frac{d\vec{x}}{dt} = \vec{v}, \quad \frac{d\vec{v}}{dt} = q(\frac{\vec{v}}{m\gamma} \times \vec{B}). \tag{B.1}$$

The initial boundary conditions were specified using (E_{kin}, θ), and the distance between the source and spectrometer entrance. The intersections of the proton trajectories with the image plates were then calculated, which, in turn, were used to obtain the dispersion relations, e.g $E(x, y)$ and $\theta(x, y)$ for the rear image plate.

In order to calibrate the calculated dispersion relations, we used experimental spectra taken with rear IPs covered with thin Al foils acting as range filters. Four different Al foils with thickness

between 48.5 μm and 254 μm were used on separate target shots. As the angles of incidence on the rear IP and range filters are near normal, the energy dependent stopping power and range data for a given filter can be used to reliably calibrate the energy corresponding to the low-energy cut-off observed in the proton spectrum. With this calibration procedure, the 3D model of the magnetic field, coupled with the proton trajectory calculations, provides significantly improved dispersion relation, particularly for the low energy part of the spectrum (below 1.8 MeV) on the side IP.

B.4 Results

Figure B.2 shows the energy dispersion relation calculated with the 3D model (solid line), using the above-mentioned calibration procedure, for the mid-plane ($y = 0$) of the L-IPS. The low- and high-energy parts, corresponding to the side and rear image plates, are plotted separately. The dispersion curves obtained previously using a 2D model of the B-field calibrated with range filters on the image plates [12] are shown for comparison (dashed line). The resolving power (E/dE) of the diagnostic is plotted as well (dotted line). The agreement for the rear image plate is excellent. However, for the side image plate, there is significant disagreement over the entire energy range. We attribute this primarily to the incorrect calibration of the earlier 2D model of the B-field using the 9 μm coating present on the BAS-MS IP as a range-filter for the low-energy proton spectrum. On the side, the protons are incident on the IP, and any filter covering it, at a very shallow angle, which decreases with increasing energy. As result, small-angle scattering of the protons in the range-filter has a large effect on the breakthrough energy inferred from the range taken equal to filter thickness/$\sin \alpha$, where α is the angle of incidence.

Figure B.3a shows an experimentally obtained spectral image on the rear image plate produced by TNSA protons from Au-coated Si foil target irradiated by the Titan laser at LLNL[86]. Part of the image plate was covered with 48.5 μm thick Al filter, which produces a cutoff at 2.2 MeV. In the image, this cutoff appears curved as a function of y, because the B-field is stronger near the magnets on top and bottom than in the middle, and therefore protons with a fixed energy are deflected from the entrance slit more near the magnets. The energy spectrum exhibits some quasi-periodic modulations[74] (see Figure B.3c), which appear to be independent of incoming angle (θ) over the limited angular range of the L-IPS. These modulations get shifted along x as a function of y due to the B-field variation in y and provide energy banding in the image that enables precision energy response characterization of the L-IPS off axis. Figure B.3b compares the experimental locations of these iso-contours at selected values of y (shown as blue dots) to those calculated from the 3D model (shown as red lines). The agreement is satisfactory, which indicates that the 3D model is giving sufficiently accurate dispersion relations away from the mid-plane of the spectrometer.
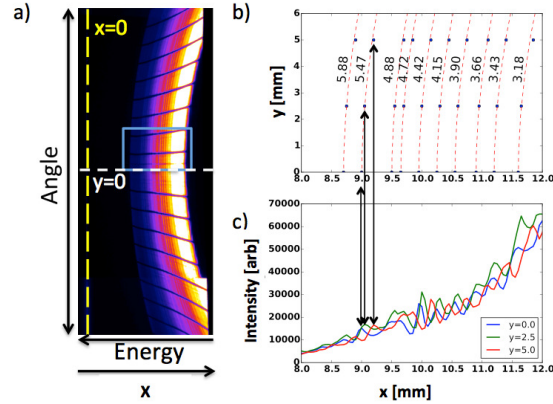
Figure B.3 (a) Experimentally obtained spectral image from the rear image plate. The yellow dashed line shows the image of the slit due to X-rays and/or neutrals. (b) Iso-energy contours from calculation (red dashed line) and loci from experimental iso-energy contours (blue dots) are plotted on the rear image plate. The energy of each contour is written in MeV. (c) shows the lineouts from which the experimental iso-energy loci were extracted. Lineouts were taken at three vertical locations, the locations of the peaks in the lineouts then give the co-ordinates of points along the experimental iso-energy contours. The vertical lines between b) and c) show which peaks correspond to which experimental loci for the 5.47 MeV contour. Only the upper half of the contours are plotted in b) as both the B field and iso-contours are highly symmetric. The region plotted in b) corresponds to the blue box in a).

B.5   Conclusion

We have computed the 3D magnetic field of the L-IPS and used this to calculate the dispersion relation of the instrument. This work has both improved the calibration of the diagnostic on-axis and given the first calculation of the off-axis dispersion relation.

Bibliography

[1] R. J. ADRIAN, *Twenty years of particle image velocimetry*, Exp. Fluids, 39 (2005), pp. 159–169.

[2] B. AKULA, M. J. ANDREWS, AND D. RANJAN, *Effect of shear on Rayleigh-Taylor mixing at small Atwood number*, Physical Review E, 87 (2013), pp. 1–14.

[3] D. ARNETT, B. FRYXELL, AND E. MULLER, *Instabilities and nonradial motion in SN 1987A*, ApJ, 341 (1989), pp. L63—-L66.

[4] W. D. ARNETT, J. N. BAHCALL, R. P. KIRSHNER, AND S. E. WOOSLEY, *SUPERNOVA 1987A*, Annu. Rev. Astron. Astrophysics, 27 (1989), pp. 629–700.

[5] S. ATZENI AND J. MEYER-TER-VEHN, *The Physics of Inertial Fusion*, Oxford University Press, 2004.

[6] B. J. BALAKUMAR, G. C. ORLICZ, C. D. TOMKINS, AND K. P. PRESTRIDGE, *Simultaneous particle-image velocimetry-planar laser-induced fluorescence measurements of Richtmyer-Meshkov instability growth in a gas curtain with and without reshock*, Physics of Fluids, 20 (2008).

[7] W. BLEAKNEY, D. K. WEIMER, AND C. H. FLETCHER, *The Shock Tube : A Facility for Investigations in Fluid Dynamics*, Rev. Sci. Instrum., 20 (1949), pp. 807–815.

[8] T. BONNET, M. COMET, D. DENIS-PETIT, F. GOBET, F. HANNACHI, M. TARISIEN, M. VERSTEEGEN, AND M. M. ALEONARD, *Response functions of Fuji imaging plates to monoenergetic protons in the energy range 0.6-3.2 MeV*, Review of Scientific Instruments, 84 (2013), pp. 0–6.

[9] M. BROUILLETTE, *The Richtmyer-Meshkov Instability*, Ann. Rev. Fluid Mech., 34 (2002), pp. 445–468.

[10] G. L. BROWN AND A. ROSHKO, *On density effects and large structure in turbulent mixing layers*, J. Fluid Mech., 64 (1974), pp. 775–816.

[11] C. J. CHAPMAN, *High Speed Flow*, Cambridge University Press, 2000.

[12] H. CHEN, A. U. HAZI, R. VAN MAREN, S. N. CHEN, J. FUCHS, M. GAUTHIER, S. LE PAPE, J. R. RYGG, AND R. SHEPHERD, *An imaging proton spectrometer for short-pulse laser plasma experiments*, Review of Scientific Instruments, 81 (2010), p. 10D314.

[13] C. A. DI STEFANO, G. MALAMUD, M. T. HENRY DE FRAHAN, C. C. KURANZ, A. SHIMONY, S. R. KLEIN, R. P. DRAKE, E. JOHNSEN, D. SHVARTS, V. A. SMALYUK, AND D. MARTINEZ, *Observation and modeling of mixing-layer development in high-energy-density, blast-wave-driven shear flow*, Physics of Plasmas, 24 (2014).

[14] C. A. DI STEFANO, G. MALAMUD, C. C. KURANZ, S. R. KLEIN, R. P. DRAKE, AND L. ALAMOS, *Measurement of Richtmyer – Meshkov mode coupling under steady shock conditions and at high energy density*, High Energy Density Physics, 17 (2015), pp. 263–269.

[15] C. A. DI STEFANO, G. MALAMUD, C. C. KURANZ, S. R. KLEIN, C. STOECKL, AND R. P. DRAKE, *Richtmyer-Meshkov evolution under steady shock conditions in the high-energy-density regime*, Applied Physics Letters, 106 (2015).

[16] C. A. DI STEFANO, A. M. RASMUS, F. W. DOSS, K. A. FLIPPO, J. D. HAGER, J. L. KLINE, AND P. A. BRADLEY, *Multimode instability evolution driven by strong, high-energy-density shocks in a rarefaction-reflected geometry*, Phys. Plasmas, 24 (2017), p. 52101.

[17] G. DIMONTE, C. E. FRERKING, M. SCHNEIDER, AND B. REMINGTON, *Richtmyer–Meshkov instability with strong radiatively driven shocks*, Physics of Plasmas, 3 (1996), p. 614.

[18] G. DIMONTE AND B. REMINGTON, *Richtmyer-Meshkov experiments on the Nova laser at high compression*, Phys. Rev. Lett., 70 (1993), p. 1806.

[19] R. P. DRAKE, *High-Energy-Density Physics*, Springer, 1st ed., 2006.

[20] R. P. DRAKE, *High-Energy-Density Physics*, Springer International Publishing, 2nd ed., 2018.

[21] T. ESIRKEPOV, M. BORGHESI, S. V. BULANOV, G. MOUROU, AND T. TAJIMA, *Highly efficient relativistic-ion generation in the laser-piston regime*, Physical Review Letters, 92 (2004), pp. 175003–1.

[22] M. GEISSEL, C. COX, M. SCHOLLMEIER, J. E. SHORES, I. C. SMITH, C. S. SPEAS, AND J. L. PORTER, *Optimization of X-Ray Backlighting for Experiments on Z*, in 2013 19th IEEE Pulsed Power Conference (PPC), 2013, pp. 1380–1383.

[23] M. GITTINGS, R. WEAVER, M. CLOVER, T. BETLACH, N. BYRNE, R. COKER, E. DENDY, R. HUECKSTAEDT, K. NEW, W. R. OAKES, D. RANTA, AND R. STEFAN, *The RAGE radiation-hydrodynamic code*, Computational Science and Discovery, 1 (2008).

[24] S. G. GLENDINNING, J. BOLSTAD, D. G. BRAUN, M. J. EDWARDS, W. W. HSING, B. F. LASINSKI, H. LOUIS, A. MILES, J. MORENO, T. A. PEYSER, B. A. REMINGTON, H. F. ROBEY, E. J. TURANO, C. P. VERDON, AND Y. ZHOU, *Effect of shock proximity on Richtmyer-Meshkov growth*, Phys. Plasmas, 10 (2003), pp. 1931–1936.

[25] V. N. GONCHAROV, *Analytical model of nonlinear, single-mode, classical Rayleigh-Taylor instability at arbitrary Atwood numbers.*, Physical review letters, 88 (2002), p. 134502.

[26] S. W. HAAN, J. D. LINDL, D. A. CALLAHAN, D. S. CLARK, J. D. SALMONSON, B. A. HAMMEL, L. J. ATHERTON, R. C. COOK, M. J. EDWARDS, S. GLENZER, A. V. HAMZA, S. P. HATCHETT, M. C. HERRMANN, D. E. HINKEL, D. D. HO, H. HUANG, O. S. JONES, J. KLINE, G. KYRALA, O. L. LANDEN, B. J. MACGOWAN, M. M. MARINAK, D. D. MEYERHOFER, J. L. MILOVICH, K. A. MORENO, E. I. MOSES, D. H. MUNRO, A. NIKROO, R. E. OLSON, K. PETERSON, S. M. POLLAINE, J. E. RALPH, H. F. ROBEY, B. K. SPEARS, P. T. SPRINGER, L. J. SUTER, C. A. THOMAS, R. P. TOWN, R. VESEY, S. V. WEBER, H. L. WILKENS, AND D. C. WILSON, *Point design targets, specifications,*

and requirements for the 2010 ignition campaign on the National Ignition Facility, Physics of Plasmas, 18 (2011), p. 51001.

[27] E. C. HARDING, J. F. HANSEN, O. A. HURRICANE, R. P. DRAKE, H. F. ROBEY, C. C. KURANZ, B. A. REMINGTON, M. J. BONO, M. J. GROSSKOPF, AND R. S. GILLESPIE, *Observation of a Kelvin-Helmholtz Instability in a High-Energy-Density Plasma on the Omega Laser*, Physical Review Letters, 103 (2009), pp. 1–4.

[28] B. M. HEGELICH, B. J. ALBRIGHT, J. COBBLE, K. FLIPPO, S. LETZRING, M. PAFFETT, H. RUHL, J. SCHREIBER, R. K. SCHULZE, AND J. C. FERNÁNDEZ, *Laser acceleration of quasi-monoenergetic MeV ion beams.*, Nature, 439 (2006), pp. 441–444.

[29] H. HELMHOLTZ, *Über discontinuierliche flüssigkeits-bewengungen (on the discontinuous movements of fluids)*, Philos. Mag. (1798-1977), 36 (1868), p. 337.

[30] A. HINDMARSH, *ODEPACK, A Systematized Collection of ODE Solvers*, IMACS Transactions on Scientific Computation, 1 (1983), pp. 55–64.

[31] D. H. H. HOFFMANN, V. E. FORTOV, I. V. LOMONOSOV, V. MINTSEV, N. A. TAHIR, D. VARENTSOV, AND J. WIESER, *Unique capabilities of an intense heavy ion beam as a tool for equation-of-state studies*, Physics of Plasmas, 9 (2002), p. 3651.

[32] R. L. HOLMES, G. DIMONTE, B. FRYXELL, M. L. GITTINGS, J. W. GROVE, M. SCHNEIDER, D. H. SHARP, A. L. VELIKOVICH, R. P. WEAVER, AND Q. ZHANG, *Richtmyer–Meshkov instability growth: experiment, simulation and theory*, J. Fluid Mech., 389 (1999), pp. 55–79.

[33] O. A. HURRICANE, *Design for a high energy density Kelvin–Helmholtz experiment*, High Energy Density Physics, 4 (2008), pp. 97–102.

[34] O. A. HURRICANE, E. BURKE, S. MAPLES, AND M. VISWANATHAN, *Saturation of Richtmyer's impulsive model*, Phys. Fluids, 12 (2000), pp. 2148–2151.

[35] O. A. HURRICANE, V. A. SMALYUK, K. RAMAN, O. SCHILLING, J. F. HANSEN, G. LANGSTAFF, D. MARTINEZ, H. S. PARK, B. A. REMINGTON, H. F. ROBEY, J. A. GREENOUGH, R. WALLACE, C. A. DI STEFANO, R. P. DRAKE, D. MARION, C. M. KRAULAND, AND C. C. KURANZ, *Validation of a Turbulent Kelvin-Helmholtz Shear Layer Model Using a High-Energy-Density OMEGA Laser Experiment*, Phys. Rev. Lett., 109 (2012).

[36] J. W. JACOBS AND V. V. KRIVETS, *Experiments on the late-time development of single-mode Richtmyer – Meshkov instability*, Phys. Fluids, 17 (2005).

[37] E. JONES, T. OLIPHANT, P. PETERSON, AND OTHERS, *SciPy: Open source scientific tools for Python*.

[38] M. H. KEY, W. T. TONER, T. J. GOLDSACK, J. D. KILKENNY, S. A. VEATS, P. F. CUNNINGHAM, AND C. L. S. LEWIS, *A study of ablation by laser irradiation of plane targets at wavelengths 1.05, 0.53, and 0.35 \textmu\ m*, Phys. Fluids, 26 (1983).

[39] R. KRASNY, *Desingularization of periodic vortex sheet roll-up*, Journal of Computational Physics, 65 (1986), pp. 292–313.

[40] R. KRASNY, *Vortex Sheet Computations: Roll-Up, Wakes, Separation*, Lect. Appl. Math., 28 (1991), pp. 385–401.

[41] C. C. KURANZ, R. P. DRAKE, M. J. GROSSKOPF, A. BUDDE, C. KRAULAND, D. C. MARION, A. J. VISCO, J. R. DITMAR, F. ROBEY, B. A. REMINGTON, A. R. MILES, A. B. R. COOPER, C. SORCE, T. PLEWA, N. C. HEARN, K. L. KILLEBREW, D. ARNETT, AND T. DONAJKOWSKI, *Three-dimensional blast-wave-driven Rayleigh – Taylor instability and the effects of long-wavelength modes*, Phys. Plasmas, 16 (2009).

[42] C. C. KURANZ, R. P. DRAKE, E. C. HARDING, M. J. GROSSKOPF, B. A. REMINGTON, AND M. J. EDWARDS, *TWO DIMENSIONAL BLAST-WAVE-DRIVEN RAYLEIGH-TAYLOR INSTABILITY: EXPERIMENT AND SIMULATION*, The Astrophysical Journal, 696 (2009), pp. 749–759.

[43] C. C. KURANZ, H. PARK, C. M. HUNTINGTON, A. R. MILES, B. A. REMINGTON, T. PLEWA, M. R. TRANTHAM, H. F. ROBEY, D. SHVARTS, A. SHIMONY, K. RAMAN, S. MACLAREN, W. C. WAN, F. W. DOSS, J. KLINE, K. A. FLIPPO, G. MALAMUD, T. A. HANDY, S. PRISBREY, C. M. KRAULAND, S. R. KLEIN, E. C. HARDING, R. WALLACE, M. J. GROSSKOPF, D. C. MARION, D. KALANTAR, E. GIRALDEZ, AND R. P. DRAKE, *How high energy fluxes may affect Rayleigh-Taylor instability growth in young supernova remnants*, Nature Communications, 9 (2018).

[44] L. D. LANDAU AND E. M. LIFSHITZ, *Fluid Mechanics*, Butterworth-Heinemann, 2nd ed., 1987.

[45] J. T. LARSEN AND S. M. LANE, *HYADES-A plasma hydrodynamics code for dense plasma studies*, Journal of Quantitative Spectroscopy and Radiative Transfer, 51 (1994), pp. 179–186.

[46] M. C. LEVY, D. D. RYUTOV, S. C. WILKS, J. S. ROSS, C. M. HUNTINGTON, F. FIUZA, D. A. MARTINEZ, N. L. KUGLAND, M. G. BARING, AND H. S. PARK, *Development of an interpretive simulation tool for the proton radiography technique*, Review of Scientific Instruments, 86 (2015).

[47] J. LINDL, O. LANDEN, J. EDWARDS, AND E. MOSES, *Review of the national ignition campaign 2009-2012*, Physics of Plasmas, 21 (2014).

[48] J. D. LINDL, *Inertial Confinement Fusion*, Springer, 1998.

[49] S. P. LYON AND J. D. JOHNSON, *SESAME: The Los Alamos National Laboratory equation of state database*, Technical Report No. LA-UR-92-3407, Los Alamos National Laboratory, (1992).

[50] T. MA, E. BOND, D. K. BRADLEY, J. CAGGIANO, D. A. CALLAHAN, D. T. CASEY, P. M. CELLIERS, C. J. CERJAN, J. A. CHURCH, D. N. FITTINGHOFF, J. A. FRENJE, M. G. JOHNSON, S. GLENN, S. H. GLENZER, G. GRIM, N. GULER, S. W. HAAN, B. A.

HAMMEL, R. HATARIK, H. W. HERRMANN, D. HICKS, D. E. HINKEL, L. F. B. HOPKINS, W. W. HSING, P. REGAN, B. A. REMINGTON, H. F. ROBEY, M. D. ROSEN, J. R. RYGG, J. S. ROSS, J. D. SALMONSON, AND J. SATER, *The role of hot spot mix in the low-foot and high-foot implosions on the NIF*, 056311 (2017).

[51] T. MA, P. K. PATEL, N. IZUMI, P. T. SPRINGER, M. H. KEY, L. J. ATHERTON, L. R. BENEDETTI, D. K. BRADLEY, D. H. EDGELL, J. D. KILKENNY, J. L. KLINE, G. A. KYRALA, O. L. LANDEN, S. L. PAPE, B. J. MACGOWAN, A. J. MACKINNON, A. G. MACPHEE, N. B. MEEZAN, J. D. MOODY, A. PAK, T. PARHAM, H.-S. PARK, J. E. RALPH, S. P. REGAN, B. A. REMINGTON, H. F. ROBEY, J. S. ROSS, B. K. SPEARS, V. SMALYUK, L. J. SUTER, R. TOMMASINI, R. P. TOWN, S. V. WEBER, J. D. LINDL, M. J. EDWARDS, S. H. GLENZER, AND E. I. MOSES, *Onset of Hydrodynamic Mix in High-Velocity , Highly Compressed Inertial Confinement Fusion Implosions*, Phys. Rev. Lett., 111 (2013), p. 085004.

[52] G. MALAMUD, C. A. DI STEFANO, Y. ELBAZ, C. M. HUNTINGTON, C. C. KURANZ, P. A. KEITER, AND R. P. DRAKE, *A design of a two-dimensional, multimode RM experiment on OMEGA-EP*, HEDP, 9 (2013), pp. 122–131.

[53] G. MALAMUD, A. SHIMONY, W. C. WAN, C. A. D. STEFANO, Y. ELBAZ, C. C. KURANZ, P. A. KEITER, R. P. DRAKE, AND D. SHVARTS, *High Energy Density Physics A design of a two-dimensional , supersonic KH experiment on OMEGA-EP*, HEDP, 9 (2013), pp. 672–686.

[54] C. MATSUOKA, *Nonlinear behavior of a vortex sheet in incompressible Richtmyer – Meshkov instability with surface tension*, Phys. Scr., 2008 (2008).

[55] J. MCFARLAND, D. REILLY, S. CREEL, C. MCDONALD, AND T. FINN, *Experimental investigation of the inclined interface Richtmyer – Meshkov instability before and after reshock*, Exp. Fluids, 55 (2014), p. 1640.

[56] E. E. MESHKOV, *Instability of the interface of two gases accelerated by a shock wave*, Sov. Fluid Dynamics, 4 (1969), pp. 151–157.

[57] E. E. MESHKOV, *Instability of the interface of two gases accelerated by a shock wave*, Fluid Dynamics, 4 (1972), pp. 101–104.

[58] K. A. MEYER, *Numerical Investigation of the Stability of a Shock-Accelerated Interface between Two Fluids*, Physics of Fluids, 15 (1972), p. 753.

[59] K. O. MIKAELIAN, *Oblique shocks and the combined Rayleigh-Taylor, Kelvin-Helmholtz, and Richtmyer-Meshkov instabilities*, Phys. Fluids, 6 (1994), p. 1943.

[60] F. NÜRNBERG, M. SCHOLLMEIER, E. BRAMBRINK, A. BLAŽEVIĆ, D. C. CARROLL, K. FLIPPO, D. C. GAUTIER, M. GEIBEL, K. HARRES, B. M. HEGELICH, O. LUNDH, K. MARKEY, P. MCKENNA, D. NEELY, J. SCHREIBER, AND M. ROTH, *Radiochromic film imaging spectroscopy of laser-accelerated proton beams*, Review of Scientific Instruments, 80 (2009), pp. 1–13.

[61] S. OSHER AND R. FEDKIW, *Level Set Methods and Dynamic Implicit Surfaces*, vol. 57, Springer-Verlag New York Inc, 2003.

[62] H. PARK, D. M. CHAMBERS, H. K. CHUNG, R. J. CLARKE, R. EAGLETON, E. GIRALDEZ, T. GOLDSACK, R. HEATHCOTE, N. IZUMI, M. H. KEY, J. A. KING, J. A. KOCH, O. L. LANDEN, A. NIKROO, P. K. PATEL, D. F. PRICE, B. A. REMINGTON, H. F. ROBEY, R. A. SNAVELY, D. A. STEINMAN, R. B. STEPHENS, C. STOECKL, M. STORM, M. TABAK, W. THEOBALD, R. P. J. TOWN, J. E. WICKERSHAM, AND B. B. ZHANG, *High-energy K-alpha radiography using high-intensity, short-pulse lasers*, Phys. Plasmas, 13 (2006).

[63] D. REILLY, J. MCFARLAND, M. MOHAGHAR, AND D. RANJAN, *The effects of initial conditions and circulation deposition on the inclined - interface reshocked Richtmyer – Meshkov instability*, Exp. Fluids, 56 (2015), p. 168.

[64] R. D. RICHTMYER, *Taylor instability in shock acceleration of compressible fluids*, Communications on Pure and Applied Mathematics, 13 (1960), pp. 297–319.

[65] A. RIKANATI, U. ALON, AND D. SHVARTS, *Vortex-merger statistical-mechanics model for the late time self-similar evolution of the Kelvin – Helmholtz instability*, Phys. Fluids, 15 (2003), p. 3776.

[66] A. RIKANATI, U. ALON, AND D. SHVARTZ, *Vortex model for the nonlinear evolution of the multimode Richtmyer-Meshkov instability at low Atwood numbers*, Phys. Rev. E, 58 (1998), pp. 7410–7418.

[67] H. F. ROBEY, *Effects of viscosity and mass diffusion in hydrodynamically unstable plasma flows*, Physics of Plasmas, 11 (2004), pp. 4123–4133.

[68] M. ROTH, T. E. COWAN, M. H. KEY, S. P. HATCHETT, C. BROWN, W. FOUNTAIN, J. JOHNSON, D. M. PENNINGTON, R. A. SNAVELY, S. C. WILKS, K. YASUIKE, H. RUHL, F. PEGORARO, S. V. BULANOV, E. M. CAMPBELL, M. D. PERRY, AND H. POWELL, *Fast ignition by intense laser-accelerated proton beams*, Physical Review Letters, 86 (2001), pp. 436–439.

[69] D. D. RYUTOV, R. P. DRAKE, J. KANE, E. LIANG, B. A. REMINGTON, AND W. M. WOOD-VASEY, *Similarity Criteria for the laboratory simulation of supernova hydrodynamics*, Astrophysical Journal, 518 (1999), pp. 821–832.

[70] D. D. RYUTOV, R. P. DRAKE, AND B. A. REMINGTON, *Criteria for Scaled Laboratory Simulations of Astrophysical MHD Phenomena*, The Astrophysical Journal Supplement Series, 127 (2000), pp. 465–468.

[71] D. D. RYUTOV, B. A. REMINGTON, H. F. ROBEY, AND R. P. DRAKE, *Magnetohydrodynamic scaling: From astrophysics to the laboratory*, Physics of Plasmas, 8 (2001), pp. 1804–1816.

[72] O. SADOT, L. EREZ, U. ALON, D. ORON, L. LEVIN, G. EREZ, G. BEN-DOR, AND D. SHVARTS, *Study of Nonlinear Evolution of Single-Mode and Two-Bubble Interaction under Richtmyer-Meshkov Instability*, Physical Review Letters, 80 (1998), pp. 1654–1657.

[73] R. SAMTANEY, J. RAY, AND N. J. ZABUSKY, *Baroclinic circulation generation on shock accelerated slow/fast gas interfaces*, Physics of Fluids, 10 (1998), pp. 1217–1230.

[74] R. SAMTANEY AND N. J. ZABUSKY, *Circulation Deposition on Shock-Accelerated Planar and Curved Density-Stratified Interfaces: Models and Scaling Laws*, Journal of Fluid Mechanics, 269 (1994), pp. 45–78.

[75] M. SCHNÜRER AND A. A. ANDREEV, *The beat in laser-accelerated ion beams*, Physics of Plasmas, (2013), pp. 0–5.

[76] L. SENJE, M. YEUNG, B. AURAND, S. KUSCHEL, C. RODEL, F. WAGNER, K. LI, B. DROMEY, V. BAGNOUD, P. NEUMAYER, M. ROTH, C. G. WAHLSTROM, M. ZEPF, T. KUEHL, AND D. JUNG, *Diagnostics for studies of novel laser ion acceleration mechanisms*, Review of Scientific Instruments, 85 (2014).

[77] A. SHIMONY, D. SHVARTS, G. MALAMUD, C. DI STEFANO, C. KURANZ, AND R. DRAKE, *The Effect of a Dominant Initial Single Mode on the Kelvin-Helmholtz Instability Evolution: New Insights on Previous Experimental Results*, Journal of Fluids Engineering, Transactions of the ASME, 138 (2016), pp. 1–7.

[78] A. SHIMONY, W. WAN, C. KURANZ, R. DRAKE, D. SHARTS, AND G. MALAMUD, *Construction and validation of a statistical model for the nonlinear Kelvin-Helmholtz instability under compressible , multimode conditions*, Physics of Plasmas, 25 (2018).

[79] V. A. SMALYUK, J. F. HANSEN, O. A. HURRICANE, G. LANGSTAFF, D. MARTINEZ, H. S. PARK, K. RAMAN, B. REMINGTON, H. F. ROBEY, O. SCHILLING, R. WALLACE, Y. ELBAZ, A. SHIMONY, D. SHVARTS, C. D. STEFANO, R. P. DRAKE, D. MARION, C. M. KRAULAND, AND C. C. KURANZ, *Experimental observations of turbulent mixing due to Kelvin – Helmholtz instability on the OMEGA Laser Facility*, Phys. Plasmas, 19 (2012).

[80] V. A. SMALYUK, O. A. HURRICANE, J. F. HANSEN, G. LANGSTAFF, D. MARTINEZ, H. S. PARK, K. RAMAN, B. A. REMINGTON, H. F. ROBEY, O. SCHILLING, R. WALLACE, Y. ELBAZ, A. SHIMONY, D. SHVARTS, C. D. STEFANO, R. P. DRAKE, D. MARION, C. M. KRAULAND, AND C. C. KURANZ, *Measurements of turbulent mixing due to Kelvin-Helmholtz instability in high-energy-density plasmas*, High Energy Density Physics, 9 (2013), pp. 47–51.

[81] S.-I. SOHN, *Vortex model and simulations for Rayleigh-Taylor and Richtmyer-Meshkov instabilities*, Phys. Rev. E, 69 (2004), pp. 1–11.

[82] S.-I. SOHN, *Late-time vortex dynamics of Rayleigh-Taylor instability*, Journal of the Physical Society of Japan, 80 (2011), pp. 1–7.

[83] S.-I. SOHN, D. YOON, AND W. HWANG, *Long-time simulations of the Kelvin-Helmholtz instability using an adaptive vortex method*, Phys. Rev. E, 82 (2010), pp. 1–10.

[84] C. STOECKL, G. FIKSEL, D. GUY, C. MILEHAM, P. M. NILSON, T. C. SANGSTER, M. J. SHOUP, AND W. THEOBALD, *A spherical crystal imager for OMEGA EP*, Rev. Sci. Instrum., 83 (2012), p. 33107.

[85] J. W. STRUTT (LORD RAYLEIGH), *Investigation of the character of the equilibrium of an incompressible heavy fluid of variable density*, Proc. London Math. Soc., s1-s14 (1882), pp. 170–177.

[86] B. C. STUART, J. D. BONLIE, J. A. BRITTEN, J. A. CAIRD, R. CROSS, C. A. EBBERS, M. J. ECKART, A. C. ERLANDSON, W. A. MOLANDER, A. NG, P. K. PATEL, AND D. F. PRICE, *The Titan Laser at LLNL - Technical Digest (CD)*, in Conference on Lasers and Electro-Optics/Quantum Electronics and Laser Science Conference and Photonic Applications Systems Technologies, Optical Society of America, 2006, p. JTuG3.

[87] G. TAYLOR, *The Instability of Liquid Surfaces when Accelerated in a Direction Perpendicular to their Planes*, Proceedings of the Royal Society of London A: Mathematical, Physical, and Engineering Sciences, 201 (1950), pp. 192—-196.

[88] W. THOMSON, *Hydrokinetic solutions*, The London, Edinburgh, and Dublin Philosophical Magazine and Journal of Science, 42 (1871), pp. 362—-377.

[89] R. B. TULLY, H. COURTOIS, Y. HOFFMAN, AND D. POMAREDE, *The Laniakea supercluster of galaxies*, Nature, 513 (2014), pp. 71–73.

[90] W. C. WAN, G. MALAMUD, A. SHIMONY, C. A. DI STEFANO, M. R. TRANTHAM, S. R. KLEIN, D. SHVARTS, C. C. KURANZ, AND R. P. DRAKE, *Observation of Single-Mode, Kelvin-Helmholtz Instability in a Supersonic Flow*, Physical Review Letters, 115 (2015), pp. 1–6.

[91] W. C. WAN, G. MALAMUD, A. SHIMONY, C. A. D. STEFANO, M. R. TRANTHAM, S. R. KLEIN, D. SHVARTS, R. P. DRAKE, AND C. C. KURANZ, *Observation of dual-mode , Kelvin-Helmholtz instability vortex merger in a compressible flow*, Phys. Plasmas, 24 (2017), p. 055705.

[92] L. WAXER, D. MAYWAR, J. KELLY, T. KESSLER, B. KRUSCHWITZ, S. LOUCKS, R. MC-CRORY, D. MEYERHOFER, S. MORSE, C. STOECKL, AND J. ZUEGEL, *High-Energy Petawatt Capability for the Omega Laser*, Optics and Photonics News, 16 (2005), p. 30.

[93] S. C. WILKS, A. B. LANGDON, T. E. COWAN, M. ROTH, M. SINGH, S. HATCHETT, M. H. KEY, D. PENNINGTON, A. MACKINNON, AND R. A. SNAVELY, *Energetic proton generation in ultra-intense laser–solid interactions*, Physics of Plasmas, 8 (2001), p. 542.

[94] J. G. WOUCHUK, *Growth rate of the linear Richtmyer-Meshkov instability when a shock is reflected*, Phys. Rev. E, 63 (2001), pp. 1–13.

[95] J. G. WOUCHUK, *Growth rate of the Richtmyer-Meshkov instability when a rarefaction is reflected*, Physics of Plasmas, 8 (2001), pp. 2890–2907.

[96] J. G. WOUCHUK AND F. COBOS-CAMPOS, *Linear theory of Richtmyer – Meshkov like flows*, Plasma Phys. Control. Fuso, 59 (2017).

[97] L. YIN, B. J. ALBRIGHT, B. M. HEGELICH, K. J. BOWERS, K. A. FLIPPO, T. J. T. KWAN, AND J. C. FERNANDEZ, *Monoenergetic and GeV ion acceleration from the laser breakout afterburner using ultrathin targets*, Physics of Plasmas, 14 (2007).

[98] N. J. ZABUSKY, *Vortex Paradigm for Accelerated Inhomgeneous Flows: Visiometrics for the Rayleigh-Taylor and Richtmyer-Meshkov Environments*, Annual Review of Fluid Mechanics, 31 (1999), pp. 495–536.

[99] Y. ZHOU, *Rayleigh–Taylor and Richtmyer–Meshkov instability induced flow , turbulence , and mixing . II*, Physics Reports, 723-725 (2017), pp. 1–160.

[100] Y. ZHOU, *Rayleigh–Taylor and Richtmyer–Meshkov instability induced flow, turbulence, and mixing. I*, Physics Reports, 720-722 (2017), pp. 1–136.

[101] A. B. ZYLSTRA, C. K. LI, H. G. RINDERKNECHT, F. H. SÉGUIN, R. D. PETRASSO, C. STOECKL, D. D. MEYERHOFER, P. NILSON, T. C. SANGSTER, S. LE PAPE, A. MACK-INNON, AND P. PATEL, *Using high-intensity laser-generated energetic protons to radiograph directly driven implosions*, Review of Scientific Instruments, 83 (2012).